MINISTRY OF EDUCATION AND RESEARCH

THE ANNALS OF "DUNAREA DE JOS" UNIVERSITY OF GALATI

Fascicle IX
METALLURGY AND MATERIALS SCIENCE

YEAR XLIV (XLIX)
June 2026, no. 2

ISSN 2668-4748; e-ISSN 2668-4756

GALATI UNIVERSITY PRESS

2026

EDITORIAL BOARD

THE ANNALS OF "DUNAREA DE JOS" UNIVERSITY OF GALATI
FASCICLE IX. METALLURGY AND MATERIALS SCIENCE
Nº. 2 - 2026, ISSN 2668-4748; e-ISSN 2668-4756
Volume DOI: https://doi.org/10.35219/mms.2026.2

Table of Contents

THE ANNALS OF "DUNAREA DE JOS" UNIVERSITY OF GALATI
FASCICLE IX. METALLURGY AND MATERIALS SCIENCE
Nº. 2 - 2026, ISSN 2668-4748; e-ISSN 2668-4756
Volume DOI: https://doi.org/10.35219/mms.2026.2

THE ANNALS OF "DUNAREA DE JOS" UNIVERSITY OF GALATI
FASCICLE IX. METALLURGY AND MATERIALS SCIENCE
No. 2 - 2026, ISSN 2668-4748; e-ISSN 2668-4756
Article DOI: https://doi.org/10.35219/mms.2026.2.01

DEEP LEARNING-BASED CAMOUFLAGE DETECTION FOR ANTI-PERSONNEL MINE IDENTIFICATION IN NATURAL ENVIRONMENTS

Florin-Bogdan MARIN, Mihaela MARIN
Interdisciplinary Research Centre in the Field of Eco-Nano Technology and Advanced Materials CC-ITI, Faculty of Engineering, "Dunarea de Jos" University of Galati, Romania, 47th Domneasca Street, RO-800008, Galaţi, Romania
e-mail: florin.marin@ugal.ro

ABSTRACT

The detection of anti-personnel mines in natural environments remains a critical humanitarian and technological challenge due to the high visual similarity between explosive devices and their surrounding backgrounds. This study presents a deep learning-based camouflage detection framework for the identification and segmentation of PFM-1 anti-personnel mine surrogates embedded in visually homogeneous outdoor scenes. The proposed approach employs a Deep Camouflage Detection Network (DCDN) designed to extract multi-scale contextual features and enhance boundary sensitivity under low-contrast conditions. A dedicated dataset was constructed using 3D-printed PFM-1 surrogates positioned in vegetated environments under varying illumination conditions, viewing angles, occlusion levels, and object scales. The network architecture integrates a pretrained convolutional backbone, multi-scale feature aggregation modules, and a composite loss function (consisting of Binary Cross-Entropy and Dice loss) to address class imbalance and weak edge contrast.

Experimental evaluation on an independent test set demonstrates robust segmentation performance, achieving a mean Intersection over Union (IoU) of 91.8% and a Dice coefficient of 95.7%. Precision and recall values of 96.3% and 94.9%, respectively, confirm a balanced detection capability with limited false positives. Stratified analysis indicates stable performance under illumination variability and partial occlusion, while ablation studies highlight the importance of multi-scale aggregation and region-aware loss optimization. The results confirm that deep camouflage-aware segmentation architectures provide reliable detection of low-contrast objects in complex natural environments.

KEYWORDS: anti-personnel mine, PFM-1, camouflage detection, semantic segmentation, deep learning

1. Introduction

Anti-personnel mines remain a major humanitarian threat in post-conflict regions due to their long-term persistence and the high risk they pose to civilian populations. The PFM-1 anti-personnel mine, commonly known as the "butterfly mine," is a small plastic explosive device originally developed in the 1970s. Its lightweight construction and distinctive wing-like shape enable wide-area dispersion, while its toy-like appearance increases the risk of accidental interaction, particularly among children [1-3]. Despite international regulations such as the Ottawa Convention aimed at prohibiting anti-personnel mines, recent reports indicate their continued use in contemporary conflicts [1-3].

One promising strategy for reducing casualties involves remote detection using unmanned aerial vehicles (UAVs), which allow for the inspection of hazardous areas without direct human exposure [4-6]. However, effective visual detection of mines such as the PFM-1 remains challenging due to their small size, plastic composition, and colour variants designed to blend with natural environments. The green and brown versions of the device are particularly difficult to distinguish from vegetation

THE ANNALS OF "DUNAREA DE JOS" UNIVERSITY OF GALATI
FASCICLE IX. METALLURGY AND MATERIALS SCIENCE
Nº. 2 - 2026, ISSN 2668-4748; e-ISSN 2668-4756
Article DOI: https://doi.org/10.35219/mms.2026.2.01

and soil backgrounds, resulting in low chromatic contrast and weak boundary definition.

Conventional computer vision methods relying on handcrafted features or simple colour thresholding are insufficient in low-contrast scenarios. Recent advances in deep learning, particularly those involving convolutional neural networks for semantic segmentation, have significantly improved object detection in complex scenes. The U-Net architecture introduced a powerful encoder-decoder framework for pixel-wise segmentation tasks [7], while residual learning approaches such as ResNet improved feature extraction depth and stability [8]. Transformer-based vision models, including the Swin Transformer, further enhanced global context modeling and long-range dependency learning [9]. To improve discrimination in visually ambiguous environments, attention mechanisms such as the Convolutional Block Attention Module (CBAM) were developed to emphasize informative spatial and channel features [10]. Additionally, multi-scale feature aggregation techniques, such as Feature Pyramid Networks (FPN), enable the integration of fine-grained spatial details with high-level semantic information [11]. These strategies are particularly relevant in camouflage detection, where subtle structural inconsistencies rather than strong colour contrasts reveal an object's presence. Deep Camouflage Detection Networks (DCDNs) extend traditional segmentation frameworks to explicitly address low-contrast object detection. The Concealed Object Detection model proposed in recent research demonstrated the effectiveness of multi-scale contextual modeling for camouflaged targets [12]. Specialized datasets such as CAMO [13] and CHAMELEON [14] have further enabled the systematic evaluation of camouflage segmentation performance under controlled conditions. In camouflage scenarios, boundary refinement is critical, as camouflaged objects typically exhibit weak edge gradients. Region-aware and structure-sensitive loss functions, including Dice-based formulations and focal Tversky loss variants, have proven effective in improving segmentation overlap and contour accuracy [15]. These loss functions mitigate class imbalance and encourage precise boundary reconstruction, which is essential when detecting small objects embedded in homogeneous backgrounds.

Motivated by these developments, this study investigates a deep learning-based camouflage detection framework for identifying PFM-1 mine surrogates in natural vegetated environments. A Deep Camouflage Detection Network (DCDN) is employed to perform pixel-wise segmentation of a green 3D-printed PFM-1 model placed in predominantly green outdoor scenes. The primary challenge addressed is the minimal visual separability between the object and the background under varying illumination conditions. The experimental protocol evaluates robustness to changes in lighting, occlusion, and object scale while maintaining methodological reproducibility.

2. Experimental procedure

The experiments used non-hazardous surrogates such as 3D-printed objects with the same dimensions as the PFM 1 anti-personnel mine (Figure 1). A dedicated dataset was constructed by acquiring RGB images of the 3D model positioned in vegetated outdoor scenes, including grass-covered terrain and natural foliage. Data acquisition was performed under diverse illumination conditions (direct sunlight, diffuse lighting, and partial shadow), viewing angles (top-down and oblique perspectives), object-to-camera distances, and occlusion levels caused by surrounding vegetation. Images were divided into training (70%), validation (15%), and test (15%) subsets, ensuring scene-level separation to prevent data leakage. Pixel-level ground truth masks were manually annotated for each image to enable supervised learning and quantitative segmentation evaluation. Prior to training, all images were resized to a fixed spatial resolution compatible with the network input while preserving the aspect ratio through zero-padding where necessary. Input normalization followed ImageNet statistics due to the use of pretrained backbone weights. To improve generalization and mitigate overfitting, online data augmentation was applied during training, including random horizontal and vertical flipping, limited-angle rotation, brightness and contrast adjustment, hue and saturation perturbation, Gaussian blur, additive noise, and random scaling. These transformations simulate environmental variability and enhance robustness to low-contrast camouflage conditions.

The adopted DCDN architecture consists of a pretrained convolutional backbone for hierarchical feature extraction, a multi-scale feature aggregation module that integrates low-level spatial details with high-level semantic representations, and a decoder network producing a dense pixel-wise probability map. The multi-scale design is essential for detecting small, visually ambiguous targets whose features may be suppressed in deeper layers.

Training was conducted using the Adam optimization algorithm with an empirically selected initial learning rate and a scheduled decay.

THE ANNALS OF "DUNAREA DE JOS" UNIVERSITY OF GALATI
FASCICLE IX. METALLURGY AND MATERIALS SCIENCE
No. 2 - 2026, ISSN 2668-4748; e-ISSN 2668-4756
Article DOI: https://doi.org/10.35219/mms.2026.2.01

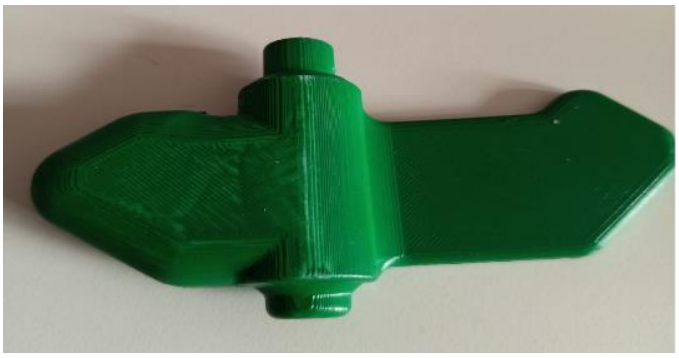

Fig. 1. *3D-printed PFM-1 model*

The training phase was conducted in a supervised manner using the annotated segmentation masks described in the previous section. Model parameters were initialized using pretrained backbone weights, while newly introduced layers were randomly initialized. Optimization was performed using the Adam optimizer with weight decay regularization to improve generalization. The initial learning rate was empirically selected and progressively reduced using a cosine decay schedule. Mini-batch training was adopted, with the batch size determined by the available GPU memory.

To mitigate overfitting, early stopping was applied based on validation IoU performance. The model state corresponding to the highest validation IoU was retained for the final evaluation. In addition, training and validation loss curves were monitored to verify convergence behavior and detect potential instability or gradient saturation.

Given the limited spatial footprint of the 3D model relative to the background, special attention was given to class imbalance during training. The composite loss function (BCE + Dice) ensured stable optimization by balancing pixel-wise classification accuracy with region-level overlap consistency. Hard samples, particularly those involving heavy occlusion or extreme illumination conditions, were implicitly emphasized through the Dice component of the loss.

During testing, the trained model was evaluated on the held-out test dataset without any data augmentation. Each input image was passed through the network to generate a dense probability map. A fixed decision threshold, determined from validation experiments, was applied to produce binary segmentation masks. No test-time augmentation was employed in order to preserve the strict comparability of the results. Quantitative evaluation was performed using the Intersection over Union (IoU), the Dice coefficient (F1 score), pixel-wise precision and recall, and the Mean Absolute Error (MAE). In addition to the overall performance, a stratified analysis was conducted to assess robustness under varying illumination conditions, object scales, and occlusion levels. To further validate the generalization capability, a qualitative visual inspection of predicted masks was performed, focusing on boundary accuracy and false positive regions in highly homogeneous background areas. The inference time per image was measured to evaluate computational efficiency and assess the feasibility of near real-time deployment.

All experiments were conducted using a fixed hardware configuration and a controlled software environment to ensure reproducibility. Training duration, the total number of epochs, the convergence epoch, and the average inference latency were recorded and reported as part of the experimental results.

3. Results and Discussion

The proposed DCDN-based framework was evaluated on an independent test set to assess segmentation accuracy, robustness, and computational performance in low-contrast conditions. Quantitative results indicate that the model achieves high detection reliability despite strong foreground–background similarity. On the test dataset, the model achieved a mean Intersection over Union (IoU) of 91.8% and a Dice coefficient (F1 score) of 95.7%, indicating a strong overlap between predicted masks and ground truth annotations. Pixel-wise precision reached 96.3%, while recall was 94.9%, demonstrating a balanced performance with limited false positives and high object recovery. The Mean Absolute Error (MAE) between predicted probability maps and ground truth masks was 0.021, reflecting stable pixel-level confidence estimation.

The overall quantitative performance is summarized in Table 1. The reported metrics confirm that the proposed DCDN architecture achieves consistently high segmentation accuracy across the independent test dataset. The strong Dice coefficient and balanced precision–recall values indicate reliable object localization with limited false positive

THE ANNALS OF "DUNAREA DE JOS" UNIVERSITY OF GALATI
FASCICLE IX. METALLURGY AND MATERIALS SCIENCE
N°. 2 - 2026, ISSN 2668-4748; e-ISSN 2668-4756
Article DOI: https://doi.org/10.35219/mms.2026.2.01

activations in visually homogeneous background regions.

Table 1. *Overall segmentation performance on the independent test dataset*

Metric	Value
Mean IoU (%)	91.8
Dice coefficient (%)	95.7
Precision (%)	96.3
Recall (%)	94.9
MAE	0.021

A stratified robustness analysis was conducted to evaluate segmentation stability under varying environmental conditions, including changes in illumination and partial vegetation occlusion. The quantitative results for each scenario are presented in Table 2. The model maintains IoU values above 90% across all tested conditions, demonstrating resilience to moderate lighting variability and the structural interference caused by surrounding vegetation.

Table 2. *Segmentation performance under varying environmental conditions*

Condition	IoU (%)
Diffuse lighting	93.1
Direct sunlight	91.2
Partial shadow	90.4
Partial occlusion	90.6

The experimental results confirm that the Deep Camouflage Detection Network (DCDN) provides robust performance in detecting a low-contrast 3D model embedded in a visually homogeneous green environment. Achieving a mean IoU of 91.8% demonstrates that deep multi-scale feature aggregation effectively compensates for reduced chromatic separability between the foreground and the background. One key observation is the importance of combining region-based and pixel-wise optimization objectives. The composite loss function (BCE + Dice) significantly improved segmentation overlap compared to using BCE alone. This suggests that region-aware supervision is essential when the target object occupies a small fraction of the image and exhibits weak edge contrast. The robustness analysis further indicates that illumination variability has a measurable but controlled impact on performance. While extreme lighting conditions slightly reduced the IoU, the degradation remained limited, confirming that data augmentation played a critical role in improving generalization. Similarly, performance under partial occlusion remained above 90% IoU, highlighting the effectiveness of multi-scale contextual fusion in reconstructing incomplete object representations.

However, several limitations should be acknowledged. First, performance decreased for very small object scales, suggesting a sensitivity to extreme spatial reduction. Second, false positives were occasionally observed in background regions with repetitive texture patterns similar to the object surface. This indicates that texture-based ambiguity remains a challenge in camouflage detection tasks. Future work may address this limitation by incorporating attention mechanisms or transformer-based global context modeling.

From a computational standpoint, the achieved inference speed supports near real-time deployment at moderate resolution. Nevertheless, scaling to higher resolutions or resource-constrained platforms may require architectural optimization or lightweight backbone variants.

Under partial occlusion by vegetation, the model maintained an IoU of 90.6%, suggesting that multi-scale feature aggregation effectively preserved the contextual information necessary for segmentation. Qualitative inspection confirmed accurate contour localization in most test samples. Minor boundary smoothing effects were observed in highly textured grass regions, and isolated false positives appeared in background areas exhibiting similar structural patterns. However, such instances were limited and did not significantly impact the overall metrics.

From a computational perspective, the average inference time per image was 28 ms at a resolution of 352×352 pixels on an NVIDIA RTX-class GPU, corresponding to approximately 35 frames per second, which supports near real-time applicability. The contribution of individual architectural components was further analysed through an ablation study. The quantitative results are summarized in Table 3. Each configuration was retrained under identical conditions to isolate the impact of the removed component on segmentation performance.

Table 3. *Ablation study evaluating the impact of architectural components on segmentation performance*

Model configuration	Mean IoU (%)
Full model (BCE + Dice + multi-scale + augmentation)	91.8
Without Dice loss	88.9
Without multi-scale aggregation	86.7
Without data augmentation	87.5

The results indicate that multi-scale feature aggregation has the largest impact on performance, as

its removal reduced the IoU by more than 5%. Excluding the Dice component from the loss function resulted in a 2.9% IoU decrease, confirming the importance of region-aware supervision in low-contrast segmentation tasks. The absence of data augmentation led to a reduced generalization capability, particularly under illumination variability, highlighting the importance of environmental diversity during training.

Overall, the experimental results demonstrate that the proposed DCDN-based approach achieves a segmentation performance consistently above 90% IoU under most evaluation conditions. These findings confirm the suitability of deep camouflage-aware architectures for detecting low-contrast 3D models in visually homogeneous environments while maintaining a computational efficiency compatible with real-time processing constraints. A qualitative example of the segmentation output is illustrated in Figure 2.

Fig. 2. *Camouflaged 3D-printed PFM-1 in vegetated scene and corresponding DCDN segmentation result*

4. Conclusions

This paper presented a systematic experimental evaluation of a Deep Camouflage Detection Network for detecting a green 3D model in a visually homogeneous green landscape. Robustness analysis confirmed stable performance across illumination changes, moderate occlusion, and varying object scales, while maintaining a computational efficiency suitable for near real-time processing. Overall, the findings support the applicability of deep camouflage-aware architectures in advanced computer vision research, particularly for tasks involving visually ambiguous or low-contrast targets. Future research directions include the integration of attention-based modules, the exploration of transformer-driven global feature modeling, and the evaluation on larger, more diverse datasets to further improve generalization capability.

References

[1]. ***, *Ukraine: Banned Landmines Harm Civilians*, Human Rights Watch, Jan. 31, 2023.
[2]. ***, *Anti-Personnel Landmines Convention (Ottawa Convention)*, United Nations Office for Disarmament Affairs (UNODA), accessed Feb. 23, 2026.
[3]. *,** *International Campaign to Ban Landmines (ICBL-CMC)*, *Landmine Monitor 2023*, Geneva, Switzerland, Nov. 2023.
[4]. Baur J., *et al.*, *Applying deep learning to automate UAV-based detection of scatterable landmines*, Remote Sensing, 12(5), 859, 2020.
[5]. García-Fernández M., *et al.*, *Autonomous airborne 3D SAR imaging system for subsurface sensing: UWB-GPR on board a UAV for landmine and IED detection*, Remote Sensing, 11(20), 2357, 2019.
[6]. Marin F.-B., Marin M., *Drone detection using image processing based on deep learning*, Annals of "Dunarea de Jos" University of Galati, Fascicle IX, 44(4), p. 36-39, 2021.
[7]. Ronneberger O., *et al.*, *U-Net: Convolutional networks for biomedical image segmentation*, Proc. MICCAI, p. 234-241, 2015.
[8]. He K., *et al.*, *Deep residual learning for image recognition*, Proc. IEEE CVPR, p. 770-778, 2016.
[9]. Liu Z., *et al.*, *Swin Transformer: Hierarchical vision transformer using shifted windows*, Proc. IEEE ICCV, p. 10012–10022, 2021.
[10]. Woo S., *et al.*, *CBAM: Convolutional block attention module*, Proc. ECCV, p. 3-19, 2018.
[11]. Lin T.-Y., *et al.*, *Feature pyramid networks for object detection*, Proc. IEEE CVPR, p. 2117-2125, 2017.
[12]. Fan D.-P., *et al.*, *Concealed object detection*, IEEE Transactions on Pattern Analysis and Machine Intelligence, 44(10), p. 6024-6042, 2022.
[13]. Le T.-N., *et al.*, *A. Sugimoto, Anabranch network for camouflaged object segmentation*, Computer Vision and Image Understanding, 184, p. 45-56, 2019.
[14]. Skurowski P., Kasprowski P., *Evaluation of saliency maps in a hard case-images of camouflaged animals*, Proc. IPAS, p. 244-249, 2018.
[15]. Abraham N., Khan N. M., *A novel focal Tversky loss function with improved attention U-Net for lesion segmentation*, Proc. IEEE ISBI, p. 683-687, 2019.

THE ANNALS OF "DUNAREA DE JOS" UNIVERSITY OF GALATI
FASCICLE IX. METALLURGY AND MATERIALS SCIENCE
N°. 2 - 2026, ISSN 2668-4748; e-ISSN 2668-4756
Article DOI: https://doi.org/10.35219/mms.2026.2.02

FRACTURE BEHAVIOR OF DISSIMILAR RESISTANCE SPOT WELDED OVERLAP JOINT

Abdelkader BENYOUCEF[1], Mustapha BENACHOUR[1*], Nadjia BENACHOUR[1,2], Fatima Zohra SERIARI[3]

[1]Mechanical Systems & Materials Engineering Laboratory, Mechanical Engineering Department, Faculty of Technology, University of Tlemcen, Algeria
[2]Mechanical Systems & Materials Engineering Laboratory, Physics Department, University of Tlemcen, Algeria
[3]Mechanical Systems & Materials Engineering Laboratory, Faculty of Technology, University of Tlemcen, Algeria
e-mail: bmf_12002@yahoo.fr

ABSTRACT

The resistance spot welding process is also used for the welding of dissimilar materials. A dissimilar join is formed by two sheets: a 1.0 mm thick sheet of low-alloy carbon steel and a 1.5 mm thick sheet of aluminium alloy 6061 T6. In this study, the effects of welding current and nugget diameter are investigated. Welding times and welding force are kept constant. Tensile shear tests were applied in order to determine the strength parameters of the dissimilar joint. The experimental results show that an increase in the welding current increases the tensile shear stress and the weld nugget diameter. This study used a fracture mechanics-based approach, to investigate the influence of resistance spot welding parameters on the critical stress intensity factor. The results show that the critical stress intensity factor is maximal for a welding current equal to 16 kA. Also, the maximum tensile shear strength is achieved at an 8 mm nugget diameter, which is influenced by an increase in the welding current.

KEYWORDS: resistance spot welding, dissimilar lap joint, welding current, critical stress intensity factor, aluminium-alloy/low carbon steel

1. Introduction

Resistance spot welding (RSW) represents the major welding process used in various manufacturing industries, especially in automobile truck cabin manufacturing, rail vehicles, motorcycles, and home appliances, such as refrigerators. For example, there are 3000 to 12000 spot welds in an automobile [1]. The majority of research investigations in spot welding have been carried out on the joining of homogeneous materials [2, 3]. Currently, research in different industries is directed towards the reduction of CO_2 emissions. Hence, the combination of heterogeneous materials is necessary in order to reduce the weight of structures and, consequently, CO_2 emissions [4]. Engineers are increasingly faced with joining different material types where they are looking for joints ensuring good mechanical strength and corrosion resistance, and ensuring a good sealing function [5]. Also, for a dissimilar Al/steel joint welded using direct RSW, as shown in Figure 1, different metallurgical phenomena occur [6]. The mechanical properties of Al/steel RSW depend on several factors controlling the quality of the joints. The factors controlling the mechanical properties can be summarized as follows: bonding zone length, the thickness of the IMC layer, electrode indentation in the Al sheet, and defects at the joint interface [7-9].

RSW of dissimilar materials, specifically high-strength galvanized steel and Aluminium alloy, was investigated by Zhang *et al.* [10]. Qui *et al.* [11] have studied the interfacial characterization of the joint between mild steel and an aluminium alloy welded by resistance spot welding with an applied cover plate technique. It is noticed from this study that there is an improvement in mechanical properties. All the cited researches are oriented toward studying mechanical properties under different welding parameters.

The study conducted by Zhang and Sun [12] investigates the mechanical behavior of RSW joints between two dissimilar material types, namely 301L austenitic stainless steel and 6063-T6 aluminium

THE ANNALS OF "DUNAREA DE JOS" UNIVERSITY OF GALATI
FASCICLE IX. METALLURGY AND MATERIALS SCIENCE
Nº. 2 - 2026, ISSN 2668-4748; e-ISSN 2668-4756
Article DOI: https://doi.org/10.35219/mms.2026.2.02

alloy, as well as the effects of welding parameters. The results show an increase in nugget diameter and tensile shear load with the increase in welding current and welding time.

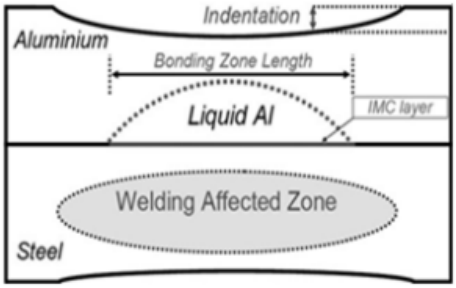

Fig. 1. *Schematic of the macrostructure of dissimilar resistance spot welds between aluminium and steel, along with details of the interfacial reaction zone* [6]

In the study conducted by Xu *et al.* [13], the resistance spot welding process was performed to join aluminium alloy and low-alloy carbon steel plates. The nugget diameters, indentation rates, microstructure, and tensile-shear strength of the RSW joints were investigated. The nugget diameters and the indentation rates of the RSW joints increased when increasing either the welding current or the welding time, and decreased when increasing the electrode pressure.

The research conducted by Ramdani *et al.* [14] reveals that welding parameters and nugget diameter are important factors that determine the load-bearing capacity of the overloaded RSW joint and its resistance to fracture.

Recently, several researches have been oriented toward fracture or fatigue behavior that depends on the stress intensity factor. Pook's resistance spot welding stress analysis refers to early fracture mechanics work by L.P. Pook, which applied stress intensity factors to predict the fatigue life of spot-welded joints [15]. His approach aimed to improve the scatter of fatigue data by analysing fatigue crack growth in terms of stress intensity factors rather than just load, though his method was limited to small-scale yielding and low applied loads [16]. More recent research continues to build on this foundation, using more advanced finite element analysis (FEA) to determine stress intensities and fatigue life [17], with some studies verifying results against Pook's work or developing alternative parameters, such as the fatigue evaluation parameter. Based on a stress analysis around the spot weld in lap joints and coach peel joints of Pook's work, Zhang [18] has determined the stress intensity at the spot weld for overlap joints and coach peel joints, with the assumption that the nugget has a circular shape.

Radja and Zhang [19] have proposed simplified formulae for stress intensity factors to evaluate the fracture toughness in spot welds. Also, Zhang [20] has proposed analytically an approximate stress intensity factor to use in optimizing the fatigue-resistant spot weld for different specimen configurations. Benchadli *et al.* [21] have studied the effect of resistance spot welding parameters on the stress intensity factor for a homogeneous joint with 316L stainless steel using Zhang's approach, where the welding current presents the dominant parameter. Recently, Fakhri *et al.* [23] have conducted an experimental and numerical investigation of the mechanical properties and stress intensity factor of a dissimilar spot weld joint (Al-Cu).

Based on the literature, the evaluation of the critical stress intensity factor is oriented principally toward homogeneous joints, especially for steel materials, and there is limited research for aluminium alloys. The association of two different materials with different densities contributes to the formation of an intermetallic compound after welding between the Al-alloy and steel. In this regard, great attention must be paid to the fracture behavior at the resistance weld point especially the estimation of the critical stress intensity factor. This research aims to evaluate the critical stress intensity factors for a dissimilar lap joint with two different materials (aluminium alloy 6061 T6 and low-alloy carbon steel) based on Zhang's approach [18, 20] under the influence of welding current and nugget diameter for a fixed welding time and electrode force.

2. Experimental data base

The experimental database was derived from the published work initiated by Xu *et al.* [13]. The experimental results are based on tensile shear tests of dissimilar spot-welded joints composed of low-alloy carbon steel and 6061 T6 Al-alloy. The welding current varies from 11 to 18 kA, the welding time and electrode force are fixed to 250 ms and 3 kN, respectively. The geometry of the resistance spot welding joint is given in (Figure 2). The experimental results for the nugget diameter and maximal shear force as a function of the welding current are given in Table 1.

THE ANNALS OF "DUNAREA DE JOS" UNIVERSITY OF GALATI
FASCICLE IX. METALLURGY AND MATERIALS SCIENCE
N°. 2 - 2026, ISSN 2668-4748; e-ISSN 2668-4756
Article DOI: https://doi.org/10.35219/mms.2026.2.02

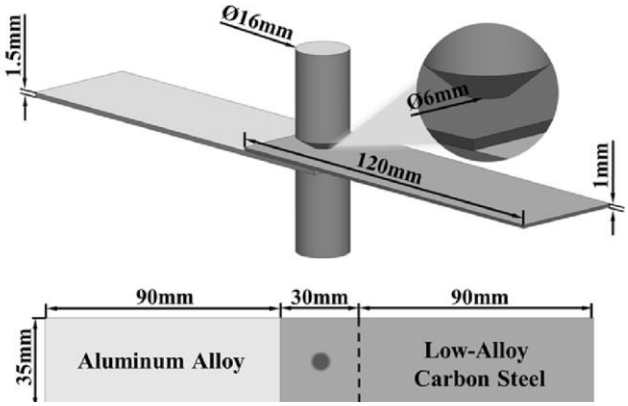

Fig. 2. *Dimensions of a dissimilar RSW sample for tensile shear tests* [13]

Table 1. *Nugget diameter and maximum tensile shear force as a function of the welding current* [13]

I (kA)	D (mm)	F (N)
11	4.13	995.73
12	5.22	1113.25
13	5.34	1294.87
14	6.99	1588.68
15	7.68	1807.69
16	7.99	2026.71
17	8.17	1674.15
18	8.18	1485.00

3. Results & discussion

3.1. Critical stress intensity factor model

In this study, a tensile shear overlap joint is used (Figure 3). The significant stress-inducing variables at the front-facing vertex parallel to the loaded direction (at point A in Figure 3), KI and KII, occur concurrently and can be determined by Zhang's method [19, 21]. Also, other analytical and numerical solutions for the stress intensity factor have been determined and are suitable for a novel application to dissimilar resistance spot welding [22].

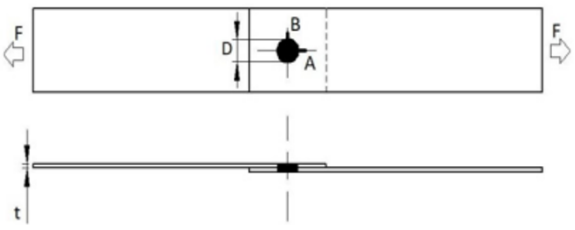

Fig. 3. *Tensile shear of a dissimilar overlap joint*

$$K_I = \frac{F.\sqrt{3}}{2\pi.D\sqrt{t}} \quad (1)$$

$$K_{II} = \frac{F}{\pi.D.\sqrt{t}} \quad (2)$$

The maximum KIII at the nugget edge side facing the vertex at point B (Fig. 3) for tensile-shear spot welds is given by equation 3:

$$K_{III} = \frac{F\sqrt{2}}{\pi.D.\sqrt{t}} \quad (3)$$

The equivalent stress intensity factor is given by equation 4:

$$K_{eq} = \frac{F.\sqrt{19}}{2.\pi.D.\sqrt{t}} \quad (4)$$

where D is the diameter of the nugget (mm), "t" is the thickness of the plate (mm), and F is the maximum applied force in tensile shear resistance spot welding.

3.2. Effect of welding current on critical stress intensity factor

As exhibited in Figure 4, an increase in the welding current from 11 kA to 15 kA results in a low variation in the equivalent stress intensity factor K_{eq}, from 149.7 to 146.3 N/mm$^{3/2}$. The maximum stress intensity factor, K_{eq}, is achieved at a welding current equal to 16 kA with a value of 156.9 N/mm$^{3/2}$. From I = 17 to 18 kA, it is noticed that there is a reduction in the equivalent stress intensity factor, where the minimum value is 112.5 N/mm$^{3/2}$ for I = 18 kA; this is attributed to the large nugget diameter. The obtained results show that I = 16 kA is the optimal welding current. This result is confirmed by the published work of Benchadli *et al.* for a 316L

THE ANNALS OF "DUNAREA DE JOS" UNIVERSITY OF GALATI
FASCICLE IX. METALLURGY AND MATERIALS SCIENCE
No. 2 - 2026, ISSN 2668-4748; e-ISSN 2668-4756
Article DOI: https://doi.org/10.35219/mms.2026.2.02

homogeneous joint [21]. The critical stress intensity factors of all modes (KI, KII and KIII) are controlled by the ratio of tensile shear force to nugget diameter: F/D).

Also, the variation of the stress intensity factor in mode II follows the same tendency compared to the equivalent stress intensity factor. The maximum stress intensity factor is identified at a welding current of I = 16 kA. The critical stress intensity factor in mode II exhibits higher values for all welding currents relative to mode I and mode III. The critical stress intensity factor for mode I shows low values under the variation of welding current compared to modes II and III. The maximum stress intensity factor is about 62.33 N/mm$^{3/2}$ for a welding current equal to 16 kA.

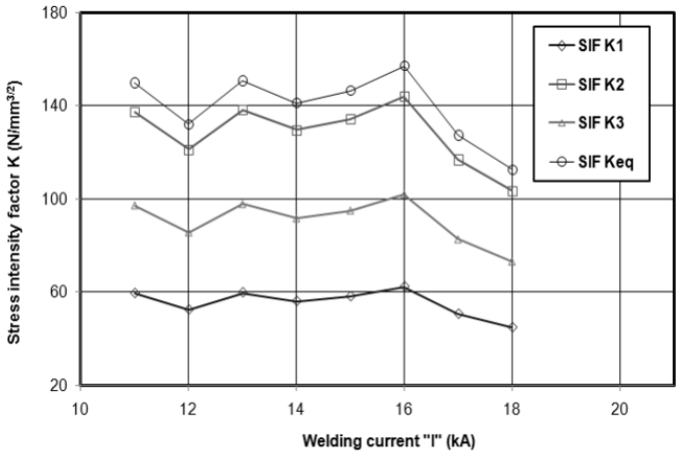

Fig. 4. *Effect of welding current on the critical stress intensity factor for a dissimilar RSW joint 6061-T6/low-alloy carbon steel*

The effect of the nugget diameter as a function of weld current is given in (Figure 5). A low variation of the critical stress intensity factor during the increase in welding current from 11 to 17 kA can be observed. Also, it is noticed that the maximum value for the nugget diameter is equal to 8 mm. Before this value of nugget diameter, a decrease in the critical stress intensity factor is shown for all modes of fracture mechanics at the resistance spot welding points. The intensity coefficient remains the same for both K_{eq} and KII as the weld zone diameter changes. This result shows that the fracture of the resistance spot welding point is governed by mode II rather than mode I.

The maximal tensile shear strength as a function of the nugget diameter is given in (Figure 6). An exponential evolution is shown for the increase in nugget diameter between 4.16 mm and 8 mm. The maximum tensile shear strength equal to "2020 N" is obtained at a nugget diameter equal to 8 mm, followed by a decrease to 1485 N at a nugget diameter equal to 8.18 mm.

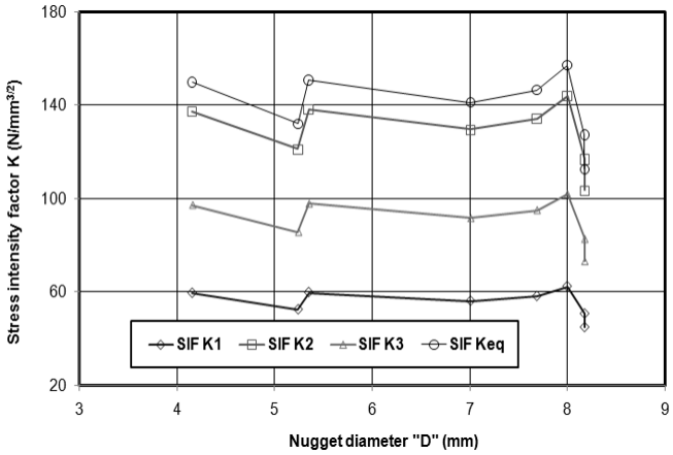

Fig. 5. *Effect of the nugget diameter on the stress intensity factor of a dissimilar lap joint 6061-T6 / low-alloy carbon steel*

THE ANNALS OF "DUNAREA DE JOS" UNIVERSITY OF GALATI
FASCICLE IX. METALLURGY AND MATERIALS SCIENCE
No. 2 - 2026, ISSN 2668-4748; e-ISSN 2668-4756
Article DOI: https://doi.org/10.35219/mms.2026.2.02

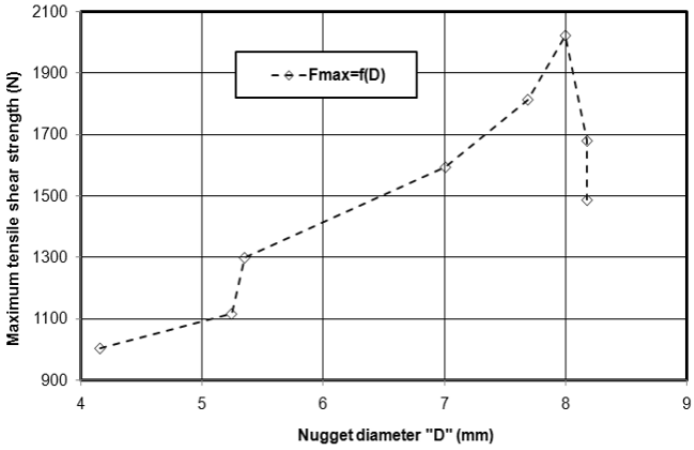

Fig. 6. *Evolution of the maximum tensile shear strength as a function of the nugget diameter*

4. Conclusions

The quality of spot weld joints is strongly related to the welding current. The investigation into resistance spot welding joints reveals a complex relationship between the welding current, mechanical properties, and the formation of the nugget, especially in dissimilar resistance spot welding joints. In conclusion, the observed trends highlight the critical importance of selecting an optimal welding current to achieve the desired mechanical properties and fracture parameters in resistance spot welding joints. Results reveal a direct relationship between the welding current and the nugget diameter. It is crucial to comprehend the relationship between the welding current and fracture toughness (critical stress intensity factor). The second mode of fracture, KII, dominates the fracture process in resistance spot welding compared to fracture modes I and III. The maximum equivalent critical stress intensity factor (K_{eq}) is obtained at a welding current equal to 16 kA. Also, the relationship between the equivalent critical stress intensity factor and the nugget diameter shows that the maximum Keq is achieved at the nugget diameter corresponding to I = 16 kA. The dissimilar joint (aluminium alloy/low carbon steel) exhibits low values of the critical stress intensity factor compared to stainless steel or low carbon steel homogeneous joints.

Nomenclature

I - Welding current (kA)
D - Nugget diameter (mm)
F - Maximum tensile shear (N)
T - Thickness of the RSW joint (mm)
KI - Stress intensity factor in mode I ($N/mm^{3/2}$)
KII - Stress intensity factor in mode II ($N/mm^{3/2}$)
KIII - Stress intensity factor in mode III ($N/mm^{3/2}$)
Keq - Equivalent stress intensity factor ($N/mm^{3/2}$)

References

[1]. Shawon M. R. A., *et al.*, *Effect of welding current on the structure and properties of resistance spot welded dissimilar (austenitic stainless steel and low carbon steel) metal joints*, Journal of the Institution of Engineers (India), Series D, 96(1), p. 29-36, 2015.
[2]. Alzahougi A., *et al.*, *RSW Junctions of Advanced Automotive Sheet Steel by Using Different Electrode Pressures*, Eng. Technol. Appl. Sci. Res., vol. 8, no. 5, p. 3492-3495, Oct. 2018.
[3]. Guezzen S., *et al.*, *Spot welding parameters influence on the assembled structures behavior*, Annals of "Dunarea de Jos" University of Galati. Fascicle XII, Welding Equipment and Technology, vol. 4, 2025.
[4]. Mezrag B., *et al.*, *Control of mass and heat transfer for steel/aluminium joining using Cold Metal Transfer process*, Science and Technology of Welding and Joining, 20 (3), p. 189-198, 2015.
[5]. Pouranvari M., Marashi S. P. H., *Similar and dissimilar RSW of low carbon and austenitic stainless steels: effect of weld microstructure and hardness profile on failure mode*, Materials Science and Technology, 25(12), p. 1411-1416, 2009.
[6]. Pouranvari M., *Critical assessment 27: dissimilar resistance spot welding of aluminium/steel: challenges and opportunities*, Materials Science and Technology, 33(15), p. 1705-1712, 2017.
[7]. Wan Z., *et al.*, *Characterization of intermetallic compound at the interfaces of Al/steel resistance spot welds*, J. Mater. Process. Technol., 242, p. 12-23, 2017.
[8]. Ibrahim I., *et al.*, *Fatigue behaviour of Al/steel dissimilar resistance spot welds fabricated using Al-Mg interlayer*, Sci. Technol. Weld. Join., 21, p. 223-233, 2017.
[9]. Qiu R. F., *et al.*, *Effect of interfacial reaction layer continuity on the tensile strength of resistance spot welded joints between Al alloy and steels*, Mater Des., 30, p. 3686-3689, 2009.
[10]. Zhang W. H., *et al.*, *Effects of resistance spot welding parameters on microstructures and mechanical properties of dissimilar material joints of galvanised high strength steel and aluminium alloy*, Sci. Technol. Weld. Join., 16, p. 153-161, 2011.
[11]. Qiu R., *et al.*, *Interfacial characterization of joint between mild steel and aluminum alloy welded by resistance spot welding*, Mater. Charact., 61, p. 684-688, 2010.
[12]. Zhang Y., Sun D., *Microstructures and mechanical properties of steel/aluminum alloy joints welded by RSW*, Journal of Materials Engineering and Performance, 26(6), p. 1-14, 2017.

[13]. Xu Y., *et al.*, *Dissimilar joining of aluminum alloy and low-alloy carbon steel by resistance spot welding*, Journal of Materials Research and Technology, 33, p. 919-928, 2024.
[14]. Ramdani M., *et al.*, *The Effects of Resistance Spot Welding Parameters on the Mechanical Behavior of Stainless Steel*, Eng. Technol. Appl. Sci. Res., vol., 13(2), p. 10501-04, 2023.
[15]. Pook L. P., *Fracture mechanics analysis of the fatigue behavior of spot weld*, International Journal of Fracture, 11, p. 173-176, 1975.
[16]. Pook L. P., *Practical implications of the fatigue crack growth threshold*, Metal Science, p. 382-389, 1977.
[17]. Yuuki R., Ohera T., *Development of the method to evaluate the fatigue life of spot welded structures by fracture mechanics*, IIW Doc. III-928-89.
[18]. Zhang S., *Stress Intensities at Spot Welds*, International Journal of Fracture, vol. 88(2), p. 167-185, 1997.
[19]. Radaj D., Zhang S., *Simplified formulae for stress intensity factors of spot welds*, Engineering Fracture Mechanics, vol. 40, no. 1, p. 233-236, Jan. 1991.
[20]. Zhang S., *Approximate stress intensity factors and notch stresses for common spot-welded specimens*, Welding Journal, vol. 78(5), p. 173-179, 1999.
[21]. Benchadli I., *et al.*, *Evaluation of Critical Stress Intensity Factor for Different RSW Joints*, Eng. Technol. Appl. Sci. Res., vol. 14, no. 5, p. 16766-16771, 2024.
[22]. Zhang S., *Fracture mechanics solutions to spot welds*, International Journal of Fracture, 112, p. 247-274, 2001.
[23]. Fakhri M. S., *et al.*, *Experimental and numerical investigation of mechanical properties and stress intensity factor of dissimilar spot weld joint*, Journal of Materials Engineering and Performance, 34, p. 13355-13369, 2025.

THE ANNALS OF "DUNAREA DE JOS" UNIVERSITY OF GALATI
FASCICLE IX. METALLURGY AND MATERIALS SCIENCE
N°. 2 - 2026, ISSN 2668-4748; e-ISSN 2668-4756
Article DOI: https://doi.org/10.35219/mms.2026.2.03

SIMULATION OF THE MECHANICAL STRESS BEHAVIOR IN THE CASE OF THE DAMASCUS STEEL AFTER HEAT TREATMENTS FOR IMPROVEMENT

Carmen-Penelopi PAPADATU
"Dunarea de Jos" University of Galati, Romania, Faculty of Engineering, Interdisciplinary Research Centre in the Field of Eco-Nano Technology and Advanced Materials (CC-ITI), 111 Domneasca Street, Galati, Romania
e-mail: cpapadatu@ugal.ro

ABSTRACT

The paper aims to study the behavior of Damascus steel at a maximum admissible load with a force of 250 N. Previous studies considered lower loading force values that did not produce cracks in the material. The processing of the samples and laboratory tests were carried out on specimens of Damascus steel obtained in the laboratory. The applied treatments were hardening and tempering to improve the material's properties. The processing of the results and the simulations were carried out using Autodesk Inventor Professional 2023.

KEYWORDS: Damascus steel, improvement treatment, structural aspects, mechanical properties, simulation

1. Introduction

High-carbon steels are known for their excellent mechanical properties, especially hardness and strength. These properties are achieved through the process of quenching and tempering, which involves heating the steel to a high temperature, holding it there, and then rapidly cooling it in a liquid such as oil or water. This process causes the crystal structure of the steel to change, increasing the amount of Martensite, which leads to higher hardness and higher tensile strength properties.

Damascus steel involves the hot forging of two high-carbon steels and subsequent heat treatment to improve their hardness.

According to the specialized literature [1], special studies have been conducted on Persian Damascus steel blades from the 18th century, original blades from Iran. In the work highlighted above, the morphology of the carbide bands was analysed in relation to the shape of the edge profiles. For example, the dagger blade (Khanjar) exhibited a transverse section with cross-shaped traces. Sukhanov *et al.* observed that in the case of the sword blade from Iran (Shamshir), the cross-section has a reticular profile.

Sukhanov [1, 2] also demonstrated that the morphology of the carbide bands in the structure of Damascus steel depends directly on the chemical composition – specifically the steels used to form the Damascus steel - and the distribution of inclusions in the material. These inclusions can be oxides and sulphides in the carbide layers.

The morphology of the carbide strips greatly modifies both the physical and mechanical properties, as well as the wave-shaped macrostructure of Damascus blades. It can be stated that the microstructure of the carbide strips determines the quality of Damascus steel and its resistance to loading stresses. The quality of oriental Damascus blade steels is directly related to the distribution of the carbide strips in the pearlitic matrix. In this regard, several important studies have been carried out on the appearance and morphology of the carbide strips in Damascus steel in the history of authentic Damascus steels [3-11]. According to research [12-14], the structure of Damascus steel has a unique characteristic specific to these samples compared to high-hardness tool steels.

Figures 1 and 2 present the essence of the research by Sukhanov's team on the morphology of carbide bands in the structure of original Damascus steel from Iran from the 18th century.

According to [3, 4], very distinct bands of Fe_3C particles can be observed in the matrix. The pearlite matrix has a band spacing of 50 μm. The matrix was formed by Pearlite (P), except for a thin DET region near the fat end. It is worth noting that the first mentions of Damascus steel date back to around 300 BC (originally called "wootz") [5-8, 12-15].

THE ANNALS OF "DUNAREA DE JOS" UNIVERSITY OF GALATI
FASCICLE IX. METALLURGY AND MATERIALS SCIENCE
No. 2 - 2026, ISSN 2668-4748; e-ISSN 2668-4756
Article DOI: https://doi.org/10.35219/mms.2026.2.03

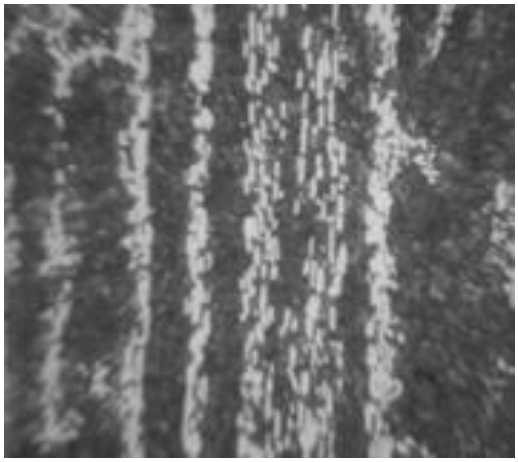

Fig. 1. *Carbide band in the longitudinal direction (cutting edge of the original blade): a Shamshir saber blade, according to* [1, 2] *(100 μm)*

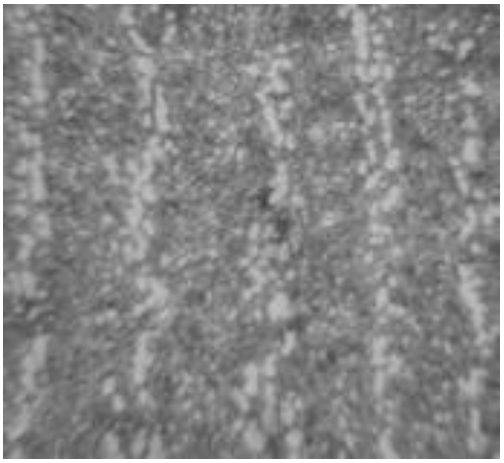

Fig. 2. *Carbide band in the case of the original Khanjar dagger blade, according to* [1, 3, 4]

Studies of this type of steel can help develop new technologies for producing high-strength knives and more.

2. Materials and method

To fabricate Damascus steel in the laboratory, two high-carbon steels were considered, namely: AISI 1095 and 15N20. Hypereutectoid steels were used. For example, AISI 1095 steel contains 0.90-1.03% C and 15N20 steel contains 0.75% C and 2% Ni.

In the hypereutectoid range, above 0.77% C, secondary cementite (Fe3CII) appears, which leads to increased hardness but decreased plasticity and toughness. The tensile strength shows a maximum around 0.9-1% carbon because at higher carbon contents, secondary cementite separates in the form of a continuous network at the pearlite grain boundaries (where Ledeburite appears), producing an embrittlement effect.

In the experimental process of preparing the specimens (Damascus steel), plates in the form of rectangular shapes (see Fig. 3) with dimensions of 2 x 40 x 100 mm were used. These were alternated to obtain packages of 30 layers each, which, by free forging/hot hammering, resulted in the knife blade shown in Figure 4 [14, 15].

Fig. 3. *Specimens in the form of rectangular plates before the hot forging process*

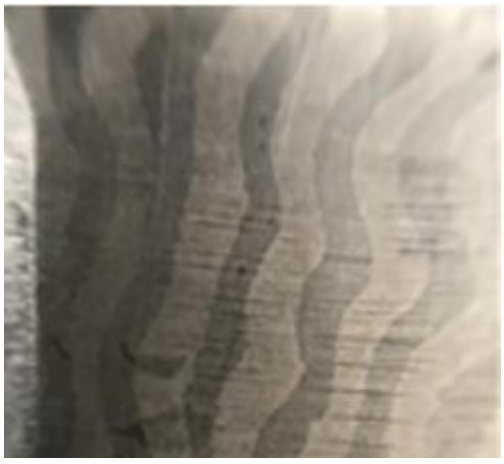

Fig. 4. *Sample obtained in the laboratory* [14, 15]

The samples obtained in the laboratory present waves with different shades of grey that can be compared to the microstructure of the ancient Iranian swords in Figures 1 and 2. A belt sander was used to remove oxide layers and impurities.

The semi-finished products were cleaned with a degreasing agent.

The applied treatments were hardening at 900 °C (1 h) followed by cooling in water and tempering

THE ANNALS OF "DUNAREA DE JOS" UNIVERSITY OF GALATI
FASCICLE IX. METALLURGY AND MATERIALS SCIENCE
No. 2 - 2026, ISSN 2668-4748; e-ISSN 2668-4756
Article DOI: https://doi.org/10.35219/mms.2026.2.03

at 250 °C to improve the mechanical properties, especially the hardness of the steel. After performing the heat treatment, the Brinell hardness of the Damascus steel obtained in the laboratory increased from 197 daN/mm^2 to 698 daN/mm^2 [12-14].

The processing of the results and the simulations were carried out using Autodesk Inventor Professional 2023.

3. Aspects of the Stress Analysis Report

The objective of this study was to analyse the behavior of the knife blade under loading conditions for F = 250 N. The study includes the evaluation of Von Mises stress, equivalent strain, and displacement to obtain information about how much the knife blade deforms under the load given above.

If a load F = 250 N is considered, the following results will be obtained, as presented below. In Table 1, the operating conditions corresponding to Force 1 are summarized.

In Table 2, the Reaction Force and the moment at the Fixed Constraint are presented. The type of load consists of a force F = 250 N.

As a result of this action, a moment with a magnitude of 43.406 Nm is generated, distributed across the X, Y, and Z components, as shown in Table 2.

Table 1. *Operating conditions*

Load Type	Force value
Magnitude	250.000 N
Vector X	0.000 N
Vector Y	250.000 N
Vector Z	0.000 N

In the first step, the test side of the knife blade and a fixed constraint (the knife handle, the right part) are selected. In Figures 5 and 6, the selected testing face [15] and the fixed constraint are shown.

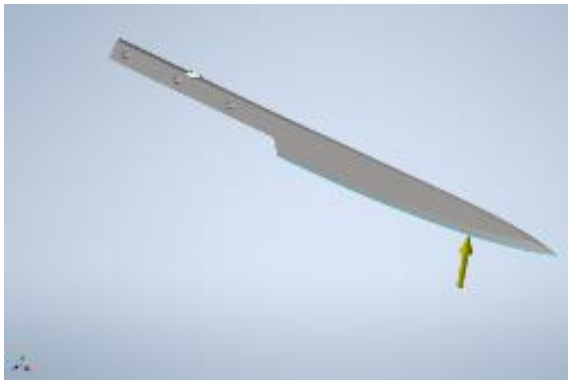

Fig. 5. *Selected testing face, corresponding to the specimen*

Table 2. *The Reaction Force and the moment at the Fixed Constraint*

Reaction Force		Reaction Moment		Constraint Name
Magnitude	Component (X, Y, Z)	Magnitude	Component (X, Y, Z)	
250 N	0 N	43.406 Nm	-0.500186 Nm	Fixed Constraint: 2
	-250 N		0 Nm	
	0 N		-43.403 Nm	

Fig. 6. *Fixed Constraint 2*

In Figure 7, the Von Mises Stress evolution is presented. The minimum value corresponding to the Von Mises Stress is 0.000351435 MPa and the maximum value is 582.919 MPa.

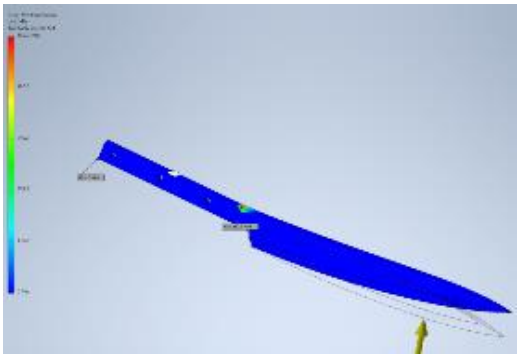

Fig. 7. *The Von Mises Stress evolution in the case of F = 250 N*

THE ANNALS OF "DUNAREA DE JOS" UNIVERSITY OF GALATI
FASCICLE IX. METALLURGY AND MATERIALS SCIENCE
No. 2 - 2026, ISSN 2668-4748; e-ISSN 2668-4756
Article DOI: https://doi.org/10.35219/mms.2026.2.03

This displacement signifies the minimal blade deformation under the given load (F = 250 N), highlighting its excellent rigidity and dimensional stability.

The maximum X-Displacement value in this case is 0.0829454 mm and the minimum value is -0.0609947 mm.

The maximum value corresponding to Y-Displacement is 1.1737 mm and the minimum value is -0.00069134 mm (Figures 8-10).

The total Displacement has a maximum value of 1.22852 mm (Figure 11).

The displacements have very small values; the knife blade used as a laboratory specimen does not deform plastically at this stress level.

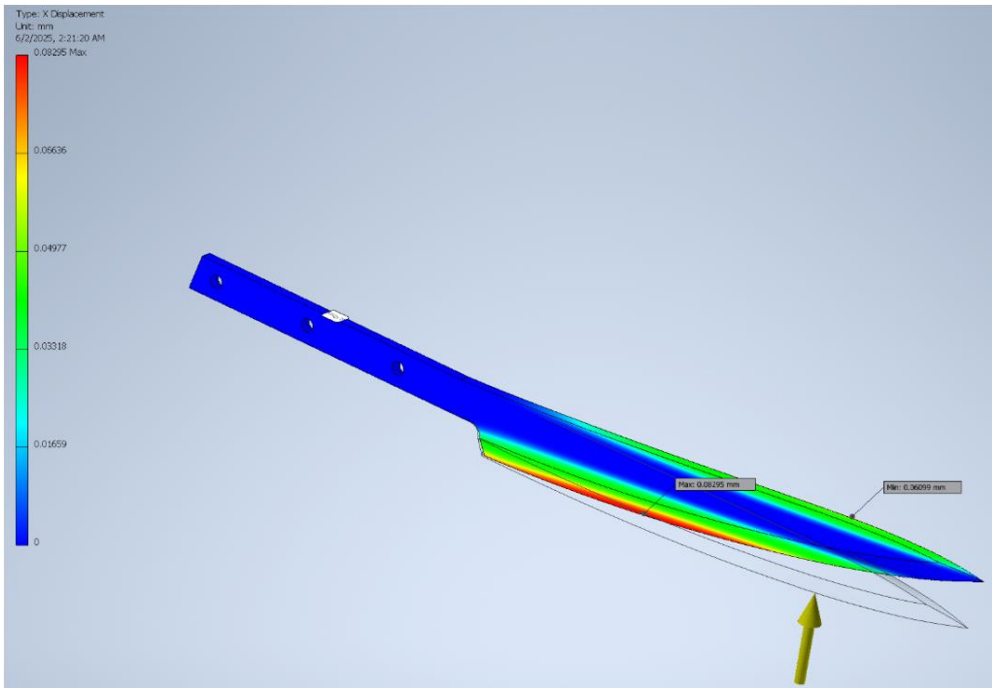

Fig. 8. *X-Displacement evolution*

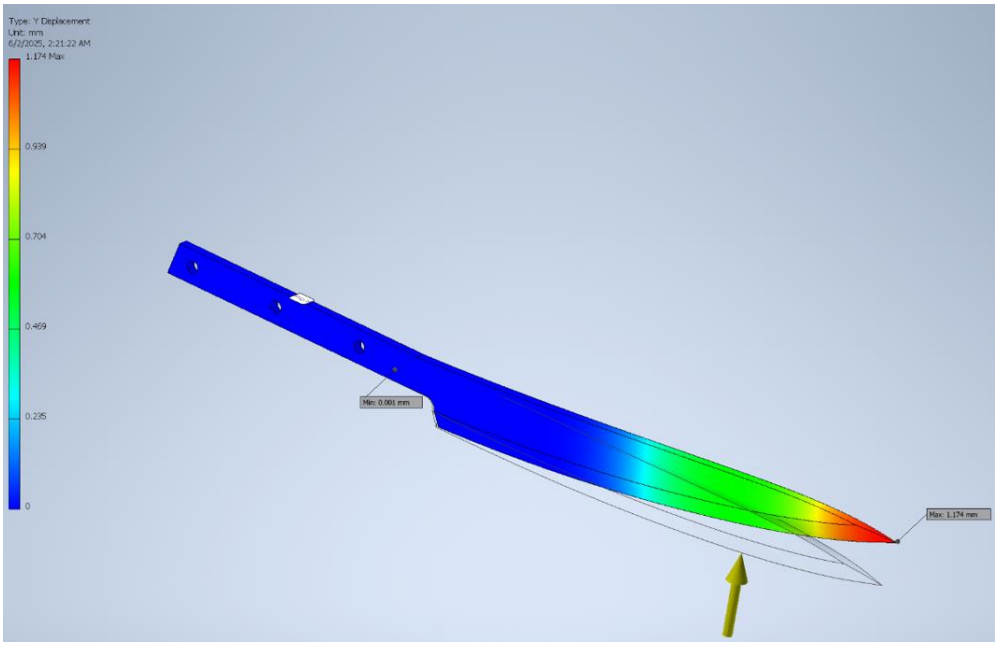

Fig. 9. *Y-Displacement*

THE ANNALS OF "DUNAREA DE JOS" UNIVERSITY OF GALATI
FASCICLE IX. METALLURGY AND MATERIALS SCIENCE
No. 2 - 2026, ISSN 2668-4748; e-ISSN 2668-4756
Article DOI: https://doi.org/10.35219/mms.2026.2.03

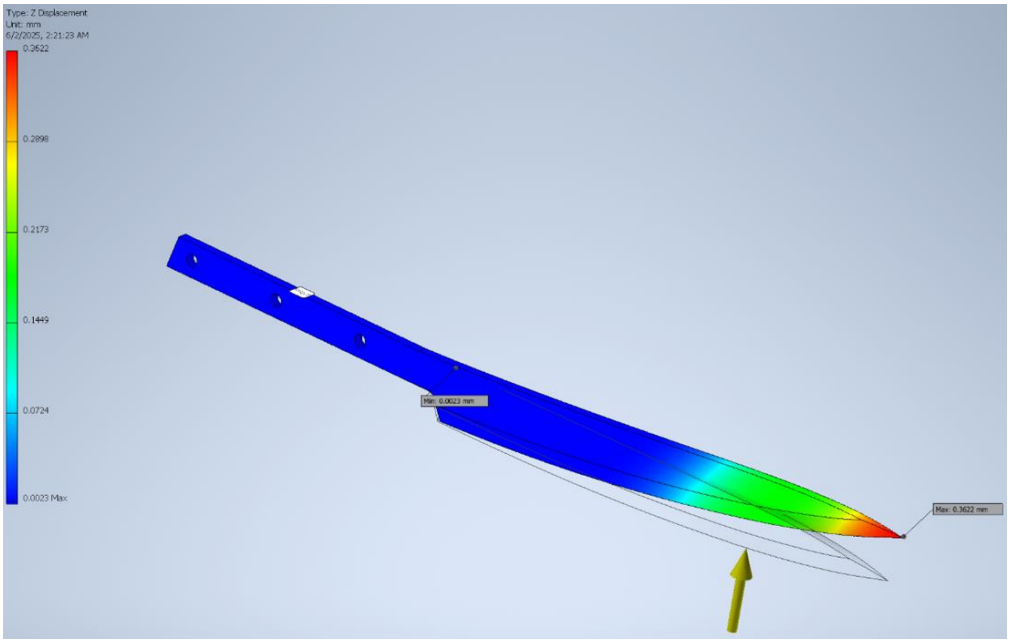

Fig. 10. *Z-Displacement*

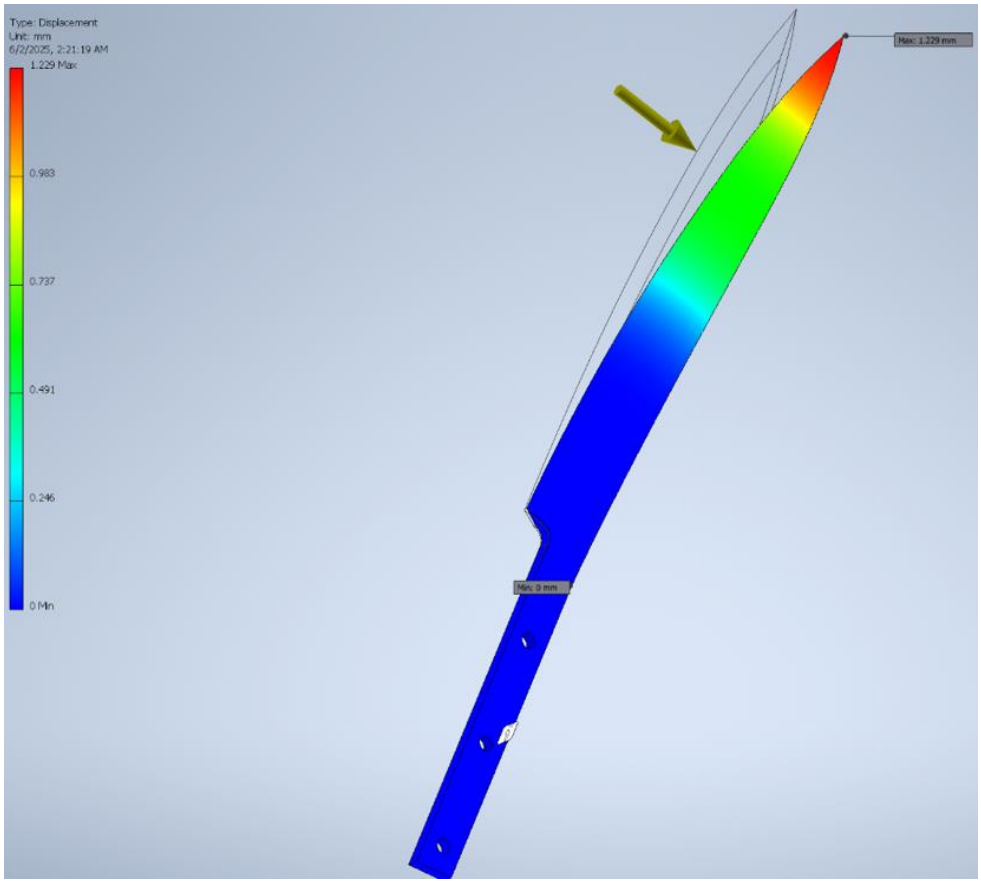

Fig. 11. *The Displacement of the sample during the action of the Load (F = 250 N) corresponding to the First Principal Stress*

Considering that a "displacement" of the blade is still achieved during loading, it can be observed that the Damascus steel made in the laboratory has very little elasticity. No plastic deformations were recorded during this loading.

4. Conclusion

The objective was to create Damascus steel in the laboratory. The original recipe was lost at the end of the 16th century.

Searching the specialized literature, laboratory tests for this type of steel were found, as well as tests carried out on original swords from the 14th-16th centuries. The structure of the original steel from the 16th century was compared with the specimens obtained in the laboratory.

After performing the heat treatment, the Brinell hardness of the Damascus steel obtained in the laboratory increased from 197 daN/mm^2 to 698 daN/mm^2.

Additional studies, such as finite element analysis and the evaluation of material strength properties, were carried out using Autodesk Inventor Professional 2023.

By stacking plates of different high-carbon steels and using hot forging, a Damascus steel with excellent strength properties was obtained.

The steel made in the laboratory performed exceptionally well at a load value of 250 N.

References

[1]. Sukhanov D. A., *et al.*, *Carbide banding as the basis for the Damascus structure of the 18th century Persian blade steels*, Metallurgist, Springer Nature, June 2025.

[2]. Sukhanov D. A., *Morphological features of carbide banding in high-carbon steels with bulat structure*, Metallurg, vol. 1, p. 103-111, 2023.

[3]. Zschokke B., *Du Damasse et des Lamés de Damast*, Revue Metalurgie, 21, p. 635-669, 1924.

[4]. Verhoeven J. D., *et al.*, *The Key Role of Impurities in Ancient Damascus Steel Blades*, Archaeotechnology, JOM, vol. 50, p. 58-64, September 1998.

[5]. Sherby O. D, Wadsworth J., *Damascus steel*, Scientific American, 252 (2), p. 112-120, 1985.

[6]. Peterson D. T, *et al.*, *Damascus steel: characterization of one Damascus steel sword*, Materials Characteristics, vol. 24, issue 4, p. 355-374, 1990.

[7]. Panseri C., *Damascus steel in legend and in reality*, rev. Gladius, Nb. IV, p. 5-66, 1965.

[8]. Verhoeven J. D., *The mystery of Damascus blades*, Scientific American, 284, Article Number: 74, 2001.

[9]. Perttula J., *Reproduced wootz damascus steel*, Scand J Met 30 (2), p. 65-68, 2001.

[10]. Sukhanov D. A., Plotnikova N. V., *Mechanical properties of 18th century Persian bulat steel compared with modern tool steels*, Metallurg 11, p. 50-60, 2019.

[11]. Merico P., *et al.*, *Archaeo-metallurgical Investigation of a Fragment of a Medieval Sword Blade*, Metallography, Microstructure, and Analysis, vol. 13, p. 257-271, 2024.

[12]. Papadatu C. P., *et al.*, *Learning from the past: The reconstruction of the original Damascus Steel. Experimental Study*, International Journal of Conservation Science, ISSN: 2067-533X, 14, 3, p. 871-886, 2023.

[13]. Papadatu C. P., *et al.*, *Research on Testing a Genuine Damascus Steel. A Case Study*, International Journal of Conservation Science, ISSN: 2067-533X, vol. 14, issue 4, p. 1367-1380, 2023.

[14]. Papadatu C. P., *et al.*, *Graphic Modelling and Equipment used in the Reconstruction of the Original Damascus Steel*, International Journal of Conservation Science, 15 (2), p. 979-992, 2024.

[15]. Papadatu C.-P., Obreja D. B., *Simulation regarding the Damascus Steel Behavior on Mechanical Stress*, The Annals of "Dunarea de Jos" University of Galati, Fasc. IX, Metallurgy and Materials Science, vol. 48, issue 4, 2025.

THE ANNALS OF "DUNAREA DE JOS" UNIVERSITY OF GALATI
FASCICLE IX. METALLURGY AND MATERIALS SCIENCE
No. 2 - 2026, ISSN 2668-4748; e-ISSN 2668-4756
Article DOI: https://doi.org/10.35219/mms.2026.2.04

ASSESSMENT OF POLLUTANT LOAD AND POTENTIAL IMPACT OF THE SNOWPACK IN BRĂILA MUNICIPALITY

Nicoleta CIOBOTARU
"Dunarea de Jos" University of Galati, Faculty of Engineering and Agronomy,
Calarasi Street, 29, RO-810017, Braila, Romania
e-mail: nicoleta.ciobotaru@ugal.ro

ABSTRACT

Urban snowpack represents a highly effective matrix for monitoring atmospheric deposition, as it has the capacity to accumulate pollutants originating from anthropogenic activities during the cold season. The present study aims to assess the contamination levels of snow collected from different functional areas of the Brăila municipality, as well as to estimate the potential impact of pollutants on soil and surface waters during the melting period. Snow samples were collected from areas characterized by intense road traffic, residential zones, industrial sectors, and green spaces, in order to highlight the spatial variability of contaminants. Laboratory analyses included the determination of physicochemical parameters (pH, total dissolved solids, and electrical conductivity), major ionic species (Cl^-, SO_4^{2-}, NO_3^-, NH_4^+, Ca^{2+}, Mg^{2+}), and selected heavy metals (Pb, Cd, Fe), which are relevant indicators for identifying sources of urban pollution. The assessment of pollution levels was carried out using specific indices, such as the contamination factor and the pollution load index. The obtained results highlight the influence of anthropogenic activities on the chemical composition of urban snow and emphasize its role as a vector for pollutant transfer to soils and drainage systems during snowmelt. Ultimately, this study contributes to a better understanding of seasonal urban pollution processes and provides a scientific basis for the development of sustainable environmental management measures.

KEYWORDS: urban snow, atmospheric deposition, anthropogenic pollutants

1. Introduction

Urban environments are subject to increasing anthropogenic pressure generated by road traffic, residential heating, industrial activities, and processes associated with urban infrastructure. During the cold season, the snowpack represents an efficient natural matrix for capturing atmospheric pollutants, accumulating suspended particles, soluble ions, and heavy metals deposited through both wet and dry deposition processes [1]. Due to its high specific surface area and relatively long exposure period, snow acts as a short-term integrator of anthropogenic emissions, reflecting the level of atmospheric contamination in urban ecosystems.

Seasonal snow accumulation plays a dual role from an environmental perspective. On the one hand, it temporarily immobilizes atmospheric pollutants, reducing their concentrations in the air; on the other hand, during the melting period, it can generate a concentrated input of contaminants into the soil, surface waters, and urban drainage systems [2]. Numerous studies have reported elevated concentrations of chlorides, sodium, nitrates, sulphates, and heavy metals in urban snow, particularly in areas characterized by intense traffic and industrial activities [3].

The use of salt-based de-icing materials, vehicle component wear (brake pads, tires), fossil fuel combustion, and corrosion processes represent major anthropogenic sources influencing the chemical composition of the snowpack [4]. Consequently, chemical analysis of snow has become a relevant tool for identifying pollution sources, assessing the spatial distribution of contaminants, and estimating the risks associated with their transfer to environmental compartments during snowmelt. Parameters such as pH, electrical conductivity, concentrations of major ions, and heavy metal content are frequently used as indicators of urban anthropogenic pressure [5].

THE ANNALS OF "DUNAREA DE JOS" UNIVERSITY OF GALATI
FASCICLE IX. METALLURGY AND MATERIALS SCIENCE
N°. 2 - 2026, ISSN 2668-4748; e-ISSN 2668-4756
Article DOI: https://doi.org/10.35219/mms.2026.2.04

The Brăila municipality, located in southeastern Romania, represents a relevant case study due to its mixed urban–industrial profile, increasing road traffic intensity, residential heating practices, and proximity to the Danube River. Specific climatic conditions in the region favour seasonal snow accumulation, providing an opportunity for the integrated assessment of atmospheric deposition. However, data regarding the chemical composition of urban snow in medium-sized Romanian cities remain limited, highlighting the need for systematic investigations.

The present study aims to characterize the physicochemical composition of urban snow collected from various functional areas of Brăila municipality, analyse the spatial variability of major ions and heavy metals, identify potential anthropogenic sources of contamination, and evaluate the implications for soil and surface waters in the context of snowmelt. The findings contribute to understanding the seasonal dynamics of contaminants in urban ecosystems and support the development of sustainable environmental management strategies.

2. Materials and methods

2.1. Study area and sampling selection

The study was conducted in the municipality of Brăila, located in southeastern Romania, which is characterized by a temperate continental climate with cold winters favourable to snow accumulation [6]. To highlight the spatial variability of urban pollutants, four types of functional areas were selected:

- High-traffic areas: The Dorobanților Blvd.–Calea Călărași intersection; the Buzăului Road–Vizirului Road intersection; the Calea Călărași–Independenței Blvd. intersection; the Historic Centre; and a shopping centre parking area (Vărsătura);
- Residential areas: The Radu Negru neighborhood – one sample collected from a yard and one from the street;
- Industrial areas: The Chiscani chemical platform and the Brăila Shipyard;
- Green spaces: Monument Park – one sample collected from the interior and one from the park entrance (Buzăului Road).


Monument Park


Călărași – Independenței intersection


Radu Negru neighbourhood


Chiscani chemical platform

Fig. 1. *Fresh snow sampling areas (Brăila, February 2026)*

For each type of area, three fresh snow samples were collected, as illustrated in Figure 1. The sampling locations are presented on the map of Brăila municipality in Figure 2.

2.2. Sampling and preservation

Snow samples were collected from the upper layer (0-5 cm) to avoid contamination from the soil or previously accumulated dust. Each sample (~0.5 kg) was placed in a sealed polyethylene bag and labelled with the sample code, date, and location. The snow was allowed to melt at room temperature under sealed conditions to obtain an aqueous extract. The resulting volume was measured and homogenized. In the laboratory, samples were stored at a constant temperature of 4 °C prior to analysis.

THE ANNALS OF "DUNAREA DE JOS" UNIVERSITY OF GALATI
FASCICLE IX. METALLURGY AND MATERIALS SCIENCE
N°. 2 - 2026, ISSN 2668-4748; e-ISSN 2668-4756
Article DOI: https://doi.org/10.35219/mms.2026.2.04

2.3. Analytical Methods

The collected snow samples were analysed for physicochemical parameters, selected ions, and heavy metals, as follows:

- pH: potentiometric method;
- Total dissolved solids (TDS) and electrical conductivity (EC): conductometric method;
- Cl^-: volumetric method with potassium chromate;
- SO_4^{2-}, NO_3^-, NH_4^+: spectrophotometric methods;
- Ca^{2+}, Mg^{2+}: volumetric method with murexide and Eriochrome Black T indicators, respectively;
- Pb, Cd, Fe: spectrophotometric methods.

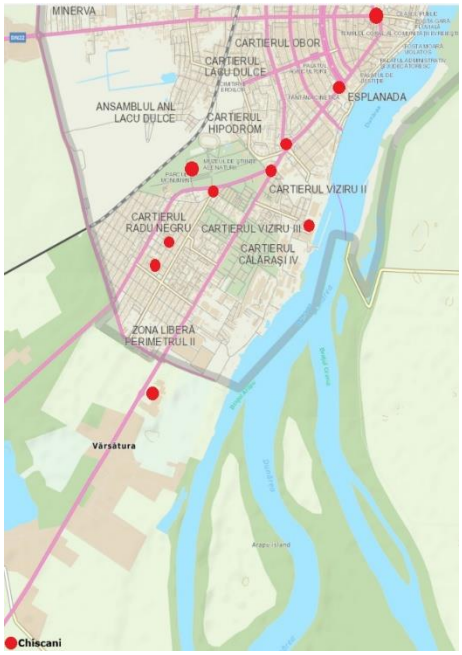

Fig. 2. *Snow sampling locations mapped in Brăila* [7]

3. Results and Discussion

3.1. Physicochemical parameters

The analysis of snow samples collected from the Brăila municipality reveals significant variations in physicochemical parameters, pH, total dissolved solids (TDS), and electrical conductivity (EC), depending on land use type and potential pollution sources, as shown in Table 1. The pH values ranged between 5.37 and 6.42, indicating a generally mild acidity. This acidity is typical of urban precipitation and can be associated with atmospheric pollutants such as nitrogen oxides (NOx) and sulphur dioxide (SO_2), originating primarily from road traffic and industrial activities [8]. The lowest pH values were recorded in high-traffic areas and near the former Chiscani chemical platform, suggesting a strong anthropogenic influence. In contrast, values closer to neutrality in the residential area (Radu Negru – street) and inside Monument Park may be explained by the presence of alkaline mineral particles in the atmosphere from soil resuspension, road dust, and construction materials.

Table 1. *Physicochemical parameters of snow samples*

Analyzed area	pH	TDS (mg/L)	EC (µS/cm)
Dorobanților – Călărașilor Road	5.37	10.5	6.72
Buzăului Road – Vizirului Road	5.62	13.0	8.32
Călărașilor Road – Independenței	5.86	20.1	12.86
Historic Center	5.97	3.7	2.37
Shopping center parking	5.41	63.9	40.90
Radu Negru – yard	5.91	7.9	5.06
Radu Negru – street	6.42	3.4	2.18
Chiscani chemical platform	5.39	42.2	27.01
Brăila Shipyard	5.75	9.5	6.08
Monument Park – interior	6.10	10.5	6.72
Monument Park – entrance	5.96	23.6	15.10

These particles, rich in carbonates (especially $CaCO_3$), can neutralize acidic compounds, leading to increased pH values [9]. Regarding total dissolved solids (TDS), values ranged widely from 3.4 mg/L to 63.9 mg/L, reflecting variability in the dissolved pollutant load. The highest values were recorded in the shopping centre parking area (63.9 mg/L), followed by the Chiscani chemical platform (42.2 mg/L), indicating significant pollutant accumulation. These levels can be attributed to intense anthropogenic activities, including traffic emissions, particulate deposition, and potential industrial discharges.

In contrast, the lowest TDS values were observed in residential areas and in the Historic Centre, suggesting reduced contamination or more efficient dispersion. Electrical conductivity (EC) shows a similar trend, confirming the direct relationship between these parameters. EC values ranged from 2.18 µS/cm to 40.90 µS/cm, with the

THE ANNALS OF "DUNAREA DE JOS" UNIVERSITY OF GALATI
FASCICLE IX. METALLURGY AND MATERIALS SCIENCE
N°. 2 - 2026, ISSN 2668-4748; e-ISSN 2668-4756
Article DOI: https://doi.org/10.35219/mms.2026.2.04

highest values corresponding to areas previously identified with elevated TDS. Thus, the shopping centre parking area and the industrial platform represent critical points in terms of ionic load, while green and residential areas exhibit lower values, closer to the natural background levels.

Comparative analysis by land-use type shows that high-traffic and industrial areas exhibit higher TDS and EC values, confirming the impact of anthropogenic activities on precipitation quality [8]. In contrast, green spaces, particularly inside Monument Park, show lower values, making them suitable as reference areas for natural background conditions. The differences observed between the park entrance and its interior suggest the influence of traffic from adjacent areas on snow quality. The results highlight a clear correlation between land use and snow pollution levels, demonstrating that snow can serve as a reliable indicator of air quality and atmospheric deposition in urban environments [9].

The pH values (5.37–6.42) indicate a slightly acidic character of the snow, which, upon melting, may contribute to local soil acidification and to the mobilization of certain metals, particularly in areas with intense traffic and industrial activity. The concentrations of dissolved salts and the corresponding electrical conductivity values, which are higher in anthropogenically influenced areas (e.g., parking lots, industrial platforms), suggest an increased input of salts and dissolved compounds that may infiltrate into the soil and subsequently reach surface waters through runoff. Although no specific regulatory limits exist for snow, these results can be tentatively correlated with water quality requirements [10, 11], which impose the maintenance of an appropriate physico-chemical balance in water bodies. Thus, the analysed snow represents a diffuse source of pollution, with a potentially moderate, yet relevant impact in an urban context.

3.2. Major ion concentrations

The analysis of major ions in snow samples collected from Brăila highlights the variable influence of anthropogenic activities on precipitation chemistry.

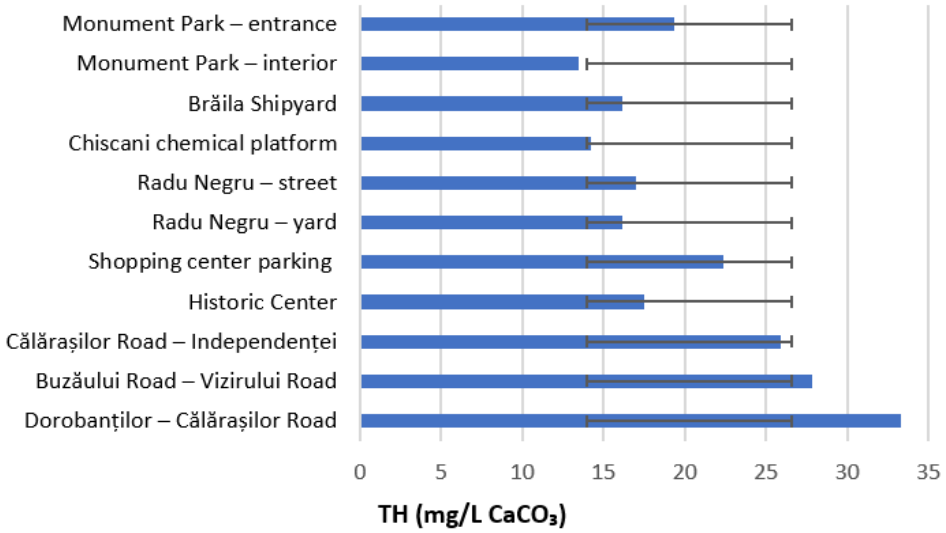

Fig. 3. *Total hardness (TH) in the studied snow samples*

In high-traffic areas, such as Dorobanților Blvd.–Calea Călărași and the Vărsătura parking area, chloride (Cl^-, 35–57 mg/L) and sulphate (SO_4^{2-}, 22–26 mg/L) concentrations are significantly higher compared to those in green areas, reflecting contributions from road traffic and industrial aerosols.

The presence of chlorides (Cl^-) identified in snow samples collected from high-traffic areas, such as major intersections and large parking lots, can be largely attributed to the use of de-icing agents based on salts such as NaCl, $CaCl_2$, and $MgCl_2$, applied to prevent ice formation and ensure traffic safety. These salts readily dissolve during snowmelt, leading to increased Cl^- concentrations in the resulting meltwater and, consequently, in soils and surface waters. This phenomenon may result in increased soil salinity, alterations in the ionic balance of aquatic ecosystems, and adverse effects on chloride-sensitive organisms [12]. Nitrates (NO_3^-, 0.5–1.4 mg/L) and ammonium (NH_4^+, 0.85–1.05 mg/L) indicate a moderate influence of nitrogen oxides originating from traffic, as well as, to some extent, from agricultural and industrial sources, while also contributing to the partial neutralization of acidity. In residential areas, ion concentrations are lower (Cl^- 30–32 mg/L; SO_4^{2-} 15–16 mg/L), suggesting a

THE ANNALS OF "DUNAREA DE JOS" UNIVERSITY OF GALATI
FASCICLE IX. METALLURGY AND MATERIALS SCIENCE
N°. 2 - 2026, ISSN 2668-4748; e-ISSN 2668-4756
Article DOI: https://doi.org/10.35219/mms.2026.2.04

reduced anthropogenic impact. In contrast, the Chiscani chemical platform and the shipyard exhibit elevated SO_4^{2-} and NH_4^+ levels, highlighting direct industrial inputs. Green areas, particularly the interior of Monument Park, record the lowest values for all measured ions, indicating conditions close to the natural background and a greater capacity for pollutant filtration.

Alkaline ions, Ca^{2+} and Mg^{2+}, present especially in urban and industrial areas, originate from mineral dust, resuspended soil, and construction materials, and play an essential role in the neutralization of precipitation acidity, which correlates with pH values closer to neutrality in residential areas and parks [8, 9]. This neutralization reduces the immediate impact of acidity on soils and surface waters; however, elevated Cl^- and SO_4^{2-} levels in traffic-affected and industrial areas may contribute to increased soil salinity and surface water conductivity, promoting metal mobilization and alterations in the ecological balance [8].

During snowmelt, within impervious areas, dissolved ions are transported to adjacent soils and urban drainage networks, which may affect both soil structure and water quality. Although the determined values do not exceed the permissible limits regulated for precipitation, it is necessary to maintain an appropriate physico-chemical balance of surface waters and to protect aquatic ecosystems through recurrent monitoring. All total hardness (TH) values are below 40 mg/L $CaCO_3$, indicating low hardness levels that fall within the maximum permissible concentrations. High-traffic areas and parking lots (e.g., Dorobanților Boulevard, Vărsătura) exhibit higher hardness values (22–33 mg/L $CaCO_3$), as well as higher concentrations of Ca^{2+} and Mg^{2+} ions, likely due to urban dust and the resuspension of construction materials. Industrial areas and green spaces (Chiscani, park interior) show lower TH values (13–16 mg/L $CaCO_3$), closer to natural background conditions. Low-hardness precipitation contributes less to the formation of calcareous deposits in soils or drainage systems.

3.3. Heavy metals

Figure 4 presents the analysis of heavy metals Pb, Cd, and Fe in snow samples from the city of Brăila. The results highlight a distribution of the analysed metals correlated with the degree of anthropogenic influence and the type of area. High-traffic and industrial zones exhibit higher concentrations of lead and cadmium, suggesting a continuous input of atmospheric pollutants from road traffic and industrial sources, including fossil fuel emissions, tire wear, construction materials, and industrial processes [13, 14].

Iron (Fe) concentrations are higher in the Chiscani chemical platform and the shipyard (180–200 µg/L), indicating deposition associated with industrial activities and the presence of iron in urban aerosols and dust. In contrast, residential areas and green spaces, such as Radu Negru District and Monument Park, exhibit much lower concentrations (Pb 7–10 µg/L; Cd 2.5–3 µg/L; Fe 50–65 µg/L), approaching natural background levels for precipitation and reflecting a moderate anthropogenic impact. Heavy metals in snow represent a potential risk to soils and surface waters. During snowmelt, Pb, Cd, and Fe can be transported into soils and drainage systems, where they may alter soil chemical properties, influence nutrient availability, and affect aquatic ecosystems through bioaccumulation or direct toxicity [15]. High-traffic and industrial areas pose a greater risk, whereas green and residential zones act as buffer areas, reducing pollutant input to the urban and aquatic environment.

The determined concentrations of heavy metals in the collected snow samples do not exceed the permissible limits established by water quality and soil protection legislation [11, 16].

Table 2. *Major ion concentrations (mg/L)*

Area	Cl^-	SO_4^{2-}	NO_3^-	NH_4^+	Ca^{2+}	Mg^{2+}
Dorobanților – Călărași Road	35.45	26	0.9	0.85	10.2	1.89
Buzăului Road – Vizirului Road	49.63	24	1.1	0.95	8.5	1.6
Călărași Road – Independenței	49.63	23	1.2	1.00	7.9	1.5
Historic Center	33.46	18	0.7	0.60	5.2	1.1
Shopping center parking	56.72	22	1.4	1.05	6.01	1.78
Radu Negru – yard	30.4	15	0.6	0.50	4.8	1.0
Radu Negru – street	31.54	16	0.7	0.55	5.0	1.1
Chiscani chemical platform	42.54	24	0.9	1.56	3.61	1.26
Brăila Shipyard	28.36	30	1.0	0.80	4.5	1.2
Monument Park – interior	21.27	12	0.5	0.40	3.9	0.9
Monument Park – entrance	34.24	20	0.8	0.70	5.6	1.3

THE ANNALS OF "DUNAREA DE JOS" UNIVERSITY OF GALATI
FASCICLE IX. METALLURGY AND MATERIALS SCIENCE
N°. 2 - 2026, ISSN 2668-4748; e-ISSN 2668-4756
Article DOI: https://doi.org/10.35219/mms.2026.2.04

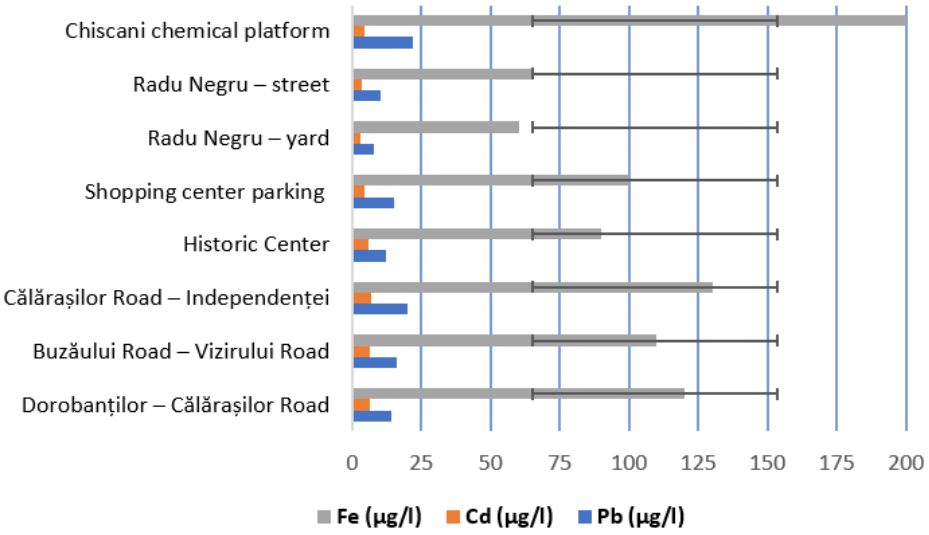

Fig. 4. *Concentrations of Pb, Cd, and Fe in the studied snow samples*

4. Conclusions

According to the chemical analysis of snow collected in the city of Brăila, the following observations were made:

- Slightly acidic pH values (5.37–6.42) reflect the input of atmospheric pollutants from traffic and industrial areas, while residential areas and green spaces show values closer to neutrality due to the presence of alkaline mineral particles that contribute to neutralization.
- Higher total dissolved salts and electrical conductivity in parking lots and industrial platforms indicate an increased input of dissolved salts and urban-industrial pollutants. Green and residential areas show lower values, reflecting a reduced anthropogenic impact and a natural filtration capacity.
- The presence of Cl^-, SO_4^{2-}, and NO_3^- ions highlight the influence of traffic and industrial activities, while NH_4^+ partially contributes to acidity neutralization.
- The analysed metals (Pb, Cd, Fe) exhibit the highest concentrations in high-traffic and industrial areas, likely due to vehicle wear or corrosion processes; however, in the analysed samples, the presence of these metals indicates moderate anthropogenic deposition. In residential areas and green spaces, values are close to natural background levels, suggesting a low impact.

Snow acts as a vector of diffuse pollution, transporting ions and heavy metals to soils and surface waters. In urban and industrial areas, this phenomenon can lead to partial acidification, increased soil salinity, and metal mobilization, affecting aquatic ecosystems and soil structure. Therefore, continuous monitoring of snow and precipitation is recommended to identify trends in urban and industrial pollution, alongside the promotion and maintenance of green spaces, which serve as buffer zones and natural filters for pollutants.

A comparative analysis of the physico-chemical parameters and the concentrations of major ions and heavy metals in snow samples collected in the city of Brăila indicates that all determined values fall within the limits established by current legislation regarding the discharge of wastewater into sewer networks and natural receptors [17-19]. Furthermore, a comparison with surface water quality standards shows that the levels of the analysed heavy metals (Pb, Cd, Fe) do not exceed indicative ecological risk thresholds. Nevertheless, they may contribute in the long term to alterations in soil properties and to an increased pollutant load in surface waters, particularly under conditions of repeated snow deposition and melt events.

Therefore, it can be concluded that, although spatial variations are determined by anthropogenic influences (traffic, industrial activities, and the use of de-icing materials), the analysed snow does not exhibit contamination levels exceeding the maximum permissible concentrations, and the potential impact on soils and surface waters remains generally low to moderate, which is characteristic of an urban environment.

References

[1]. Sakai H., *et al.*, *Heavy metal concentrations in urban snow as an indicator of air pollution*, Science of the Total Environment, 77(2-3), p. 163-174, 1988.
[2]. Rangel-Alvarado R., *et al.*, *Snow particles physiochemistry: feedback on air quality, climate change, and human health*, Environmental Science: Atmospheres, 2, p. 891-920, 2022.

[3]. Kuoppamäki K., *et al.*, *Urban snow indicates pollution originating from road traffic*, Environmental Pollution, 195, p. 56-63, 2014.
[4]. Vijayan A., *et al.*, *Traffic-related metals in urban snow cover: A review of the literature data and the feasibility of filling gaps by field data collection*, Science of the Total Environment, 920, 170640, 2024.
[5]. Kozhevnikov A. Y., *et al.*, *Dynamics of pollutants accumulation in the snow of an urban agglomeration*, Polar Science, 2024.
[6]. ***, *Climate data for Brăila, Romania*, Climate-Data.org (n.d.), https://en.climate-data.org/europe/romania/braila/braila-480/.
[7]. ***, *Harta digitală a municipiului Brăila*, Primăria Municipiului Brăila, (n.d.), https://braila-city.map2web.eu/
[8]. ***, *Acid rain and effects of acid rain*, United States Environmental Protection Agency (n.d.), Available at: https://www.epa.gov/acidrain.
[9]. Jacob D. J., *Introduction to atmospheric chemistry*, Princeton University Press, 1999.
[10]. ***, *Manual for the GAW precipitation chemistry programme*, World Meteorological Organization, 2004.
[11]. ***, *Legea apelor nr. 107/1996, privind utilizarea, protecția și gestionarea resurselor de apă*.
[12]. ***, *Ordinul nr. 161/2006, pentru aprobarea Normativului privind clasificarea calității apelor de suprafață în vederea stabilirii stării ecologice a corpurilor de apă*.
[13]. Szklarek S., *et al.*, *The effects of road salt on freshwater ecosystems and solutions for mitigating chloride pollution: A review*, Science of the Total Environment, 805, 150289, 2022.
[14]. Lu H., *et al.*, *Spatial heterogeneity of heavy metals contamination in urban road dust and associated human health risks*, Land, 14(4), 754, 2025.
[15]. Ariyarathna T., *et al.*, *Distribution and sources of heavy metals in stormwater: Influence of land use in Camden*, New Jersey, Land, 15(1), 154, 2026.
[16]. Alloway B. J., *Heavy metals in soils: Trace metals and metalloids in soils and their bioavailability*, Springer, 2013.
[17]. ***, *Ordinul nr. 756/1997, pentru aprobarea reglementării privind evaluarea poluării mediului*.
[18]. ***, *NTPA-001/2005 privind stabilirea limitelor de încărcare cu poluanți a apelor uzate industriale și urbane la evacuarea în receptorii naturali*, Monitorul Oficial al României, 2005.
[19]. ***, *NTPA-002/2002 privind condițiile de evacuare a apelor uzate în rețelele de canalizare ale localităților*, Monitorul Oficial al României, 2002.

THE ANNALS OF "DUNAREA DE JOS" UNIVERSITY OF GALATI
FASCICLE IX. METALLURGY AND MATERIALS SCIENCE
No. 2 - 2026, ISSN 2668-4748; e-ISSN 2668-4756
Article DOI: https://doi.org/10.35219/mms.2026.2.05

FAILURE CASE STUDY SERIES PART TWO: FAILURE ANALYSIS OF ROLLER GUIDES IN A WIRE ROD ROLLING MILL

Liviu GURĂU, Florin MARIN, Mihaela MARIN, Cristian ȘTEFĂNESCU, Gheorghe GURĂU*

Interdisciplinary Research Centre in the Field of Eco-Nano Technology and Advanced Materials CC-ITI, Faculty of Engineering, "Dunarea de Jos" University of Galati, 47 Domneasca Street, 800008 Galati, Romania
e-mail: gheorghe.gurau@ugal.ro

ABSTRACT

The paper aims to present the root cause of failure of roller guides from the wire rod and coil rolling mill during normal operation. A comprehensive failure investigation was conducted following standard metallurgical procedures, including visual inspection, hardness testing, chemical analysis, optical microscopy, stereomicroscopy, scanning electron microscopy (SEM–EDS) characterization, and inclusion rating according to ASTM E45. The investigation concludes that the primary root cause of failure was the use of D3 tool steel, which is unsuitable for components subjected to severe thermal cycling, resulting in progressive thermal fatigue damage and eventual catastrophic fracture. Moreover, the election of D2 or other Mo-V alloyed hot-work tool steels, combined with appropriate surface hardening, is recommended to enhance service life under rolling mill operating conditions.

KEYWORDS: failure analysis, thermal fatigue, roller guides, OM, SEM, EDS

1. Introduction

Roller guides in high-speed wire rod mills are subjected to extreme thermomechanical loading, given that billet temperatures routinely exceed 1000 °C while guide roll rotational velocities surpass 80–85 m/s. Moreover, these aggressive operating conditions amplify thermal gradients, surface oxidation, and vibrational stresses, all of which accelerate component degradation. Aside from the aforementioned effects, recent industrial analyses identify cooling water pressure instability, vapor film shielding, oil contamination within the cooling water, misalignment, and inadequate material selection as the most critical contributors to premature roller guide failure [1, 2, 14]. Above all, when cooling pressure drops below the ~0.5 MPa threshold or when water jets impinge at sub-optimal angles, persistent steam film layers develop, drastically diminishing heat extraction and fostering thermal fatigue fire cracking [1, 2].

Furthermore, complementary investigations across wire rod finishing units demonstrate that cobble events, gearbox bearing failures, overheating transients, and rapid load fluctuations intensify crack initiation by superimposing irregular stress cycles on already overheated surfaces [3, 15]. Correspondingly, studies addressing tungsten carbide and cast roll failures similarly correlate fire crack networks with repeated thermal cycling, showing that even modest increases in surface temperature accelerate crack propagation in line with classical thermal fatigue mechanisms [4, 5, 16]. Beyond that, both field observations and modeling research indicate that roll cooling configuration, oxide scale behavior, and surface residual stresses exert dominant control over crack advance rates in hot rolling environments [5, 16].

The material system used for roller guides likewise exerts a profound influence on service life. Cold-work tool steels standardized under ASTM A681 are commonly employed, with D2 and D3 frequently encountered in industrial guide roll fabrication [6, 7, 17]. Apart from compositional distinctions, these steels exhibit notable performance differences. D2, alloyed with molybdenum and vanadium, forms fine secondary carbides and demonstrates superior thermal fatigue resistance at elevated temperatures [7, 8, 18]. In contrast, D3 lacks Mo and V, relying instead on elevated carbon and chromium levels that promote coarse Cr-rich carbides. This microstructure yields high wear

THE ANNALS OF "DUNAREA DE JOS" UNIVERSITY OF GALATI
FASCICLE IX. METALLURGY AND MATERIALS SCIENCE
No. 2 - 2026, ISSN 2668-4748; e-ISSN 2668-4756
Article DOI: https://doi.org/10.35219/mms.2026.2.05

resistance at room temperature but results in low fracture toughness and poor high-temperature fatigue resistance [7, 8]. Moreover, recent studies show that D3's carbide dissolution behavior differs significantly from that of D2. Although multi-cycle austenitizing can improve hardness uniformity, it does not mitigate D3's intrinsic vulnerability to brittle thermal shock cracking [9, 10].

Furthermore, thermal spray and surface engineering approaches—including molybdenum-based coatings—have shown promising improvements in surface hardness and wear resistance for D-series substrates, offering potential as auxiliary life-extension strategies when base material limitations cannot be entirely eliminated [11, 19]. Correspondingly, modern fracture mechanics literature highlights that short-crack behavior, mixed-mode loading, and microstructure-sensitive crack growth models play central roles in predicting crack evolution in hot cyclic environments [12, 13, 20]. These insights align closely with SEM analyses of failed roller guides, which commonly exhibit beach marks, intergranular facets, micro-oxidized fire crack ligaments, and secondary branching—features characteristic of thermally driven fatigue.

Taken together, contemporary evidence demonstrates that improving roller guide reliability necessitates an integrated materials engineering and process control framework: (1) selecting Mo–V-bearing tool steels (e.g., D2) or alternative hot-work grades; (2) optimizing cooling jet pressure, geometry, and water cleanliness; and (3) applying surface hardening or thermal spray treatments to suppress crack nucleation under high-temperature cyclic contact conditions. Above all, this comprehensive methodology directly addresses the key root causes of premature failures in RM wire rod guide systems.

2. Experimental procedure

The chemical composition was determined with the optical emission spectrometer ARL 3460, driven by the new OXSAS analytical software. The equipment is designed to meet the specific needs of users in the metals industry, with OXSAS providing simple one-click routine analysis launch and full traceability. The test method (ASTM E415-21) facilitates the simultaneous determination of 21 alloying and residual elements in carbon and low-alloy steels. This method is suitable for routine control analysis in iron and steelmaking operations and can be applied to processed materials such as chill-cast, rolled, and forged specimens. The hardness test was performed with Universal Hardness Testing Machine KB150 R - Digital Rockwell. Stereo microscopy, optical microscopy, scanning electron microscopy (SEM) and energy dispersive X-ray spectroscopy (EDS) facilities were extensively presented in our previous work [21].

The material AISI D2 Tool Steel is a high-carbon, high-chromium tool steel alloyed with molybdenum and vanadium as per ASTM A 681 standard. It is the most widely used steel among the group D steels. It has high abrasive wear resistance, high compressive strength, good through-hardening properties, high stability during hardening, and good resistance to tempering-back. AISI D2 is often supplied in the annealed conditions.

3. Results and discussion

The analysis followed seven basic steps:

- Visual Inspection: The components were first examined for visible indicators such as fracture surface morphology, crack propagation patterns, discoloration, unusual wear, corrosion, bending, misalignment, or scoring marks that could suggest mechanical or environmental influence.
- Specimen Selection and Preservation: Critical areas of interest were carefully identified, marked, and preserved to ensure their integrity for detailed analysis.
- High-Stress Area Identification: Regions with potential high-stress concentration were assessed as likely crack initiation sites, providing key insight into the failure mechanism.
- Chemical Analysis and Standard Comparison: The chemical composition of the material was analyzed and compared against applicable standards to check for deviations or non-conformities.
- Hardness Testing: Hardness measurements were conducted and evaluated against standard requirements to detect abnormal hardness zones that may indicate improper processing.
- Optical Microscopy: Metallographic examination was performed to assess the steel's microstructure, inclusion content, and any signs of improper heat treatment, abnormal grain structure, or internal cleanliness issues.
- Scanning Electron Microscopy (SEM) and EDS Analysis: SEM analysis, coupled with Energy Dispersive Spectroscopy (EDS), was used to study the fracture surface at high magnification, identifying crack initiation points, fracture modes (e.g., brittle or ductile), and any compositional anomalies at the crack origin.

3.1. Visual inspection

The guides failed during normal operation without any blockages in the rolling process (Figure 1). Visual inspection revealed prominent fire cracks on the rolling face of the component. These thermally

THE ANNALS OF "DUNAREA DE JOS" UNIVERSITY OF GALATI
FASCICLE IX. METALLURGY AND MATERIALS SCIENCE
No. 2 - 2026, ISSN 2668-4748; e-ISSN 2668-4756
Article DOI: https://doi.org/10.35219/mms.2026.2.05

induced surface cracks are typically caused by rapid and repeated heating and cooling cycles during rolling operations, leading to localized thermal fatigue (Figure 2).

Such fire cracks serve as stress concentrators and can significantly reduce the fatigue resistance of the material. Under cyclic loading, they provide favourable conditions for fatigue crack initiation and propagation, which can ultimately result in premature fatigue failure of the component.

Fig. 1. *Broken guide at site*

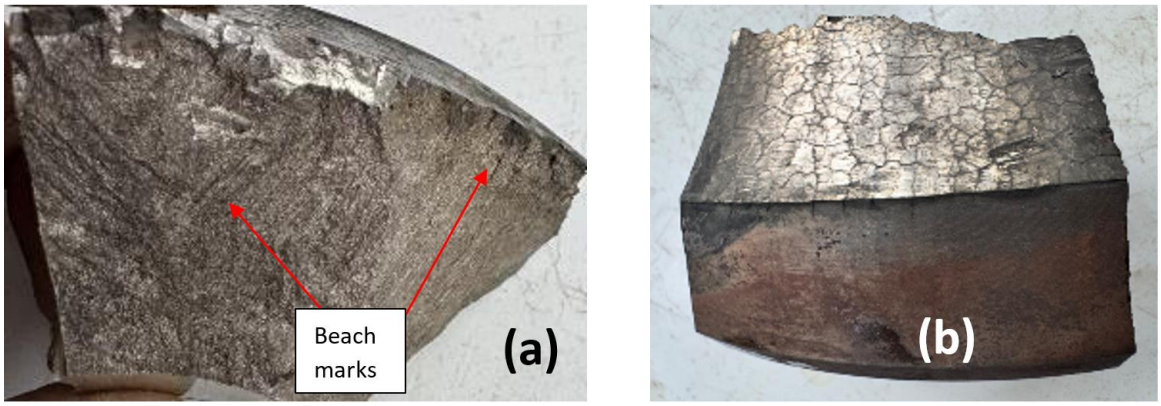

Fig. 2. *Failure surface: beach marks (a), fire cracks (b)*

Visual inspection revealed prominent fire cracks on the rolling face of the component. These thermally induced surface cracks are typically caused by rapid and repeated heating and cooling cycles during rolling operations, leading to localized thermal fatigue.

Such fire cracks serve as stress concentrators and can significantly reduce the fatigue resistance of the material. Under cyclic loading, they provide favourable conditions for fatigue crack initiation and propagation, which can ultimately result in premature fatigue failure of the component.

3.2. Chemical analysis

A Thermo Scientific ARL 3460 Advantage optical emission spectrometer was employed to quantify the elemental composition, using the ASTM E415-21 standard procedure for spark atomic emission analysis of carbon and low-alloy steels [21].

According to chemical composition determined in Spectral test machine the Steel Grade used for Roller guide is specific steel grade D2 - ASTM-A681-08-Standard-Specification-For-Alloy-Tool-Steel-Cold-work-Hot-Work-Plastic (Table 1).

Impact of Molybdenum in Tool Steel for High-Temperature Applications: Molybdenum (Mo) plays a critical role in enhancing the high-temperature performance of tool steels, especially those used in hot working applications such as rolling mill rolls, forging dies, and extrusion tools. Its addition brings several metallurgical benefits that directly improve resistance to thermal fatigue, a common failure mechanism in these environments.

THE ANNALS OF "DUNAREA DE JOS" UNIVERSITY OF GALATI
FASCICLE IX. METALLURGY AND MATERIALS SCIENCE
No. 2 - 2026, ISSN 2668-4748; e-ISSN 2668-4756
Article DOI: https://doi.org/10.35219/mms.2026.2.05

Metallurgical Contributions of Molybdenum are the following: Improved High-Temperature Strength and Creep Resistance; Forms stable carbides (e.g. Mo_2C) that maintain hardness and strength at elevated temperatures; Reduces softening during cyclic heating, preserving the tool's structural integrity. Thermal Fatigue Resistance: Molybdenum increases the hot hardness and improves resistance to thermal cycling, which is essential for preventing surface crack initiation (fire cracks); It delays crack propagation by enhancing the steel's toughness and resistance to microstructural degradation under thermal stress. Reduced Thermal Expansion Mismatch: Molybdenum contributes to a more stable microstructure during heating and cooling cycles, minimizing thermal strain and associated fatigue cracking. Carbide Stability and Secondary Hardening: Molybdenum supports the formation of finely dispersed carbides, improving wear resistance without excessive brittleness. Promotes secondary hardening during tempering, further enhancing thermal resistance. Resistance to Tempering Embrittlement: Mo helps prevent temper embrittlement and intergranular cracking under prolonged service at high temperatures.

Table 1. *Roller guide chemical composition*

Element	Composition Range (wt.%)	D2 - ASTM-A681-08	D3 -ASTM-A681-08
Carbon (C)	2.125	1.4-1.6	2.0-2.35
Manganese (Mn)	0.303	0.1-0.6	0.10-0.60
Phosphorus (P)	0.04	Max 0.030	Max 0.030
Sulfur (S)	0.028	Max 0.030	Max 0.030
Silicon (Si)	0.655	0.10-0.60	0.10-0.60
Chromium (Cr)	12.213	11.0-13.00	11.0-13.00
Nickel (Ni)	0.135	Ni + Cu max 0.75%	Ni + Cu max 0.75%
Aluminum (Al)	0.0041	-	
Nitrogen (N)	0.0120	-	
Molybdenum (Mo)	0.0261	0.7-1.20	Max 1.0
Vanadium (V)	0.024	0.50-1.0	Max 1.0
Titanium (Ti)	0.0132		
Copper (Cu)	0.070	Ni + Cu max 0.75%	Ni + Cu max 0.75%
Cev	4.64	-----	-----

Overall, molybdenum is a key alloying element in tool steels used for high-temperature applications due to its ability to increase thermal fatigue resistance, maintain hardness under heat, and improve structural stability. Its inclusion is essential in environments where tools are exposed to cyclic thermal loading, helping prevent fire cracks and fatigue failures, and thus extending the tool's service life.

3.3. Hardness Test

Hardness testing was performed on the roller surface [rolling face] region as well as the core region to evaluate potential hardness variations. However, no significant difference could be observed between the two regions. Both areas revealed very high hardness, on the order of approximately 60 HRC (Figure 3).

THE ANNALS OF "DUNAREA DE JOS" UNIVERSITY OF GALATI
FASCICLE IX. METALLURGY AND MATERIALS SCIENCE
No. 2 - 2026, ISSN 2668-4748; e-ISSN 2668-4756
Article DOI: https://doi.org/10.35219/mms.2026.2.05

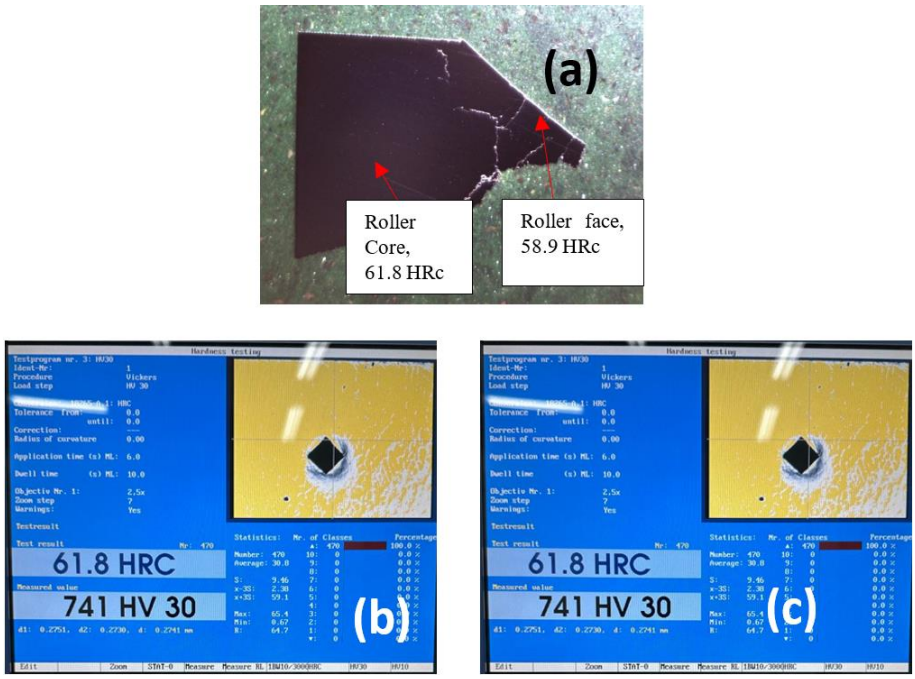

Fig. 3. *Vickers and Rockwell hardness (a) roller core, (b) roller side*

3.4. Stereomicroscopy

Stereomicroscopy plays an important role in failure analysis, quality control, and industrial applications (Figure 4). With its high depth perception, large working distance, and ease of use, it remains an essential instrument across multiple scientific and technical fields.

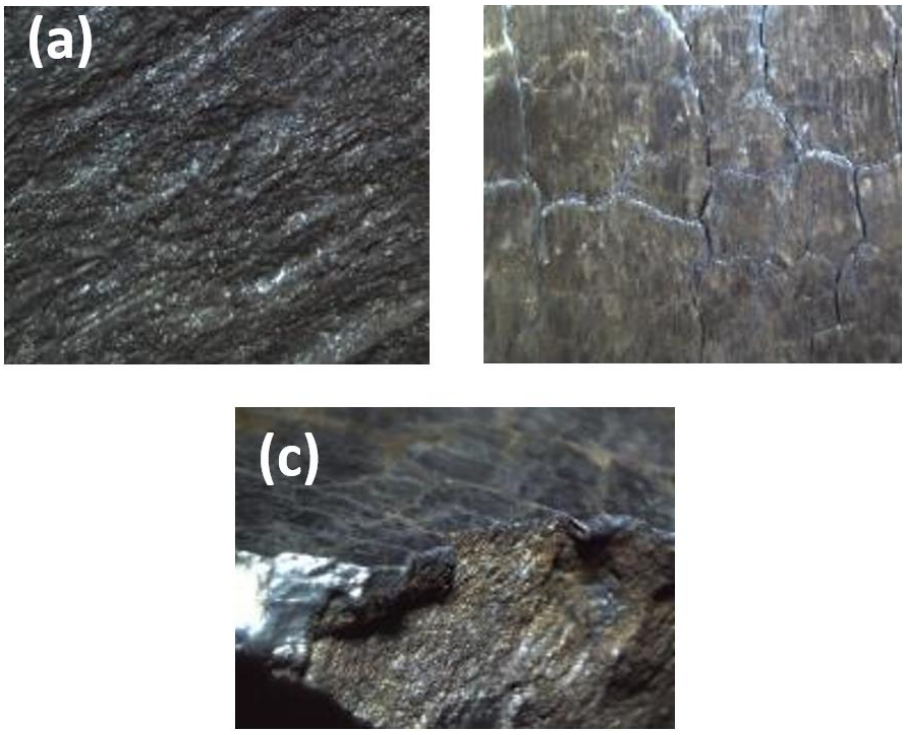

Fig. 4. *Beach marks visible on the fracture surface (a); Prominent fire cracks observed all around the rolling face of roller guide (b); Separation (fracture) found to be occurring along fire crack planes (c)*

THE ANNALS OF "DUNAREA DE JOS" UNIVERSITY OF GALATI
FASCICLE IX. METALLURGY AND MATERIALS SCIENCE
No. 2 - 2026, ISSN 2668-4748; e-ISSN 2668-4756
Article DOI: https://doi.org/10.35219/mms.2026.2.05

3.5. Optical microscopy

The cross-sectional sample was polished up to 1500-grit emery paper, followed by 1 µm velvet cloth polishing, and then etched using a 2% nital solution to reveal the microstructures and observe defects. The micro-examination carried out in accordance with ASTM E407 and the ASM Handbook, Volume 9.

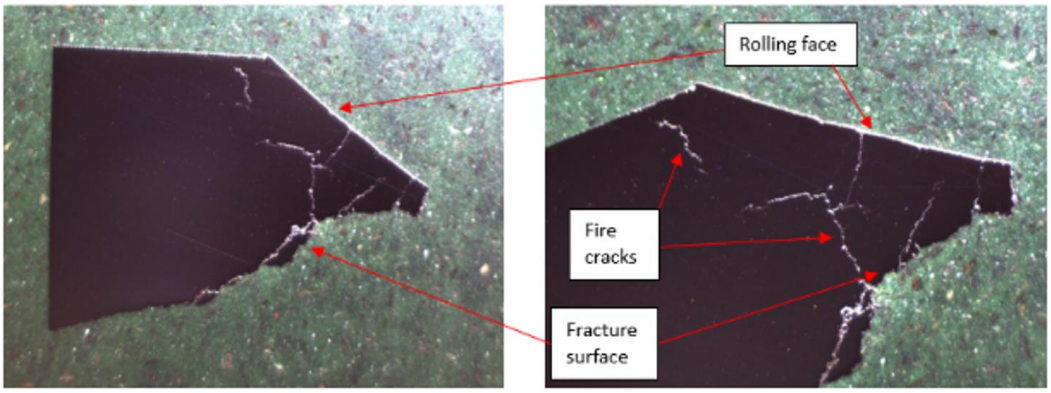

Fig. 5. *OM observation points*

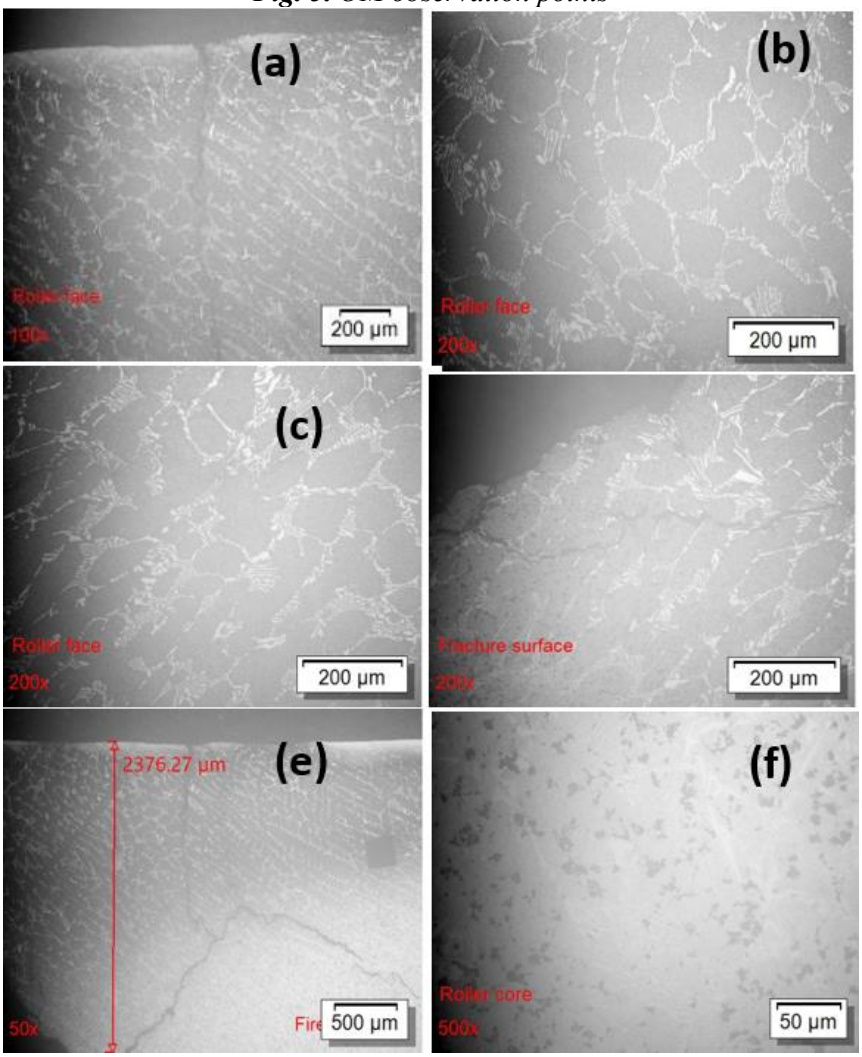

Fig. 6. *OM microstructures, (a) Roller face Micro-image, (b) Fire cracks can be seen, (c) Roller face region, (d) Micro-image, Depth of fire crack > 2.376 mm*

THE ANNALS OF "DUNAREA DE JOS" UNIVERSITY OF GALATI
FASCICLE IX. METALLURGY AND MATERIALS SCIENCE
No. 2 - 2026, ISSN 2668-4748; e-ISSN 2668-4756
Article DOI: https://doi.org/10.35219/mms.2026.2.05

Micro-examination (Figures 5 and 6), conducted according to ASTM E407 and the ASM Handbook Volume 9, follows industry best practices for metallurgical analysis. The process ensures accurate and repeatable results for material characterization, quality control, and failure investigation.

The sample was hot-mounted with phenolic resin. After proper grinding and polishing, the sample was subjected to inclusion analysis using optical microscopy. Inclusions were evaluated using micrographic analysis according to the ASTM E45 standard. The inclusion rating was performed under a light microscope with a 100x objective. After inclusion analysis, the sample was etched with 2% nital. The etched sample was examined to check for the presence of a decarburized layer or to determine if any case hardening had been applied to the component.

The sample was found to have higher sulphide inclusions on the order of 2.0 (thin series). It was fairly clean and free from any harmful inclusions / exogenous entrapment. No surface hardening was found to have been given to the part. The hardness and microstructures were homogeneous throughout the sample. Because surface hardening gives better fatigue life. Metallographic examination revealed a homogeneous microstructure throughout the roller guide cross-section. There was no indication of surface hardening treatments such as induction or flame hardening. The uniform hardness profile suggests the part was likely used in a normalized or cold-drawn condition. Surface hardening techniques are known to significantly improve fatigue life, especially in components subjected to cyclic or torsional stresses like roller guides.

Inclusion Analysis ASTM E45, Method A: ASTM E45 is a standard test method for determining the inclusion content in steel using microscopic examination. It is primarily used in quality control and material certification to ensure the steel meets required cleanliness standards.

ASTM E45 categorizes inclusions into the following main types: 1. Type A (Sulfide Inclusions) – Usually manganese sulfides (MnS), elongated due to rolling. 2. Type B (Aluminate Inclusions) – Alumina (Al_2O_3) inclusions, typically globular. 3. Type C (Silicate Inclusions) – Elongated silicates, formed from deoxidation.

Material Cleanliness: The sample was found to be fairly clean, with no evidence of harmful non-metallic inclusions or exogenous entrapments that could contribute to premature failure. This indicates proper steelmaking practices and material quality.

3.6. Scanning electron microscopy (SEM)

Scanning electron microscopy (SEM) and energy dispersive X-ray spectroscopy (EDS) were carried out on the cross-sectional fractured surface of the sample to observe the surface morphology and identify the elements present on the surface.

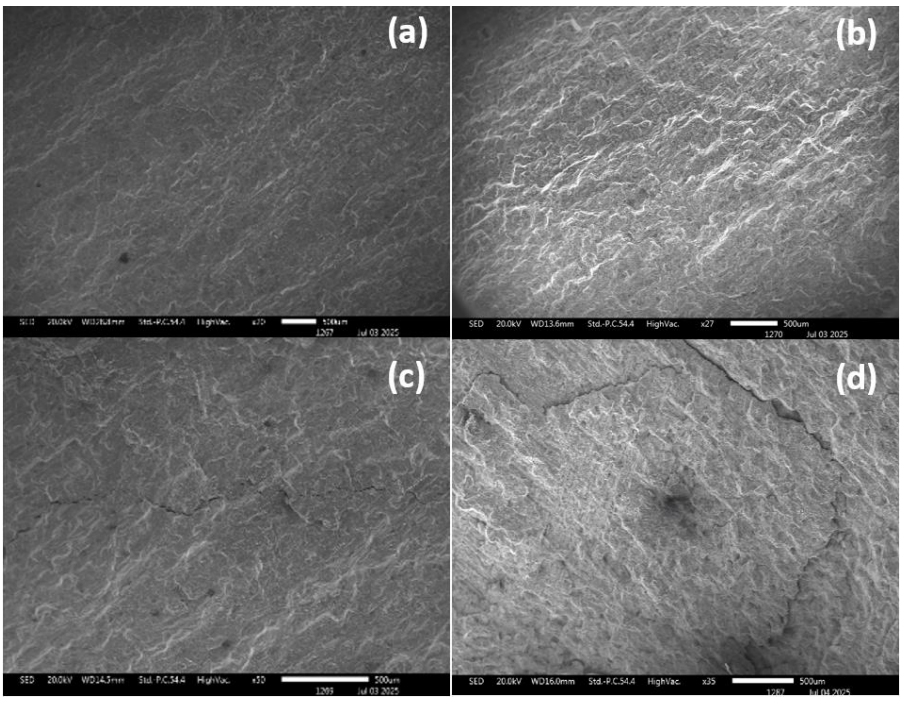

Fig. 7. *SEM micrographs, (a and b) beach marks crack propagation, (c) secondary cracks, (d) fatigue crack initiation*

THE ANNALS OF "DUNAREA DE JOS" UNIVERSITY OF GALATI
FASCICLE IX. METALLURGY AND MATERIALS SCIENCE
No. 2 - 2026, ISSN 2668-4748; e-ISSN 2668-4756
Article DOI: https://doi.org/10.35219/mms.2026.2.05

A typical intergranular fractured surface was revealed throughout the sample (Figure 7). This fracture surface displays a characteristic intergranular fracture mode, meaning the cracks propagated along grain boundaries rather than through the grains themselves. The distinctive features visible are individual grains with well-defined boundaries, revealing how the fracture paths preferentially followed these boundaries.

Evident outlines of individual grains indicate that the separation occurred along grain boundaries, suggesting grain boundary weakness. The sharp edges suggest that minimal deformation occurred during the fracture, which is consistent with a brittle fracture mode.

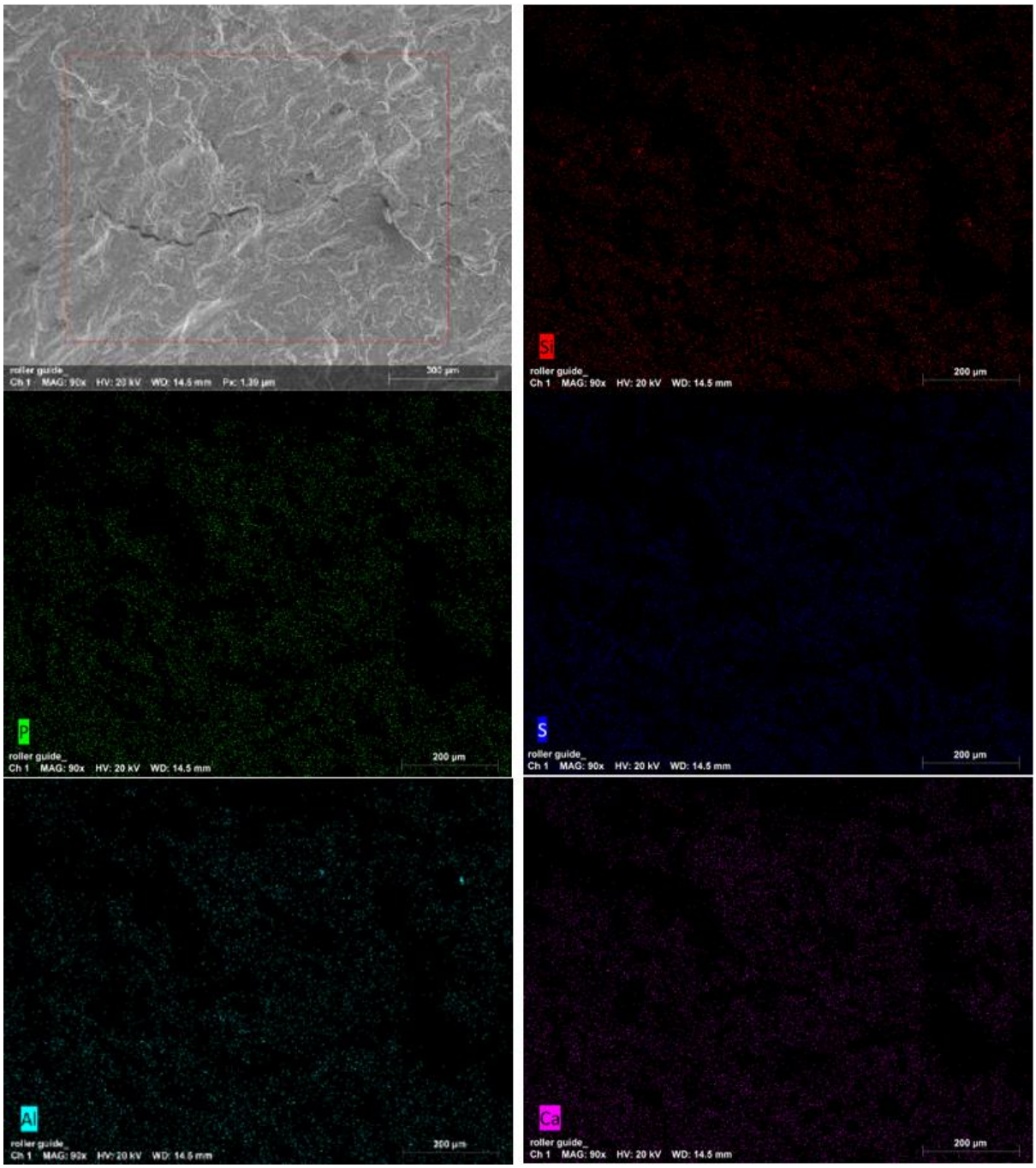

THE ANNALS OF "DUNAREA DE JOS" UNIVERSITY OF GALATI
FASCICLE IX. METALLURGY AND MATERIALS SCIENCE
No. 2 - 2026, ISSN 2668-4748; e-ISSN 2668-4756
Article DOI: https://doi.org/10.35219/mms.2026.2.05

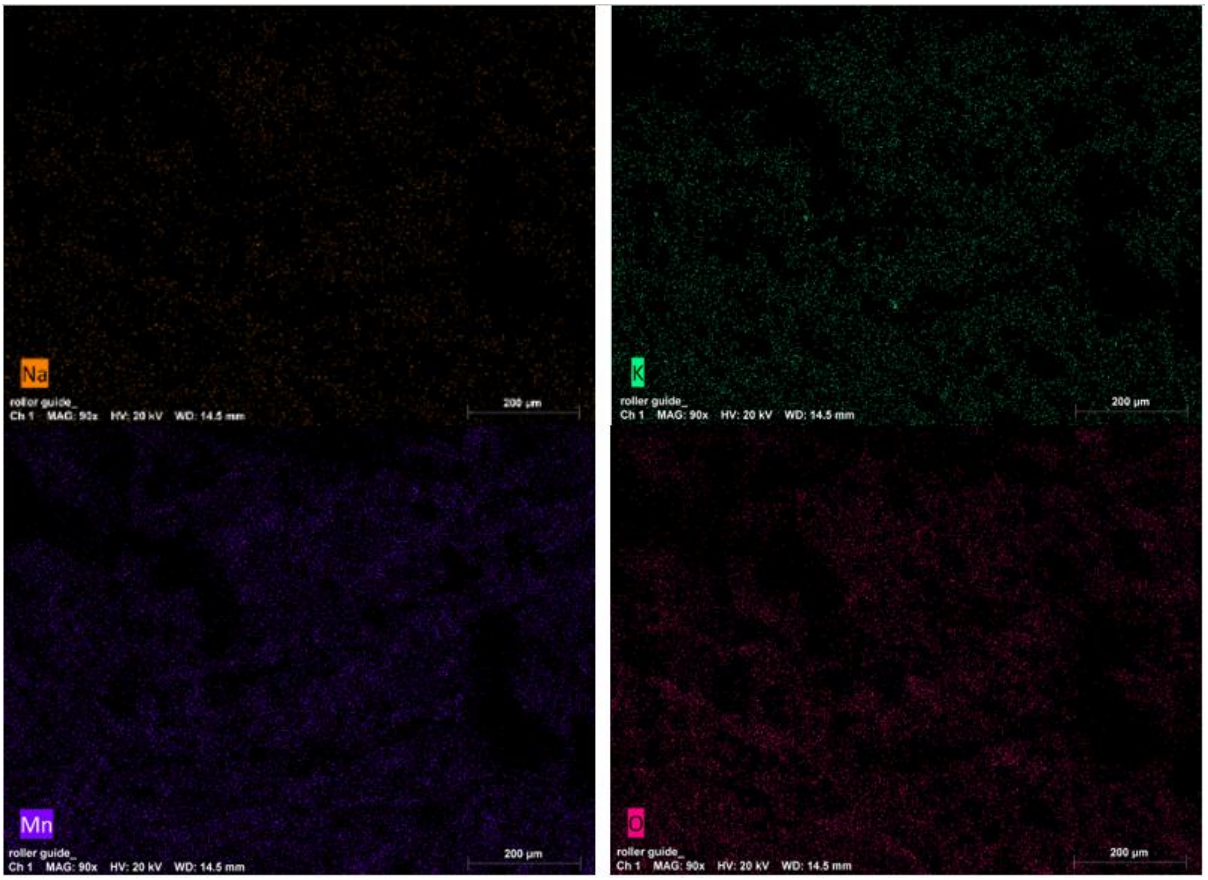

Fig. 8. *EDS mapping of the chemical element distribution*

3.7. Energy dispersive X-ray spectroscopy (EDS)

As suggested by the arrangement of the elemental distribution on the EDS map (Figure 8), the intergranular fracture surface reveals a homogeneous dispersion of alloying elements.

4. Conclusions

In summary, the comprehensive analysis of the roller guide failure sample has provided substantial insights into the mechanisms underlying its failure, pointing toward a fracture produced by fire cracks on the rolling face of the guide rolls. Thermally induced surface cracks are typically caused by rapid and repeated heating and cooling cycles during rolling operations, leading to localized thermal fatigue.

The guide rolls, which are in direct contact with high-temperature steel, are typically well protected from fire cracks and thermal fatigue through a combination of material selection, design features, surface treatments, and operational controls. These factors ensure roll life durability, minimize downtime, and prevent catastrophic roll failure in the rolling line process.

ASTM A 681-D2 Tool Steel is a high-carbon, high-chromium tool steel alloyed with molybdenum and vanadium as per the ASTM A 681 standard. It is the most widely used steel among the group D steels due to its abrasive wear resistance, high compressive strength, good through-hardening properties, high stability during hardening and good resistance to tempering. In the same standard ASTM A 681 – D3 grade is defined with a similar chemistry pattern; however, the key difference is the absence of Molybdenum and Vanadium. These 2 elements make a significant difference when using rolls in repeated heating and cooling cycles during rolling operations.

We conclude that the root cause of the failure is identified as the use of an inadequate steel grade for manufacturing the guide rolls operating under repetitive heating and cooling cycles. As a result, the guide rolls experienced pronounced fire cracking, which progressively developed into thermal fatigue damage, ultimately leading to catastrophic failure and a high disruption of the rolling process.

THE ANNALS OF "DUNAREA DE JOS" UNIVERSITY OF GALATI
FASCICLE IX. METALLURGY AND MATERIALS SCIENCE
No. 2 - 2026, ISSN 2668-4748; e-ISSN 2668-4756
Article DOI: https://doi.org/10.35219/mms.2026.2.05

References

[1]. ***, *Analysis and solutions to common failure causes of rolling guides in high speed wire rod finishing mills*, LMM Rolling Mill, 2024.
[2]. ***, *Analysis of common failure causes and solutions for rolling guides*, LMM Group, 2022.
[3]. ***, *Failure Analysis and Solutions of Rolling Mill Gearbox Bearings in Special Steel High Speed Wire Rod Mill*, ZHY Gear, 2025.
[4]. Pandey J. C., *Failure of Tungsten Carbide Rolls from a Wire and Rod Mill*, J. Fail. Anal. Prev., 2007.
[5]. Farrugia D., *Investigations into Roll Thermal Fatigue in Hot Rolling*, Int. J. Mater. Form, 2008.
[6]. ***, *ASTM A681 24: Standard Specification for Tool Steels Alloy*, ASTM International, 2024.
[7]. ***, *AISI D2 vs D3 Cold Work Tool Steel – ASTM A681*, Otai Special Steel, 2026.
[8]. ***, *A681 Type D3 (UNS T30403)*, H2ABC Materials DB, 2024.
[9]. Ghio E., *Effects of Multiple Quenching Treatments on O2, D2, and D3 Tool Steels*, JMMP, 2025.
[10]. Dadou A., *15 Minutes Heat Treatment Effect on AISI D3 Tool Steel*, J. Mater. Eng. Perf, 2026.
[11]. Reddy S., *Sliding Wear Analysis of Thermal Sprayed Mo Coating on D2 Steel*, JAER, 2023.
[12]. Mourad A.-H. I., *Fatigue Life and Crack Growth Prediction of Metallic Structures: A Review*, Structures, 2025.
[13]. Fayed A. S., *Fatigue Crack Growth Correlations under Mixed Mode Loading: A Review*, 2025.
[14]. ***, *Guide – Roller guide design considerations*, HKT International, 2025.
[15]. Arun K., *Lubricant Failure Analysis of Roll Neck Bearings of Wire Rod Mill*, IJAERS, 2025.
[16]. Okumoto T., *Study on Fire Cracks of Slabbing Mill Rolls*, ISIJ Overseas, 1980s reprint.
[17]. ***, *ASTM A681 Tool Steels Alloy (D series classification)*, Fushun Special Steel, 2015.
[18]. ***, *D3 Tool Steel: Properties and Applications*, SteelPro Group, 2024.
[19]. ***, *D2 vs D3 vs A2 Tool Steels – Comparative Metallurgy*, AoboSteel, 2025.
[20]. ***, *Tool Steel Resource Guide (A2, D2, H13…)*, KeyMetals, 2025.
[21]. Gurau L., *Failure Case Study Series Part One: Analysis of Oxygen Compressor Shaft Breakage*, The Annals of "Dunarea de Jos" University of Galati. Fascicle IX, Metallurgy and Materials Science, vol. 49, no. 1, p. 11-18, 2026.

THE ANNALS OF "DUNAREA DE JOS" UNIVERSITY OF GALATI
FASCICLE IX. METALLURGY AND MATERIALS SCIENCE
No. 2 - 2026, ISSN 2668-4748; e-ISSN 2668-4756
Article DOI: https://doi.org/10.35219/mms.2026.2.06

FAILURE CASE STUDY SERIES PART THREE: INVESTIGATION OF WEAR AND FAILURE MECHANISMS IN HEAVY-DUTY GEAR COUPLING

Liviu GURĂU, Florin MARIN, Mihaela MARIN, Cristian ȘTEFĂNESCU, Gheorghe GURĂU*

Interdisciplinary Research Centre in the Field of Eco-Nano Technology and Advanced Materials CC-ITI, Faculty of Engineering, "Dunarea de Jos" University of Galati, 47 Domneasca Street, 800008 Galati, Romania
e-mail: gheorghe.gurau@ugal.ro

ABSTRACT

This paper investigates the failure mechanisms of the gear teeth in a heavy-duty coupling, emphasizing the combined effects of mechanical loading, metallurgical microstructure, and tribological wear mechanisms.

Detailed characterization using optical microscopy (OM), scanning electron microscopy (SEM), energy-dispersive X-ray spectroscopy (EDS), and both chemical and mechanical testing identified pronounced wear and progressive degradation of the coupling sleeve, largely driven by operational misalignments and external contamination, such as mill cobbles. The analysis underscores the critical importance of precise material compatibility, a controlled hardness differential, and manufacturing accuracy in mitigating localized stress concentrations and wear. The findings highlight that abnormal wear progression results from a complex interaction among load redistribution owing to misalignment, tribological deterioration, manufacturing tolerances, and dynamic rotor–coupling interactions. Recommendations focus on optimizing design parameters, manufacturing processes, and operational routines to enhance the reliability, durability, and safety of high-torque coupling systems in harsh industrial environments.

KEYWORDS: failure analysis, gear-coupling, OM, SEM, EDS

1. Introduction

This paper presents a comprehensive analysis of the failure mechanisms observed in the gear teeth of a coupling used within a rolling mill assembly. The coupling exhibited pronounced abnormal wear patterns and progressive tooth damage-phenomena closely associated with mill cobble contamination. Gear couplings are indispensable in high-torque transmission systems operating under strenuous conditions; where the mechanical integrity of the gear teeth determines overall system reliability and safety. Deterioration phenomena such as wear, pitting, and crack initiation, compromise torque transfer efficiency; induce operational instability; and elevate the risk of unplanned downtime, or secondary damage to mill components [1, 2].

The investigation involved a visual assessment and advanced metallurgical examinations of the failed coupling components, emphasizing the interaction between material properties and operational stresses. The coupling configuration comprises hubs attached to the motor and gear shafts interconnected through internal sleeves. Typically, hubs are fabricated from high-strength alloy steels to resist fatigue and high-torque loads; conversely, sleeves are constructed from wear-resistant or case-hardened steels designed to withstand sliding contact, misalignment, and cyclic loading [3, 4].

A key factor influencing coupling life is the metallurgical relationship between the materials used for both the hub and the sleeve. An optimal hardness differential - ideally with the sleeve ideally slightly harder than the hub - ensures balanced wear and mitigates excessive tooth wear, pitting, or failure [5]. An imbalance where one component is significantly harder or softer accelerates localized wear and may lead to fatigue cracking at the tooth roots or edges [6]. Such relationships must be precisely engineered and monitored to optimize tribological compatibility.

From a geometric perspective, the contact of the straight internal teeth with the external teeth on the

THE ANNALS OF "DUNAREA DE JOS" UNIVERSITY OF GALATI
FASCICLE IX. METALLURGY AND MATERIALS SCIENCE
Nº. 2 - 2026, ISSN 2668-4748; e-ISSN 2668-4756
Article DOI: https://doi.org/10.35219/mms.2026.2.06

hub is designed to accommodate misalignment and facilitate sliding during operational angular displacement. While crowned or spherical external teeth have been employed in some coupling applications to improve contact conformity, the external gear teeth in this study are straight, with the design optimized for specific misalignment conditions. Even minor offsets can significantly influence meshing forces and contact patterns, as evidenced by finite element and analytical studies [7, 8]. These misalignments often lead to an uneven load sharing among the teeth, concentrating stresses toward the extremities of the gear teeth and thereby promoting fatigue and crack initiation at the root fillets [9].

Furthermore, manufacturing precision plays an essential role in load distribution during misaligned operation. Properly controlled manufacturing processes enhance interface conformity, reducing stress concentrations and prolonging gear service life [10, 11]. Deviations or inaccuracies in tooth geometry can accentuate load unevenness, thereby increasing wear and the likelihood of failure.

Tribological performance, particularly lubricant film stability, directly impacts wear progression. Under angular misalignment, contact migration toward tooth edges intensifies sliding and frictional heating, risking film collapse and surface wear [12, 13]. Lubricant selection, surface finish, and maintenance are critical in mitigating these effects. When a small number of teeth bear disproportionate loads due to misalignment, localized roughening, micropitting, and abrasion are amplified, decreasing the durability of the gear teeth [14].

The abnormal wear and progressive damage observed in the coupling teeth derive from a complex interaction of mechanical, metallurgical, geometric, and tribological factors. Addressing these issues requires an integrated approach encompassing precise manufacturing, proper material selection, lubrication management, and real-time operational monitoring. These measures are essential to ensure the longevity and safe operation of heavy-duty couplings in demanding industrial environments.

2. Experimental procedure

The failure investigation adhered to the protocol outlined in our previous study [15]. This involved determining the chemical composition of the components; examining the fracture morphology through stereomicroscopy; and performing an in-depth microstructural and surface-damage assessment using OM, SEM, and EDS techniques [15]. Furthermore, the mechanical behavior of the material was evaluated via hardness measurements.

The investigations were conducted on both the hub and sleeve of the gear coupling (Figure 1).

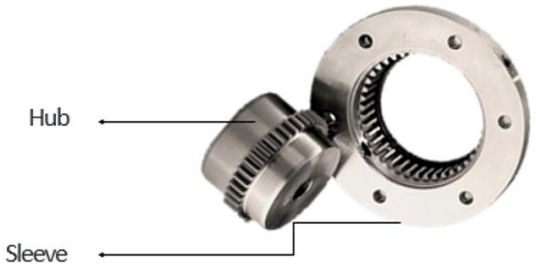

Fig. 1. *Gear coupling*

The recommended materials for this coupling are presented in Table 1.

Table 1. *ASTM equivalents of the recommended steel grades*

Steel Type	Grade	ASTM Grades	Key Properties	Typical Applications
Chromium-Molybdenum Alloy	AISI 4140	ASTM A29 Grade 4140 (for forgings), ASTM A322 / A322M (bars)	High strength, toughness, good hardenability, suitable for heat treatment	Medium to heavy-duty mechanical components, gear couplers, shafts, and gears
Nickel-Chromium-Molybdenum Alloy	AISI 4340	ASTM A29 Grade 4340	Very high toughness, excellent fatigue resistance, high hardenability	Heavy-duty gear couplings, high-load shafts, critical mechanical parts
Medium Carbon	AISI 1045 / 1050	ASTM A36 / AISI 1045	Moderate strength and hardness; can be surface-hardened (carburized or induction hardened)	Light to medium-load couplers, shafts, general mechanical components

THE ANNALS OF "DUNAREA DE JOS" UNIVERSITY OF GALATI
FASCICLE IX. METALLURGY AND MATERIALS SCIENCE
No. 2 - 2026, ISSN 2668-4748; e-ISSN 2668-4756
Article DOI: https://doi.org/10.35219/mms.2026.2.06

3. Results and discussion

3.1. Chemical composition

Samples were taken separately from the sleeve and the hub for spectral analysis to determine their material composition. The results of the analysis are presented in Table 2. This examination helps verify whether the materials meet the required specifications and identifies any anomalies that could have contributed to the failure. Understanding the chemical composition is crucial for assessing material properties and suitability for the application.

Using spark atomic emission spectrometry [15], we detected the chemical composition for both components as presented in Table 2.

Table 2. *Chemical composition*

Element	Sample A- Hub	Sample B- Sleeve
Carbon (C)	0.558	0.411
Silicon (Si)	0.224	0.306
Manganese (Mn)	0.645	0.664
Phosphorus (P)	0.012	0.009
Sulfur (S)	0.014	0.0025
Nitrogen (N)	0.0082	0.007
Chromium (Cr)	0.07	0.051
Molybdenum (Mo)	0.008	0.003
Nickel (Ni)	0.031	0.029
Calcium (Ca)	0.0013	0.0028
Aluminum (Al)	0.0162	0.025
Vanadium (V)	0.0014	0.0016
Titanium (Ti)	0.0009	0.0014
Copper (Cu)	0.048	0.046
Niobium (Nb)	0.0006	0.0011
Borom (B)	0.0002	0.00015
Iron (Fe)	98.356	98.433
CEV	0.6863	0.5375

We found that for this chemical composition, medium-carbon grades equivalent to AISI 1055 (C55 EN 10277-2-2008) for the hub and AISI 1040 (C40 (1.0511): EN 10277-2-2008) for the sleeve were used. Consequently, we observe a very large hardness/strength mismatch (Table 3) between the hub (C55) and the sleeve (C40). This mismatch could drive accelerated wear during normal torque transmission. Even if the design intent is to use the sleeve as a sacrificial element, the actual hardness gap is too high, which led to rapid wear and a rapid catastrophic failure when torque and misalignment increased (the design aspects of the sacrificial sleeve concept need to be correlated with these results).

A practical pairing recommendation in the case of a sacrificial sleeve concept (controlled) is: Hub: ~300–340 HB; Sleeve: ~270–310 HB (≈ –15–30 HB vs. hub), with strict lubrication control and inspection intervals.

Table 3. *HB [MPa] for both C40 EN 10277-2-2008 (sleeve) and C55 EN 10277-2-2008 (hub)*

A) As-rolled / As-forged (no heat treatment):		B) Quenched & Tempered:	
C40	170–205 HB	**C40**	180–220 HB (soft temper) up to 35–45 HRC
C55	190–235 HB	**C55**	200–260 HB (soft temper) up to 50–56 HRC

THE ANNALS OF "DUNAREA DE JOS" UNIVERSITY OF GALATI
FASCICLE IX. METALLURGY AND MATERIALS SCIENCE
Nº. 2 - 2026, ISSN 2668-4748; e-ISSN 2668-4756
Article DOI: https://doi.org/10.35219/mms.2026.2.06

3.2. Hardness test

The test method used for the gear sample pieces analysed (Figure 2) was Vickers Hardness (HV30) – ASTM E92 standard. The values were converted to HB (Brinnel) and HRB (Rockwell) as well. The evaluation was conducted on the tooth-tip region as well as the core regions of both the hub and sleeve samples. The purpose was to confirm whether similar materials are used for the hub and sleeves and to identify hardness differences, if any.

Sample A (Hub) exhibits slightly higher hardness values at both the tooth tip (233 HV30) and core (234 HV30) compared to Sample B (Sleeve), which shows hardness values of 212 HV30 at the tooth tip and 220 HV30 at the core. This indicates that the hub material is marginally harder than the sleeve, which is consistent with its higher carbon content (Figure 3).

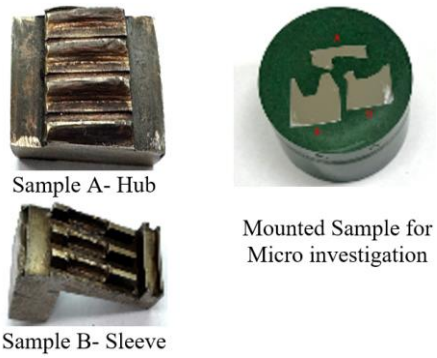

Fig. 2. *Samples for hardness investigation (A) hub (B) sleeve*

The lower hardness in the sleeve suggests it has comparatively less wear resistance, which likely contributed to the severe abrasive wear and tooth failure observed in the sleeve. Additionally, the small hardness difference between the tooth tip and core in the sleeve indicates a lack of surface hardening, making the teeth more vulnerable to wear under high contact stresses.

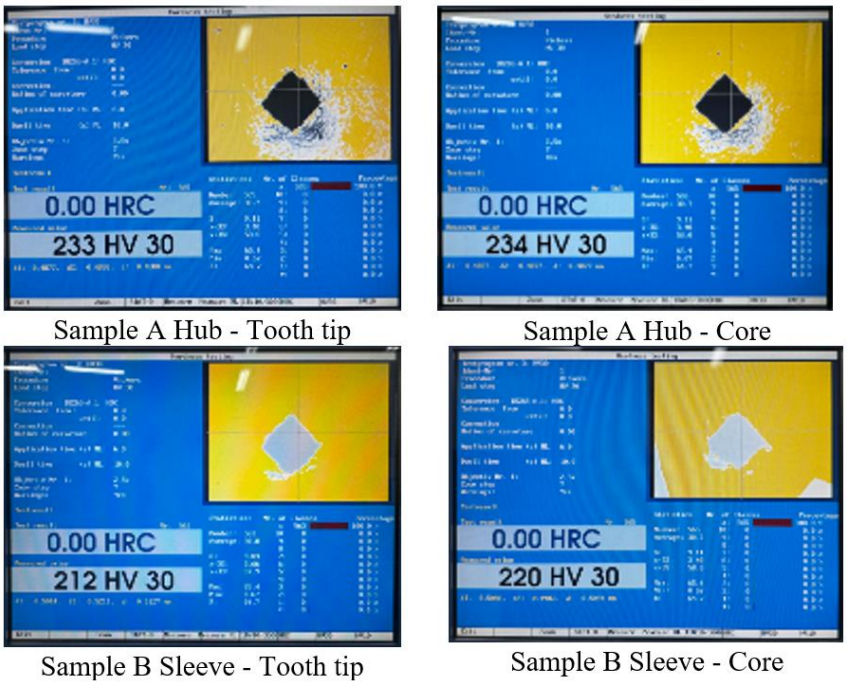

Fig. 3. *Vickers hardness for hub and sleeve*

3.3. Optical microscopy

As stated previously [15], the cross-sectional sample was polished up to 1500-grit emery grade, followed by 1 μm velvet cloth polishing, and then etched using a 2% nital solution to reveal microstructures and observe defects. Micro-examination was carried out as per ASTM E407 and the ASM Handbook, Volume 9.

THE ANNALS OF "DUNAREA DE JOS" UNIVERSITY OF GALATI
FASCICLE IX. METALLURGY AND MATERIALS SCIENCE
Nº. 2 - 2026, ISSN 2668-4748; e-ISSN 2668-4756
Article DOI: https://doi.org/10.35219/mms.2026.2.06

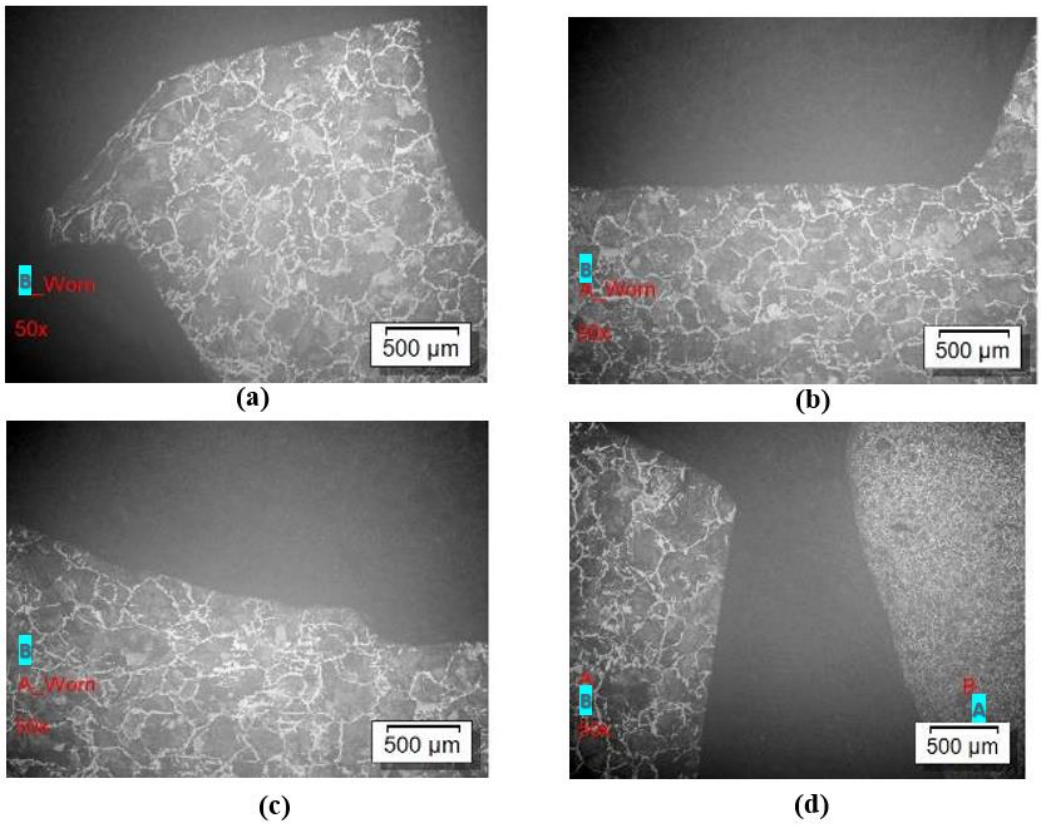

Fig. 4. *OM microstructures: (a) Sleeve sample: Tooth tip regions did not reveal any hard microstructure, indicating no case hardening was applied; (b) Sleeve sample: Tooth-damage region showing a normal ferrite-pearlitic microstructure; (c) Sleeve sample: Tooth-damage region showing a normal ferrite-pearlitic microstructure; (d) Both samples' microstructure are ferrito-pearlitic. Hub Sample (A) shows significantly finer structure*

Both the hub (Sample A) and sleeve (Sample B) show ferrite–pearlite microstructures, indicating that both components were produced from plain carbon steel or similar low-alloy steel. The hub sample exhibited a significantly finer microstructure compared to that of the sleeve sample.

No evidence of case hardening was observed in either the tooth tips or tooth damage regions. Both samples exhibit microstructures consistent with non–surface-hardened steels.

3.4. Scanning electron microscopy (SEM) and energy-dispersive X-ray spectroscopy (EDS)

For this study, a JEOL IT 300LV scanning electron microscope equipped with a Bruker energy dispersive X ray spectroscopy (EDS) detector was utilized.

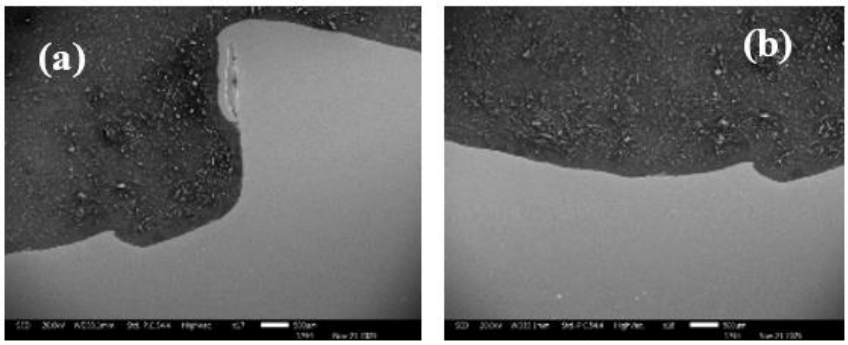

THE ANNALS OF "DUNAREA DE JOS" UNIVERSITY OF GALATI
FASCICLE IX. METALLURGY AND MATERIALS SCIENCE
No. 2 - 2026, ISSN 2668-4748; e-ISSN 2668-4756
Article DOI: https://doi.org/10.35219/mms.2026.2.06

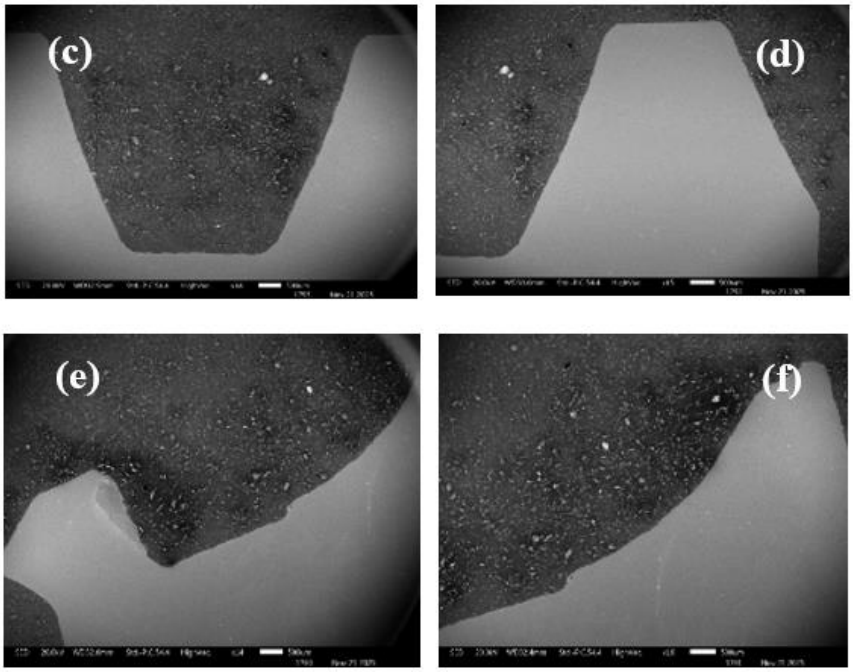

Fig. 5. *SEM micrographs; (a) Hub -A Tooth region; (b) Hub-A worn out region; (c) Sleeve B tooth region; (d, e, f) Sleeve-B worn region*

No material-related abnormalities were observed in the SEM (Figure 5) examination of either the hub or the sleeve. The worn regions showed no inclusions, defects, or compositional anomalies, confirming that the material quality did not contribute to the observed damage.

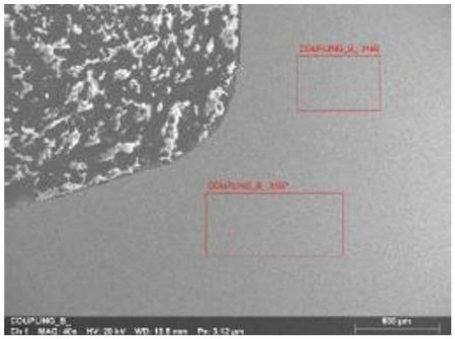

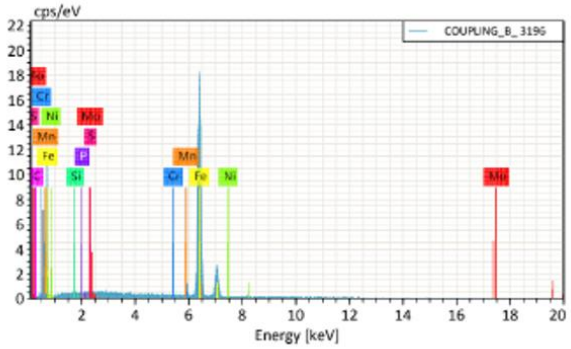

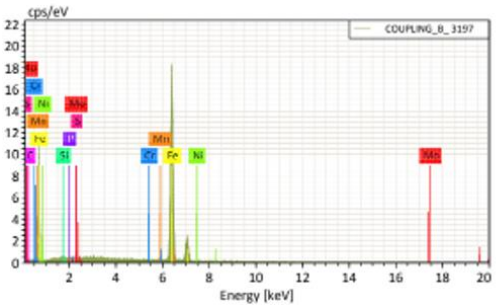

EDS analysis

Spectrum	C	Si	P	S	Cr	Mn	Fe	Ni	Mo
COUPLING_B_ 3196	4.33	0.14	0.02	0.00	0.05	0.41	94.63	0.22	0.20
COUPLING_B_ 3197	3.61	0.30	0.01	0.00	0.00	0.42	95.65	0.00	0.01

THE ANNALS OF "DUNAREA DE JOS" UNIVERSITY OF GALATI
FASCICLE IX. METALLURGY AND MATERIALS SCIENCE
Nº. 2 - 2026, ISSN 2668-4748; e-ISSN 2668-4756
Article DOI: https://doi.org/10.35219/mms.2026.2.06

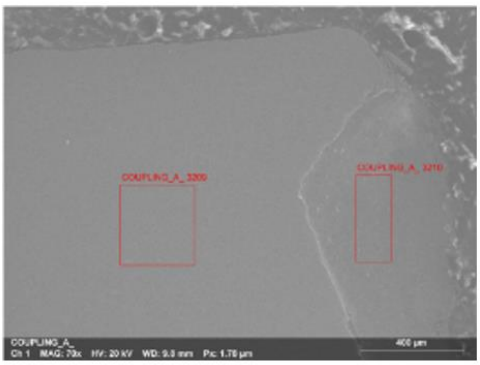

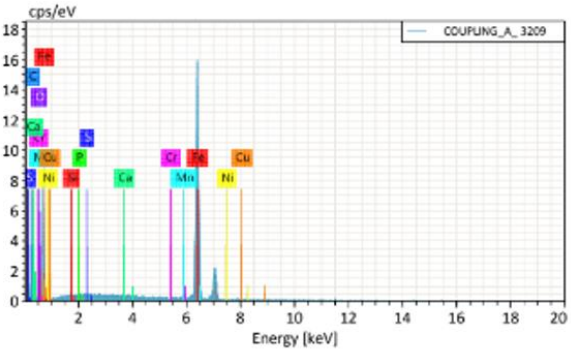

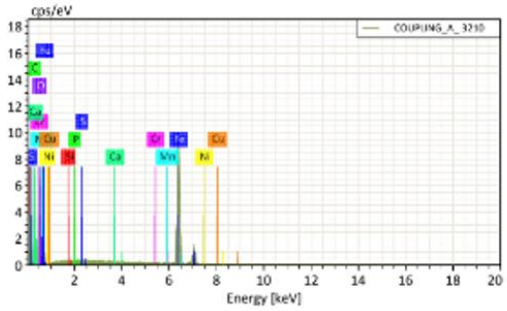

EDS analysis

Spectrum	C	O	Si	P	S	Ca	Cr	Mn	Fe	Ni	Cu
COUPLING_A_3209	3.61	0.00	0.29	0.00	0.00	0.00	0.09	0.65	95.32	0.00	0.03
COUPLING_A_3210	14.01	23.39	0.10	0.10	0.28	0.00	0.08	0.33	61.57	0.09	0.05

Fig. 6. *EDS spectra on both sleeve and hub tooth*

The EDS results closely match the measured chemical composition, confirming that the material was manufactured according to standard conditions and did not play a significant role in the coupler's failure.

4. Conclusions

The thorough investigation into the failure of the hub and sleeve gear coupler, including visual inspection, hardness testing, chemical analysis, metallography, and SEM/EDS, provides insight into the mechanisms responsible for the sleeve tooth damage. All findings consistently indicate that the failure was driven by rapid, progressive abrasive wear, resulting from an excessive difference in hardness and strength between the hub and the sleeve. Importantly, no material-related abnormalities or microstructural defects were identified in either component.

Physical and microscopic examinations showed that the sleeve tooth wear was concentrated over approximately half of the available tooth width, demonstrating uneven load distribution during operation. The reduced load-bearing contact area accelerated tooth profile degradation under service conditions.

Chemical composition analysis confirmed that both the hub and sleeve were manufactured from basic-medium carbon steels with an excessive difference between the grades. The sleeve exhibited lower carbon content without alloying elements compared to the hub. This difference resulted in lower achievable hardness and reduced wear resistance for the sleeve material.

Hardness measurements confirmed low and uniform bulk hardness across both the hub and sleeve teeth, with no hardness gradient and no indication of carburizing or induction hardening. This lack of surface hardening severely limited wear resistance under high-torque, cyclic loading.

Metallography revealed normal ferrite–pearlite microstructures throughout all examined regions. However, the hub sample exhibited a significantly finer microstructure compared to the sleeve. This observation is in line with the damage found in the sleeve. No evidence of case hardening, abnormal transformation products, cracking, or other microstructural abnormalities was observed. SEM/EDS analysis further confirmed the absence of inclusions, defects, or compositional anomalies in the worn regions.

We conclude that the root cause of the failure can be conclusively attributed to the combined influence of the hub–sleeve chemistry disparity (lower-carbon sleeve), the associated reduction in sleeve hardness, and an uneven tooth-width load distribution. These factors acted synergistically to

accelerate wear and precipitate premature failure under service torque. Metallurgical evidence also confirms that the absence of required surface hardening and the inherently softer, lower-carbon sleeve material led to progressive abrasive wear, tooth profile loss, and the final functional failure of the gear coupling.

References

[1]. Lin Z., *et al.*, *Dynamic characteristics of the gear coupled rotor system with both bearing defect and coupling misalignment*, Nonlinear Dynamics, 113, p. 25683-25713, 2025.
[2]. Miao X., *et al.*, *Dynamic characteristics of rotor system with parallel and angular misaligned involute spline coupling*, Meccanica, 59, p. 1061-1085, 2024.
[3]. Wang J., *et al.*, *An accurate finite element model for tooth contact and meshing force distribution of crown gear coupling*, Journal of Mechanical Science and Technology, 39(5), p. 2767-2778, 2025.
[4]. Zhang C., *et al.*, *An improved dynamic model of the spline coupling with misalignment and its load distribution analysis*, International Journal of Mechanics and Materials in Design, 20, p. 393-408, 2024.
[5]. Jangra D., *et al.*, *Gear sliding wear: The role of radial, axial, and combined misalignment*, Journal of Mechanical Science and Technology, 39, p. 5375-5383, 2025.
[6]. Zhao Y., *et al.*, *A lubrication contact pair model for simulating gear micro pitting damage characteristics based on contour integral*, Advances in Mechanical Engineering, 13(8), p. 1-9, 2021.
[7]. Li Z., *et al.*, *Nonlinear dynamics of unsymmetrical rotor bearing system with fault of parallel misalignment*, Advances in Mechanical Engineering, 10(5), p. 1-17, 2018.
[8]. Wang J., *et al.*, *Finite element analysis of gear tooth root crack under misalignment*, The Journal of Engineering, (In press), https://doi.org/10.1049/joe.2018.9209, 2025.
[9]. Iñurritegui A., *et al.*, *Spherical gear coupling design space analysis for high misalignment applications*, Mechanism and Machine Theory, 173, 104837, 2022.
[10]. Guan Y., *et al.*, *Clearance distribution and contact characteristics considering hob feed path in misaligned gear couplings*, Scientific Reports, 15, p. 1-16, 2025.
[11]. de Bechillon N. G., *et al.*, *A new experimental methodology to assess gear scuffing initiation*, Tribology-Materials, Surfaces & Interfaces, 16(3), p. 245-255, 2022.
[12]. Jangra D., *et al.*, *Gear sliding wear: The role of radial, axial, and combined misalignment*, Journal of Mechanical Science and Technology, 39, p. 5375-5383, 2025.
[13]. Olson R., *et al.*, *Case study of ISO/TS 6336 22 micropitting calculations*, Proceedings of the NREL/CP 5000 77731, 2020.
[14]. McCormick M., *Scuffing. Gear Solutions Magazine*, Retrieved from https://gearsolutions.com, 2016.
[15]. Gurau L., *Failure Case Study Series Part One: Analysis of Oxygen Compressor Shaft Breakage*, The Annals of "Dunarea de Jos" University of Galati. Fascicle IX, Metallurgy and Materials Science, vol. 49, no. 1, p. 11-18, 2026.

THE ANNALS OF "DUNAREA DE JOS" UNIVERSITY OF GALATI
FASCICLE IX. METALLURGY AND MATERIALS SCIENCE
No. 2 - 2026, ISSN 2668-4748; e-ISSN 2668-4756
Article DOI: https://doi.org/10.35219/mms.2026.2.07

FAILURE CASE STUDY SERIES PART FOUR: INVESTIGATION OF THE FAILURE MECHANISM OF THE CONNECTING ROD IN AN INDUSTRIAL OXYGEN COMPRESSOR

Liviu GURĂU, Florin MARIN, Mihaela MARIN, Cristian ȘTEFĂNESCU, Gheorghe GURĂU*

Interdisciplinary Research Centre in the Field of Eco-Nano Technology and Advanced Materials CC-ITI, Faculty of Engineering, "Dunarea de Jos" University of Galati, 47 Domneasca Street, 800008 Galati, Romania
e-mail: gheorghe.gurau@ugal.ro

ABSTRACT

This investigation addresses the catastrophic fracture of a connecting rod in an oxygen compressor unit during steady-state operation. Owing to its function in transmitting cyclic compressive and tensile loads between the crankshaft and the piston, the connecting rod it's a critical structural element.

The assessment employed a systematic multi-technique protocol. Macroscopic fractography was used to document crack morphology, fracture-surface topography, and subsidiary failure-related surface markers. Representative specimens were preserved for laboratory evaluation. Material conformance was verified through chemical composition analysis and hardness measurements benchmarked against applicable standards. The internal structure, including phase distribution, cleanliness, inclusion content, and thermal-processing quality, was examined using optical metallography (OM). High-resolution scanning electron microscopy (SEM) combined with energy-dispersive spectroscopy (EDS) enabled the identification of crack-initiation sites, fracture mechanisms, and local compositional anomalies.

KEYWORDS: failure analysis, connecting rod, fractography, OM, SEM, EDS

1. Introduction

The connecting rod is a key structural element in an oxygen compressor responsible for transmitting mechanical energy from the shaft to the piston. It converts rotary motion into reciprocating motion, enabling the compression of oxygen gas. Typically constructed from high-strength materials such as forged or alloy steel, the connecting rod is designed to endure high cyclic stresses under continuous load conditions.

It endures complex thermomechanical loading conditions including alternating tensile–compressive stresses, bending effects, inertial forces, and fluctuating gas pressures. These factors collectively produce high stress amplitudes that accelerate fatigue damage evolution. Finite element investigations have demonstrated that geometric discontinuities—particularly insufficient fillet radii near the cap bolt region—significantly amplify local stress concentrations, thereby promoting early crack initiation [1]. Improvements in manufacturing and material processing have also been shown to enhance the safety factor with optimized forging and machining parameters yielding reductions in residual stress and improved fatigue resistance [2].

Comprehensive analyses of connecting rods [3] reveal that failures typically arise from interacting mechanisms such as buckling, fretting, multiaxial fatigue, and cavitation-induced degradation, emphasizing the inherently multiphysical nature of the problem. Metallurgical examinations of failed rods show that axial grooves and surface irregularities act as crack nucleation sites facilitating multi-origin fatigue propagation under fluctuating mechanical loads [4]. In diesel engine applications, improper bolt torque application has been identified as a critical factor leading to brittle fracture patterns and reduced rod life, highlighting the importance of accurate assembly conditions in reciprocating compressors as well [5].

The dynamic response of the system plays an important role in determining the structural reliability of the connecting rod. Modal analysis [6] shows that

THE ANNALS OF "DUNAREA DE JOS" UNIVERSITY OF GALATI
FASCICLE IX. METALLURGY AND MATERIALS SCIENCE
Nº. 2 - 2026, ISSN 2668-4748; e-ISSN 2668-4756
Article DOI: https://doi.org/10.35219/mms.2026.2.07

if the rod's natural frequencies fall within the machine's working frequency range resonance can occur producing higher vibration stresses and accelerating fatigue damage. Advanced fatigue assessment methodologies using variable amplitude engine speed history and finite element stress fields have greatly improved predictions of rod life, demonstrating a strong correlation between simulated and real-world operating conditions [7].

Fretting fatigue at the big-end bearing interface is another critical contributor to failure. High-fidelity simulations show that parameters such as bearing crush, bolt tightening torque, and local friction strongly affect contact pressure distribution and microslip behavior directly modifying fretting damage severity [8]. Lubrication issues further exacerbate this problem; insufficient oil film thickness increases hydrodynamic pressure, leading to bushing overload and failure even under nominal rod load conditions [9]. Material selection plays a decisive role in fatigue performance. Comparative investigations of composite and metallic connecting rods show that SiC-reinforced aluminium alloys can provide major reductions in structural mass while maintaining satisfactory fatigue strength, making them promising candidates for compressor applications where lower inertia is beneficial [10]. Similarly, design studies evaluating different cross-sectional geometries such as I-sections, H-sections, and circular profiles, indicate that optimized shapes substantially enhance buckling resistance and reduce von Mises stresses under cyclic loading [11]. Recent research also highlights the value of topology optimization which enables up to a 20% mass reduction while maintaining or enhancing structural stiffness and increasing low-order natural frequencies—thereby reducing the risk of resonance-related failures in oxygen compressor rods [12]. Meanwhile, metallurgical studies on fatigue-dominated fractures confirm that the microstructure - including ferrite pearlite morphology and surface finish quality - plays a defining role in crack growth behavior under service loading [13].

Published studies consistently show that connecting-rod failures arise from a combination of factors including design geometry, material characteristics, dynamic load effects, lubrication quality, and the precision of assembly. Effective design therefore requires an integrated approach combining fatigue modeling, metallurgical evaluation, optimized manufacturing routes, and dynamic system analysis.

This paper focuses on the unexpected breakage of a connecting rod in an oxygen compressor unit. The incident occurred during normal operation resulting in an unplanned system shutdown with potential implications for both operational safety and production continuity. Given its essential role and the nature of the failure, a thorough investigation has been undertaken to identify the root cause, evaluate contributing factors, and recommend corrective and preventive actions to avoid recurrence and improve equipment reliability.

2. Experimental procedure

The unexpected breakage of a connecting rod in the oxygen compressor (Figure 1) occurred during normal operation, resulting in an unplanned system shutdown with potential implications for both operational safety and production continuity.

The failure assessment was conducted in accordance with the methodology presented in our previous work [14]. The analysis began with a thorough macroscopic examination of the fractured component, during which crack morphology, surface discoloration, and wear-related anomalies were systematically characterized. This initial assessment further facilitated the detection of geometric and surface deviations, including misalignment, bending distortion, corrosion, and scoring, that may have influenced the failure process.

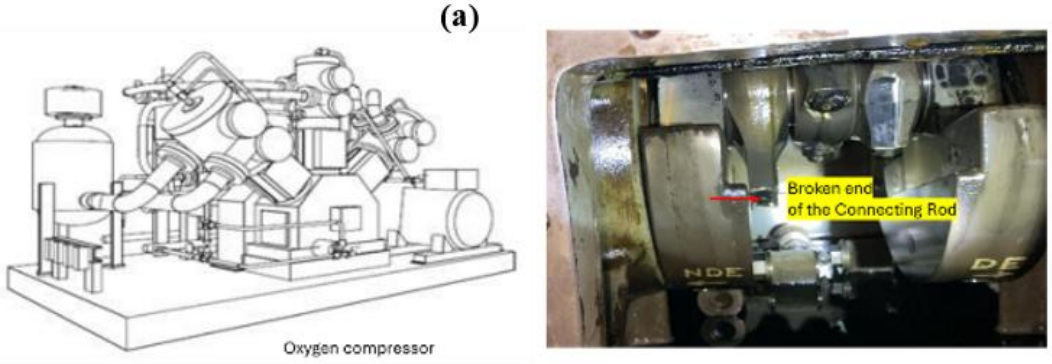

THE ANNALS OF "DUNAREA DE JOS" UNIVERSITY OF GALATI
FASCICLE IX. METALLURGY AND MATERIALS SCIENCE
N°. 2 - 2026, ISSN 2668-4748; e-ISSN 2668-4756
Article DOI: https://doi.org/10.35219/mms.2026.2.07

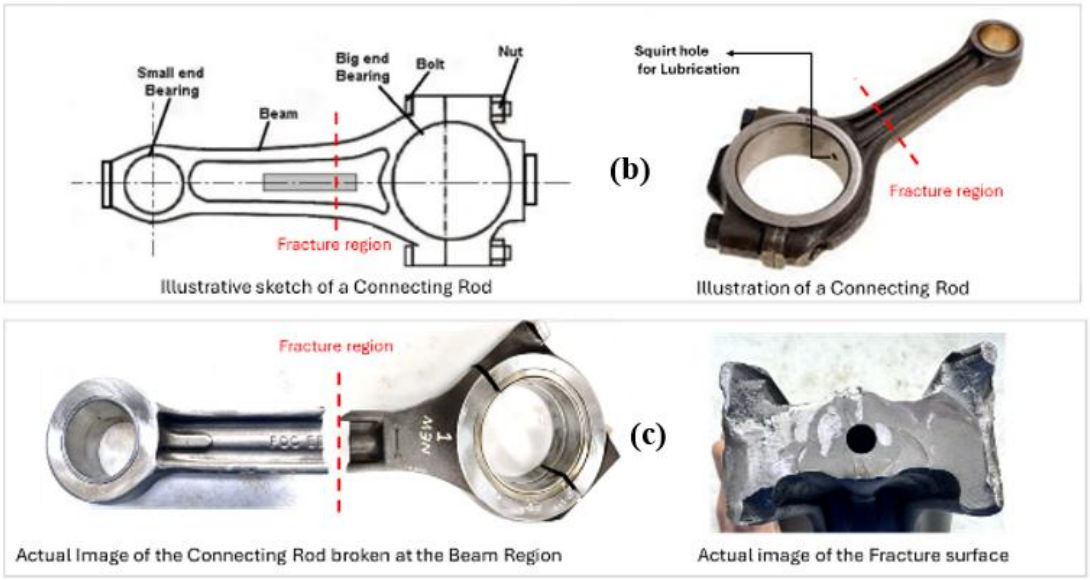

Fig. 1. *Oxygen compressor: assembly detail (a), connecting road (b), and fracture (c)*

Subsequently, representative specimens were carefully selected, catalogued, and preserved to maintain evidentiary integrity for the advanced analytical procedures that followed.

3. Results and discussion

3.1. Visual Inspection

A visual inspection of the fractured connecting rod was carried out under magnification to assess the nature of the fracture surfaces and to identify any features indicative of the failure mechanism.

One side of the connecting rod was observed to have a shiny, machined surface with visible machining marks or scratches, indicating that it had undergone secondary machining or grinding operations (Figure 2). This suggests the surface was modified post-forging, possibly for balancing or dimensional control.

Fig. 2. *Machining marks on one side*

Furthermore, a cross-sectional analysis of the connecting rod reveals a noticeable asymmetry in wall thickness on either side of the central oil hole: Side 1 thickness: 6.06 mm; Side 2 thickness: 7.59 mm (a difference of 1.53 mm). The asymmetric material distribution, highlighted by the digital vernier calliper readings (Figure 3), reveals a notable thickness difference on either side of the central oil hole.

THE ANNALS OF "DUNAREA DE JOS" UNIVERSITY OF GALATI
FASCICLE IX. METALLURGY AND MATERIALS SCIENCE
No. 2 - 2026, ISSN 2668-4748; e-ISSN 2668-4756
Article DOI: https://doi.org/10.35219/mms.2026.2.07

Fig. 3. *Asymmetric squirt hole*

This variation in a functionally critical region raises serious concerns regarding the manufacturing accuracy, geometric consistency, and structural reliability of the connecting rod. It may also indicate a lack of process control, tool wear, or inadequate calibration over time - issues that necessitate a thorough review of the production methods, tooling setup, and inspection procedures to ensure quality and consistency.

This thickness variation could stem from multiple manufacturing issues, including: Tool misalignment during drilling or machining operations, resulting in an off-centre oil hole or uneven material removal; Forging-die mismatch or inconsistent material flow, which can lead to asymmetrical shaping and wall thickness during the forging process; Core shift during casting or forging, causing the internal geometry to deviate from the intended design specification.

The presence of uneven wall thickness around the central hole can introduce areas of localized stress concentration under operational loading conditions. When subjected to cyclic stresses, these regions become likely initiation points for crack propagation, significantly increasing the risk of premature fatigue failure. Furthermore, such non-uniform geometry may disrupt oil flow characteristics, compromising lubrication effectiveness, accelerating component wear, and ultimately affecting the overall durability and performance of the connecting rod in service.

3.2. Fracture Surface Analysis

A fractographic analysis of the failed connecting rod was performed, focusing on the fracture surface characteristics observed around the central oil hole and corners of the broken end. The investigation highlights signs of fatigue crack initiation, progression, and final fracture, providing insight into the failure mechanism and likely origin.

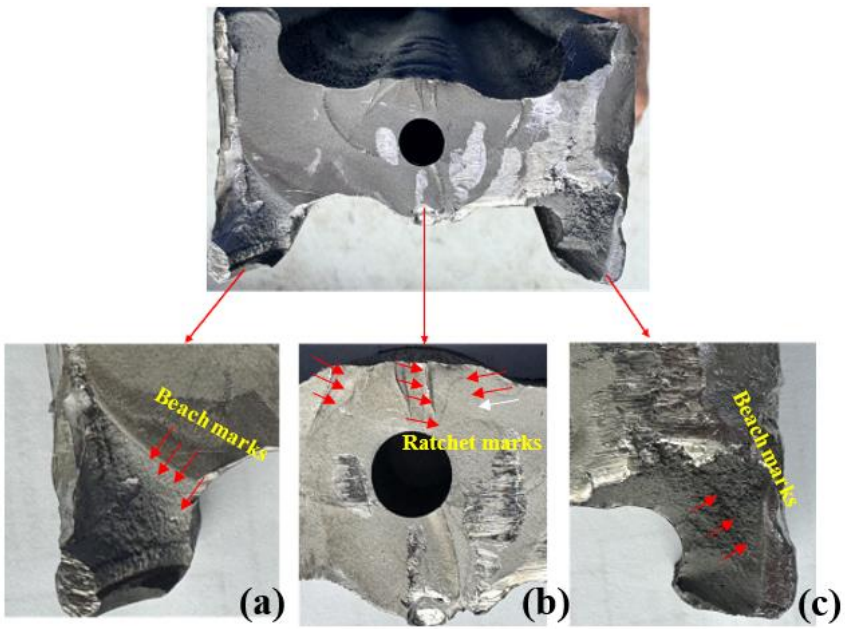

THE ANNALS OF "DUNAREA DE JOS" UNIVERSITY OF GALATI
FASCICLE IX. METALLURGY AND MATERIALS SCIENCE
Nº. 2 - 2026, ISSN 2668-4748; e-ISSN 2668-4756
Article DOI: https://doi.org/10.35219/mms.2026.2.07

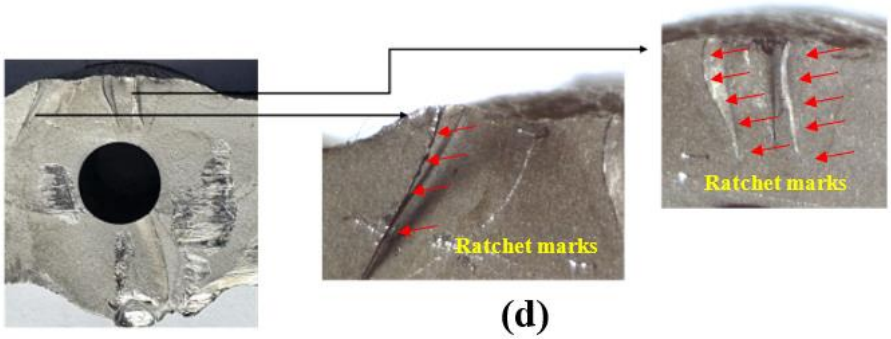

Fig. 4. *Surface fracture: (a) left side, central side (b), right side (c), and magnified view of the crack origin (d)*

Figure 4a shows a rough and uneven surface with evidence of ductile tearing, suggesting a final shear fracture. The fracture origin (Figure 4b) appears to be located in the thinner thickness region near the central oil hole, a region typically subject to high stress concentration during service. The observed ratchet marks are in line with the suspicion of a crack origin near the ratchet mark region. Figure 4 c points out the rough texture and uneven nature, suggesting a rapid final fracture after fatigue crack propagation. Minor surface irregularities hint at material discontinuities or localized stress risers.

The fracture surface shows evident signs of fatigue failure originating from the thinner edge of the central oil hole (Figure 4d), where high stress concentration likely existed. Ratchet marks indicate multiple crack initiation sites and progressive crack growth under cyclic loading. The final fracture zone appears rougher, suggesting sudden overload after prolonged fatigue. The presence of ratchet marks indicates the coalescence of cracks from different initiation points.

3.3. Chemical composition

Based on the chemical analysis performed per ASTM E415-21, the tested sample shows a composition closely aligning with the specifications of AISI 4140, a chromium-molybdenum low-alloy steel widely used for high-strength applications (Table 1). This is in line with the OEM material specification mentioned in the manual.

Key alloying elements such as chromium, molybdenum, and manganese are present within the expected ranges. Additionally, trace elements and impurities such as sulphur and phosphorus are within acceptable limits, indicating good material quality and compliance with relevant metallurgical standards. This suggests that the material used for the connecting rod adheres to the OEM's specification of 'forged steel'. The presence of balanced alloying elements ensures the necessary combination of strength, hardenability, and fatigue resistance required for high-stress applications. Overall, the chemical composition confirms the suitability of the selected material grade (AISI 4140) for the operational demands of the component.

The tested sample's chemistry and properties align with AISI 4140, making it well-suited for high-performance applications such as connecting rods, where cyclic loading, dimensional stability, and fatigue resistance are critical requirements.

Table 1. *Chemical composition*

Element	% Composition in Test sample	Nearest Grade AISI 4140
C	0.40%	0.38 -0.43%
Si	0.19%	0.15-0.35%
Mn	0.72%	0.75-1.00%
P	0.015%	
S	0.020%	
Cu	0.19%	
Ni	0.12%	
Cr	0.99%	0.80-1.10%
Mo	0.17%	0.15-0.25%
Ca	0.003%	
Al	0.014%	
V	0.003%	
Nb	0.002%	
N	0.0223%	
Fe	97.13%	

AISI 4140 offers a strong combination of strength, toughness, and wear resistance, especially when properly heat-treated, allowing it to perform reliably under demanding mechanical and thermal stresses. Its versatility in machinery and compatibility

THE ANNALS OF "DUNAREA DE JOS" UNIVERSITY OF GALATI
FASCICLE IX. METALLURGY AND MATERIALS SCIENCE
Nº. 2 - 2026, ISSN 2668-4748; e-ISSN 2668-4756
Article DOI: https://doi.org/10.35219/mms.2026.2.07

with various heat treatment processes make it a widely preferred material for both original manufacturing and aftermarket repair of precision-engineered components in automotive, aerospace, and industrial machinery sectors.

3.4. Hardness test

Hardness measurements (HV30) were performed using a KB150 R Universal Hardness Testing Machine applying a load of 294.543 N. Measurements were performed on both the surface and core regions near the fracture initiation site as shown in the mounted cross-sectional sample. There is no major deviation in the hardness value from the surface to the core. The surface region recorded a hardness of 351 MPa, while the core region showed a slightly higher value of 380 MPa.

3.5. Optical microscopy

The analysis aimed to identify characteristic patterns that can help determine the nature of the cracks, locate the origin point, and narrow down to the root cause of the failure under operational stresses. The sample (Figure 5a) was hot mounted with phenolic resin, ground, and polished, then etched with 2% nital. OM revealed the presence of secondary surface cracks (Figure 5b and c) accompanied by evident signs of decarburization (Figure 5d and e). The decarburized zones appeared as lighter regions near the surface, indicating a loss of carbon from the steel matrix. This phenomenon is typically associated with exposure to elevated temperatures in the presence of oxygen, likely during heat treatment, forging, or other thermal processing stages.

Decarburization can lead to a softer, weaker surface layer, which not only reduces surface hardness but also makes the material more susceptible to crack initiation and propagation under cyclic loading. The observed secondary cracks in these regions may have originated due to the lower mechanical strength and stress concentration effects at the decarburized interfaces.

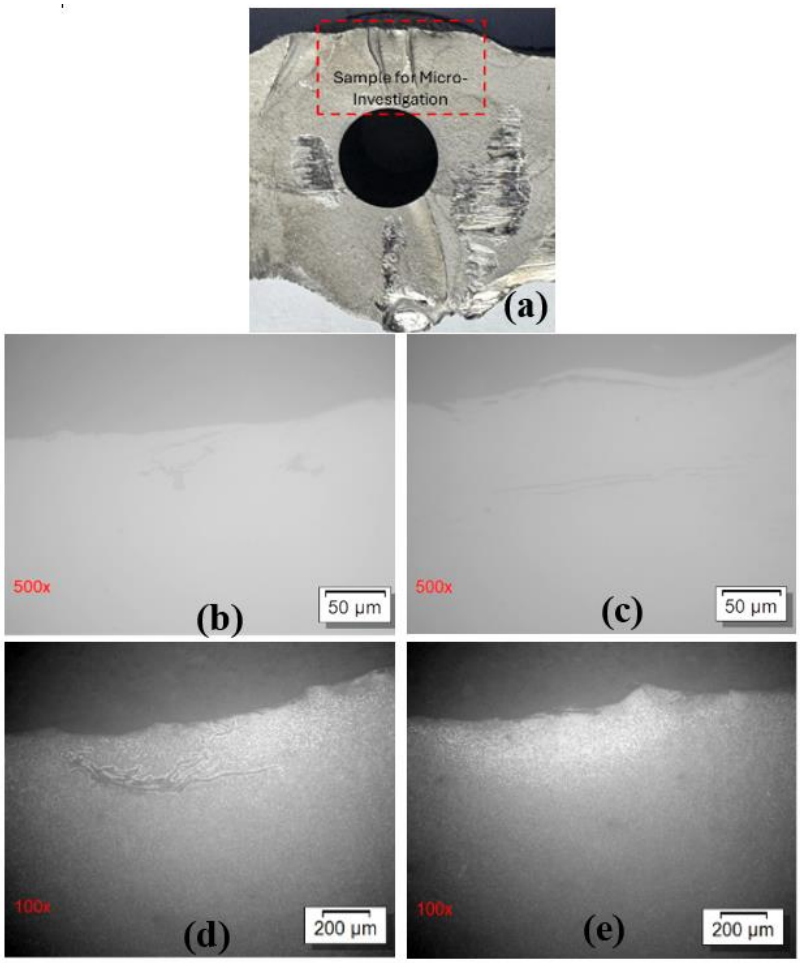

Fig. 5. *Secondary cracks (b and c) and surface decarburization (d and e)*

THE ANNALS OF "DUNAREA DE JOS" UNIVERSITY OF GALATI
FASCICLE IX. METALLURGY AND MATERIALS SCIENCE
Nº. 2 - 2026, ISSN 2668-4748; e-ISSN 2668-4756
Article DOI: https://doi.org/10.35219/mms.2026.2.07

These findings highlight the importance of controlled heat treatment atmospheres and protective surface measures to preserve carbon content and maintain the integrity of critical components like connecting rods.

3.6. Inclusion analysis

The inclusion content was determined according to ASTM E45 for steels using microscopic examination. This standard is primarily used in quality control and material certification to ensure the steel meets required cleanliness standards. ASTM E45 categorizes inclusions into four main types: Type A (Sulphide Inclusions) – Usually manganese sulfides (MnS), elongated due to rolling; Type B (Aluminate Inclusions) – Alumina (Al_2O_3) inclusions, typically globular; Type C (Silicate Inclusions) – Elongated silicates formed from deoxidation; Type D (Globular Oxide Inclusions): Small, discrete globular oxides, typically alumina or complex oxides.

Inclusion analysis was conducted at 200x magnification (Figure 6).

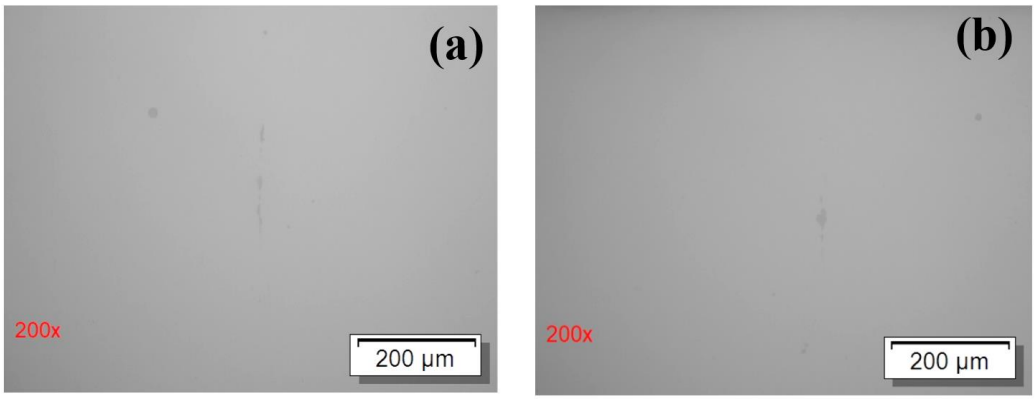

Fig. 6. *Optical micrographs (a and b) showing non-metallic inclusions*

The examination revealed the presence of thick Type-C (silicate) and thick Type-D (globular oxide) inclusions, both rated at a severity level of 1.0. No Type-A (sulphide) or Type-B (alumina) inclusions were observed (Table 2).

Table 2. *Inclusion levels*

Sample ID.	A, Sulphide		B, Alumina		C, Silicate		D, Globular oxide	
	Thin	Thick	Thin	Thick	Thin	Thick	Thin	Thick
Conn. rod	-----	-----	-----	-----	-----	1.0	-----	1.0

The inclusions detected fall within acceptable limits, and no inclusion-related abnormalities were identified in the sample tested. The steel meets the cleanliness requirements typically expected for high-performance applications.

3.7. Scanning electron microscopy (SEM) and EDS

Scanning electron microscopy (SEM) and energy-dispersive X-ray spectroscopy (EDS) were carried out on the cross-sectional fractured surface to observe the surface topography and identify the elements present on the surface.

We used SEM for fractography analysis to reveal microscopic features (dimples, cleavage facets, beach marks, and striations) that indicate fracture modes and root causes of material failure. It detects inclusions, impurities, segregation, porosity, and other processing defects.

EDS was used to measure the weight percentage of all elements present in the defect area. Elemental distribution maps clearly visualize element segregation, diffusion, inclusions, and contaminants.

Quantitative data reports, with precise elemental percentages - including spectra, maps, and line profiles - were performed.

THE ANNALS OF "DUNAREA DE JOS" UNIVERSITY OF GALATI
FASCICLE IX. METALLURGY AND MATERIALS SCIENCE
No. 2 - 2026, ISSN 2668-4748; e-ISSN 2668-4756
Article DOI: https://doi.org/10.35219/mms.2026.2.07

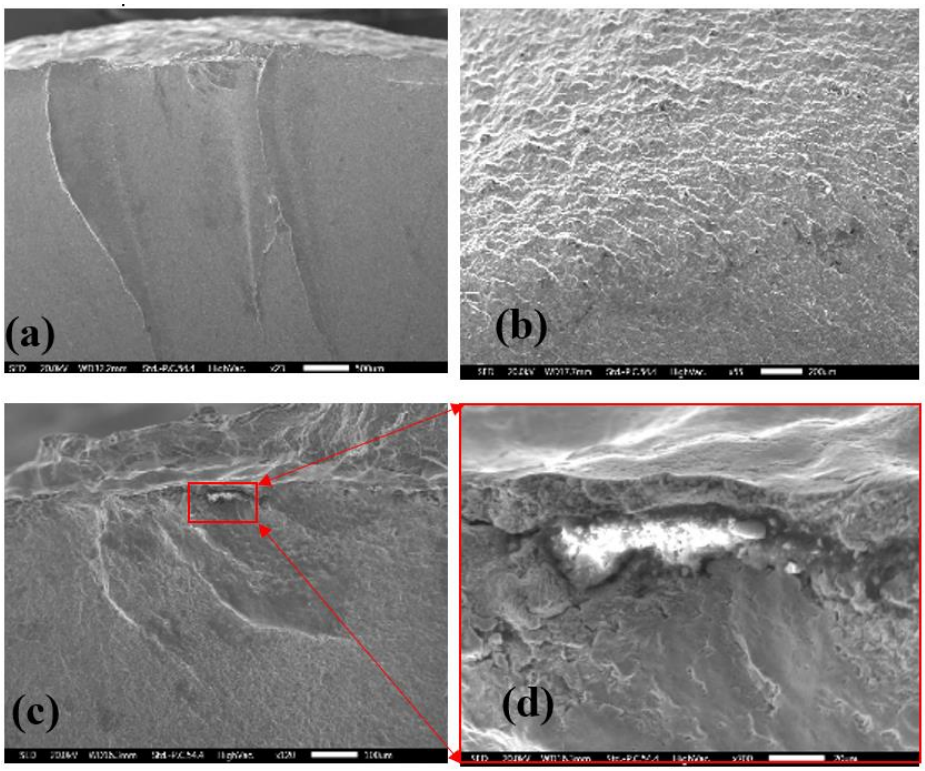

Fig. 7. *SEM micrographs: (a) Ratchet marks from the top central region (thinner wall zone), (b) Beach marks on the fracture surface, and (c and d) exogenous entrapment with adjacent ratchet marks*

The SEM fractography images (Figure 7) revealed fatigue-related features, such as ratchet marks (Figure 7a), indicating multiple crack initiation points, and cyclic crack propagation. Also, beach marks, which are a typical characteristic of fatigue crack propagation, were observed (Figure 7 b). The suspected crack initiation region located near the central region above the central oil hole revealed entrapment, suggesting the presence of a local defect (Figure 7c and d).

SEM-EDS point analysis (Figure 8) in this region confirmed the presence of several non-metallic inclusions characterized by elevated levels of elements like Ca, Mg, Al, Si, Na, and S, which are typical of inclusion-related entrapment during steel making.

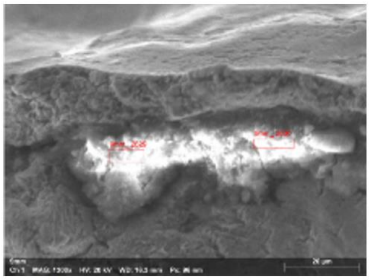

Spectrum	O	Na	Mg	Al	Si	S	K	Ca	Fe
9mm_2629	48.46		9.24	2.28	5.23	0.78	0.81	25.72	7.47
9mm_2630	53.26	0.87	5.85	3.74	10.45	1.12	1.22	13.19	10.30
Mean	**50.86**	**0.87**	**7.55**	**3.01**	**7.84**	**0.95**	**1.01**	**19.45**	**8.88**
Sigma	**3.39**	**0.00**	**2.40**	**1.03**	**3.69**	**0.23**	**0.29**	**8.86**	**2.00**
SigmaMean	**2.40**	**0.00**	**1.70**	**0.73**	**2.61**	**0.17**	**0.20**	**6.26**	**1.42**

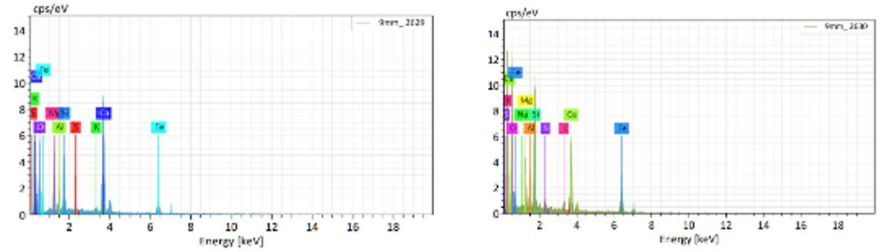

Fig. 8. *EDS spectra*

Overall, the SEM-EDS analysis confirms that the presence of non-metallic inclusions significantly contributed to the initiation and growth of fatigue cracks that led to the failure of the component.

4. Conclusions

The failure investigation of the connecting rod from the oxygen compressor unit (ASP1) concluded that failure occurred due to fatigue crack initiation at a localized region of reduced wall thickness adjacent to the central oil hole. SEM-EDS analysis further confirmed the presence of non-metallic entrapments, including Ca, Mg, Al, Si, and S, whose combined effect with the geometric inconsistency created stress concentrations that led to crack propagation under normal service conditions.

Visual examination revealed asymmetry in the connecting rod's geometry, particularly near the central oil hole. Digital calliper measurements confirmed a significant wall thickness variation (approx. a 1.53 mm difference), indicating potential machining misalignment or forging inconsistency. This geometric deviation introduced localized stress concentration zones making the region more prone to fatigue.

Moreover, one side of the connecting rod exhibited a shiny, machined surface with scratches, indicating post-forging machining or grinding operations. The opposite side retained a raw as-forged appearance, suggesting asymmetrical surface processing possibly affecting stress distribution.

Spectral analysis confirmed that the material closely matches AISI 4140, a chromium-molybdenum alloy steel suitable for high-stress applications. All major alloying and residual elements were within expected ranges, aligning with OEM specifications for forged steel components.

Nevertheless, SEM-EDS analysis at the crack origin revealed localized entrapment of non-metallic inclusions (Ca, Mg, Al, Si, S), likely from steelmaking, acting as micro-stress risers.

Furthermore, the fractographic analysis (SEM) identified fatigue crack initiation originating from the thinner region near the central oil hole. Features such as ratchet marks and beach marks indicated multiple crack initiation points and cyclic crack growth. Decarburization near the surface further reduced local strength, contributing to crack propagation under normal operating stresses.

We conclude that the root cause of the failure has been identified as fatigue crack initiation at a region of reduced wall thickness near the central oil hole driven by geometric asymmetry and the presence of non-metallic entrapments acting as stress concentrators. Although the material chemistry conformed to specifications, localized manufacturing inconsistencies and inclusion-related defects led to fatigue failure during normal service conditions.

References

[1]. Zhao C. L., *et al.*, *Analysis and Simulation Optimization of Connecting Rod Cap Failure in Compressor*, Int. J. Simul. Model., 2026.
[2]. Zhang Z., *et al.*, *Study of Failure Analysis and Manufacturing Processes Improvement of Cracking Connecting Rod*, J. Mech. Sci. Technol., 2022.
[3]. Strozzi A., *et al.*, *A Repertoire of Failures in Connecting Rods*, Engineering Failure Analysis, 2016.
[4]. Madaana A., Gupta B., *Metallurgical Analysis of Fractured Connecting Rod*, IJERT, 2019.
[5]. Gok M. G., Cihan O., *Investigation of Failure Mechanism of a DCI Engine Connecting Rod*, European Journal of Technique, 2021.
[6]. Prajapati H., *et al.*, *Investigation and Solution of Repetitive Failure of Connecting Rod*, International Conference on Multidisciplinary Research, 2026.
[7]. Xu W., *et al.*, *On a Numerical Methodology to Assess the Fatigue Life of Connecting Rods*, Proc. IMechE Part D, 2023.
[8]. Renso F., *et al.*, *Finite Element Analysis of Fretting Phenomena at the Bearing/Big End Interface*, Lubricants, 2023.
[9]. Barker M., *et al.*, *Practical Root Cause Analysis of Connecting Rod Bushing Failures*, Turbomachinery Symposium, 2008.
[10]. Kumar M., *et al.*, *Design and Fatigue Analysis of Connecting Rod with Composite Material Using ANSYS*, NanoWorld Journal, 2023.
[11]. Kumar M., Prajapati S. N., *Design, Buckling and Fatigue Failure Analysis of Connecting Rod: A Review*, International Journal of Advanced Engineering Research and Science, vol. 4, no. 7, p. 39-45, Jul. 2017.
[12]. Shu J., Fu X., *Topology Optimization Design of Compressor Connecting Rod*, J. Phys.: Conf. Ser., 2022.
[13]. Ketmuang Y., *et al.*, *Effect on Fatigue Behavior of Connecting Rod*, ETASR, 2024.
[14]. Gurau L., *Failure Case Study Series Part One: Analysis of Oxygen Compressor Shaft Breakage*, The Annals of "Dunarea de Jos" University of Galati. Fascicle IX, Metallurgy and Materials Science, vol. 49, no. 1, p. 11-18, 2026.

THE ANNALS OF "DUNAREA DE JOS" UNIVERSITY OF GALATI
FASCICLE IX. METALLURGY AND MATERIALS SCIENCE
No. 2 - 2026, ISSN 2668-4748; e-ISSN 2668-4756
Article DOI: https://doi.org/10.35219/mms.2026.2.08

FUNCTIONALIZED PLASMONIC NANOPARTICLES: SYNTHESIS, SURFACE ENGINEERING AND EMERGING BIOMEDICAL APPLICATIONS

Mariana BUȘILĂ
Research Centre in Manufacturing Engineering Technology (ITCM), Faculty of Engineering, "Dunarea de Jos" University of Galati, 47 Domneasca Street, 800008 Galati, Romania
e-mail: mariana.busila@ugal.ro

ABSTRACT

Functionalized plasmonic nanoparticles have attracted significant attention in biomedical research due to their unique optical properties, high surface reactivity, and versatile surface chemistry. In this study, gold nanoparticles (AuNPs) were synthesized via the Turkevich citrate reduction method and subsequently functionalized using (3-glycidyloxypropyl) trimethoxysilane (GPTMS) to enhance their stability and surface reactivity. The synthesized and functionalized nanoparticles were comprehensively characterized using multiple analytical techniques. Morphological features and particle size distribution were investigated by transmission electron microscopy (TEM) and scanning electron microscopy (SEM), while elemental composition was confirmed by energy-dispersive X-ray spectroscopy (EDS). The crystalline structure was analysed using X-ray diffraction (XRD), and the average crystallite size was estimated using the Scherrer equation. Fourier-transform infrared spectroscopy (FTIR) was employed to identify surface functional groups and confirm successful GPTMS functionalization. Additionally, UV–Vis spectrophotometry was used to evaluate the optical properties of the nanoparticles and to assess their localized surface plasmon resonance (LSPR) behavior. The results demonstrate that the functionalized AuNPs exhibit stable colloidal properties, controlled morphology, and modified optical responses due to surface engineering. The presence of additional absorption features in the UV region highlights the influence of GPTMS on the interfacial environment of the nanoparticles. The obtained results underscore the potential of GPTMS-functionalized gold nanoparticles for applications in nanomedicine, including biosensing, drug delivery, and optical bioimaging.

KEYWORDS: plasmonic nanoparticles; gold nanoparticles; surface functionalization; GPTMS; biomedical applications

1. Introduction

Nanotechnology has significantly transformed biomedical research by enabling the development of materials with size-dependent properties that interact efficiently with biological systems at the molecular and cellular levels. Among these materials, plasmonic nanoparticles - particularly gold- and silver-based systems - have attracted considerable attention due to their unique optical properties, chemical stability, and high biocompatibility [1-3].

The defining feature of these nanostructures is localized surface plasmon resonance (LSPR), which arises from the collective oscillation of conduction electrons under electromagnetic excitation. This phenomenon leads to strong light absorption and scattering which can be precisely tuned by controlling nanoparticle size, shape, and composition [2-4]. Notably, the ability to shift the LSPR into the near-infrared (NIR) region makes these systems particularly attractive for biomedical applications as NIR light exhibits deeper tissue penetration and reduced biological absorption [3, 5].

Recent advances have demonstrated that plasmonic nanoparticles can be engineered for a wide range of biomedical applications, including imaging, biosensing, and minimally invasive therapies such as photothermal treatment [4-6]. However, their

THE ANNALS OF "DUNAREA DE JOS" UNIVERSITY OF GALATI
FASCICLE IX. METALLURGY AND MATERIALS SCIENCE
Nº. 2 - 2026, ISSN 2668-4748; e-ISSN 2668-4756
Article DOI: https://doi.org/10.35219/mms.2026.2.08

performance is determined not solely by the core structure but also by the surface properties which govern interactions with biological environments.

Surface functionalization plays a critical role in enhancing colloidal stability, reducing toxicity, and enabling targeted delivery. Strategies such as ligand conjugation, polymer coating, and silane-based modification have been extensively explored to tailor nanoparticle behavior in complex biological systems [6-8].

In this context, the present work provides a comprehensive overview of the synthesis and solution-chemical surface functionalization of gold nanoparticles, highlighting the role of the silane-based compound (3-glycidyloxypropyl) trimethoxysilane (GPTMS), as well as the biomedical applications of plasmonic nanoparticles with a particular focus on gold-based systems. Special attention is paid to the interplay between structural design, surface functionalization, and plasmonic behavior as well as their implications for next-generation biomedical applications.

2. Experimental procedure

2.1. Synthesis of gold nanoparticles by the Citrate Method (Turkevich method)

Gold nanoparticles (AuNPs) were synthesized via the classical citrate reduction method (Turkevich method [9]), which enables the formation of relatively monodisperse spherical nanoparticles in aqueous media.

Initially, an aqueous solution of chloroauric acid ($HAuCl_4$) with a concentration of 1.0 mM was prepared by dissolving the appropriate amount of precursor in deionized water. Separately, a 1% (w/v) sodium citrate solution was prepared by dissolving sodium citrate in deionized water under continuous stirring.

For the synthesis, the $HAuCl_4$ solution was transferred into a round-bottom flask and heated to approximately 80 °C under constant magnetic stirring to ensure a homogeneous temperature distribution. Once the desired temperature was reached, the sodium citrate solution was rapidly added to the reaction mixture under continuous stirring.

The addition of sodium citrate initiates the reduction of Au^{3+} ions to metallic gold (Au^0), while simultaneously acting as a stabilizing agent. Upon the addition of the reducing agent, the solution undergoes a sequence of colour changes, ultimately turning ruby red, which is characteristic of gold nanoparticle formation and is attributed to localized surface plasmon resonance (LSPR).

The reaction was maintained under heating and stirring until a stable ruby-red colloidal suspension was obtained, indicating the successful synthesis of gold nanoparticles (Figure 1, a-e).

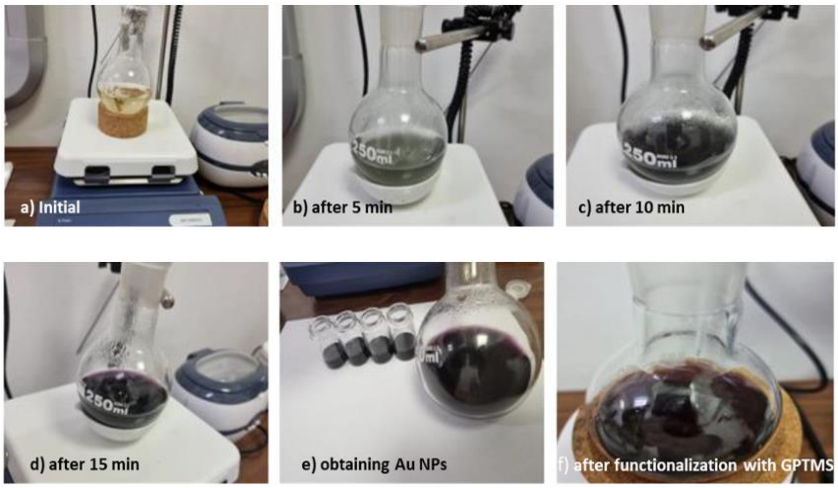

Fig. 1. *Steps of the synthesis of gold nanoparticles functionalized with GPTMS*

Following the formation of gold nanoparticles, the reaction mixture was allowed to cool naturally to room temperature under continuous magnetic stirring. This step ensures the stabilization of the colloidal system and prevents uncontrolled aggregation during temperature equilibration.

Subsequently, the obtained gold nanoparticles were purified to remove excess reagents and by-products. The colloidal suspension was subjected to multiple washing cycles using deionized water followed by centrifugation. After each centrifugation step, the supernatant was discarded and the nanoparticles were redispersed in fresh deionized

THE ANNALS OF "DUNAREA DE JOS" UNIVERSITY OF GALATI
FASCICLE IX. METALLURGY AND MATERIALS SCIENCE
N°. 2 - 2026, ISSN 2668-4748; e-ISSN 2668-4756
Article DOI: https://doi.org/10.35219/mms.2026.2.08

water. This purification process was repeated several times to ensure the removal of unreacted citrate ions and residual impurities, resulting in a stable and purified nanoparticle suspension.

2.2. Surface Functionalization with GPTMS

Surface functionalization of the synthesized gold nanoparticles was carried out using (3-glycidyloxypropyl) trimethoxysilane (GPTMS) to introduce reactive functional groups and enhance their applicability in biomedical systems (Figure 2).

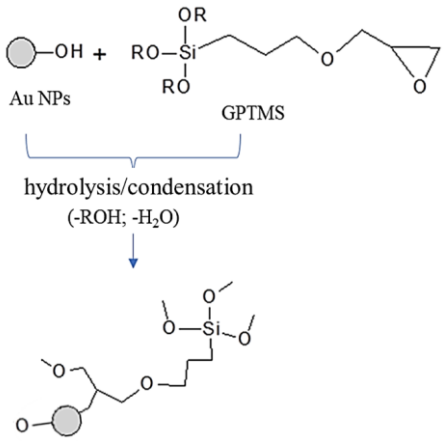

Fig. 2. *Proposed scheme for the functionalization of Au nanoparticles with (3-glycidyloxypropyl) trimethoxysilane (GPTMS)* [10]

A 1% GPTMS solution was added to the purified gold nanoparticle suspension under continuous magnetic stirring at room temperature. The reaction was allowed to proceed for 4 hours to ensure uniform surface coverage of the nanoparticles. During this time, the silane groups of GPTMS undergo hydrolysis and condensation forming a siloxane network on the nanoparticle surface, while the epoxide groups remain available for further functionalization (Figure 2f).

After the functionalization step, the nanoparticles were thoroughly washed multiple times with ethanol followed by deionized water to remove unbound GPTMS and residual impurities. The purified, functionalized nanoparticles were then redispersed in deionized water for further analysis.

2.3. Characterization Techniques

The morphological characteristics of the synthesized nanoparticles were investigated using both transmission electron microscopy (TEM) and scanning electron microscopy (SEM). TEM analysis was performed using a JEOL JEM-1010 instrument to evaluate particle size and morphology at the nanoscale. Samples for TEM were prepared by depositing a few drops of the nanoparticle suspension onto carbon-coated copper grids, followed by drying at room temperature under ambient conditions.

Complementary morphological analysis was carried out using a scanning electron microscope (SEM, Quanta Inspect F, FEI Company). The chemical composition of the samples was determined by energy-dispersive X-ray spectroscopy (EDX), coupled with the SEM system, allowing for elemental analysis and confirmation of the presence of gold in the synthesized nanoparticles.

The crystalline structure of the gold nanoparticles was analysed by X-ray diffraction (XRD) using a Rigaku SmartLab diffractometer (9 kW) with Cu Kα radiation (λ = 0.154 nm) in a parallel beam configuration. Powder X-ray diffraction (PXRD) measurements were conducted in θ–2θ scanning mode.

The average crystallite size was estimated using the Scherrer equation (1):

$$D = \frac{K\lambda}{\beta\cos\theta} \quad (1)$$

where D represents the crystallite size, K is the shape factor (typically ~0.9), λ is the X-ray wavelength, β is the full width at half maximum (FWHM) of the diffraction peak expressed in radians, and θ is the Bragg diffraction angle.

Fourier-transform infrared (FTIR) spectroscopy was performed using a Bruker Optics Tensor 27 spectrometer to investigate the chemical bonding configuration of the samples. The measurements were carried out at room temperature over the spectral range of 4000–400 cm^{-1}, with 64 scans collected for each sample. The KBr pellet method was employed for sample preparation. The obtained spectra were analysed by assigning the observed absorption bands to the corresponding vibrational modes of the molecular functional groups.

The optical absorption properties of the samples were evaluated using a UV–Vis spectrophotometer (Cary 5000, Agilent Technologies, Santa Clara, CA, USA) at room temperature. The absorption spectra of the gold nanoparticle suspensions were recorded to confirm nanoparticle formation and to assess their optical characteristics.

For gold nanoparticles synthesized via the citrate reduction method in aqueous solution with typical sizes in the range of 20–30 nm, a characteristic localized surface plasmon resonance (LSPR) peak is generally observed around 520 nm.

THE ANNALS OF "DUNAREA DE JOS" UNIVERSITY OF GALATI
FASCICLE IX. METALLURGY AND MATERIALS SCIENCE
Nº. 2 - 2026, ISSN 2668-4748; e-ISSN 2668-4756
Article DOI: https://doi.org/10.35219/mms.2026.2.08

Following surface functionalization, additional absorption features were detected in the ultraviolet region (250–350 nm), which can be attributed to modifications in the surface chemistry and the presence of functional groups introduced during the functionalization process.

3. Results and discussion

3.1. Morphological and Elemental Analysis (SEM–EDS and TEM)

Energy-dispersive X-ray spectroscopy (EDS) is an analytical technique widely used to determine the elemental composition of materials. It is commonly coupled with scanning electron microscopy (SEM) or transmission electron microscopy (TEM), enabling both qualitative and semi-quantitative analysis as well as spatial mapping of elemental distribution across the sample surface or within its volume. This technique allows the identification of regions with varying elemental concentrations and facilitates correlation with morphological features observed in electron microscopy images.

The particle size and morphology were further evaluated using transmission electron microscopy (TEM) (Figure 3.). The images reveal the formation of gold nanoparticles with sizes ranging between 20 and 30 nm. The nanoparticles exhibit a polydisperse distribution and display a variety of shapes, including spherical, tetragonal, and pentagonal morphologies.

The observed polydispersity reflects variations in both size and shape within the nanoparticle population and is influenced by several synthesis parameters, including precursor concentration, reducing agent, stabilizing agents, pH, and reaction conditions. Higher precursor concentrations may accelerate nucleation and growth processes, leading to a broader size distribution. Additionally, the presence of surface-modifying agents such as GPTMS can influence nanoparticle growth dynamics by selectively interacting with specific crystal facets, thereby affecting both morphology and stability.

As shown in Figure 3, the semi-quantitative EDS analysis confirms the presence of gold as the dominant element in the synthesized samples. The elemental distribution appears relatively homogeneous, indicating a uniform composition of the nanoparticles.

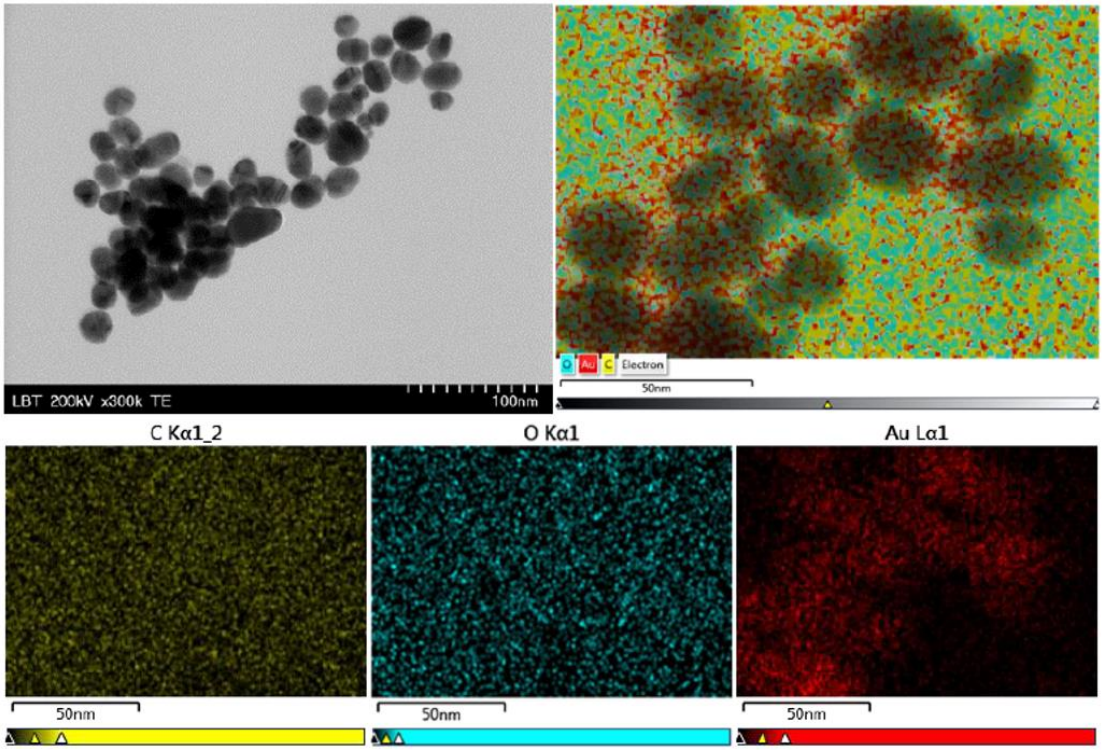

Fig. 3. *TEM image of gold nanoparticles and EDS analysis of the distribution of chemical elements*

Figure 4 presents point-based EDS analysis where the acquired spectrum was processed using dedicated software to identify characteristic peaks corresponding to the elements present. The presence of gold is further confirmed by the detection of its characteristic peaks at approximately 2.12 keV and 9.71 keV, which are consistent with the known X-ray emission lines of gold.

THE ANNALS OF "DUNAREA DE JOS" UNIVERSITY OF GALATI
FASCICLE IX. METALLURGY AND MATERIALS SCIENCE
Nº. 2 - 2026, ISSN 2668-4748; e-ISSN 2668-4756
Article DOI: https://doi.org/10.35219/mms.2026.2.08

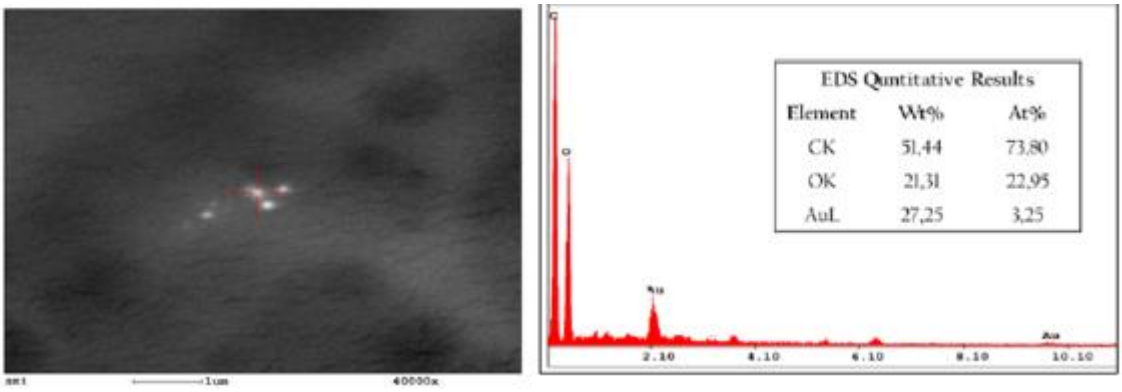

Fig. 4. *EDAX analysis for gold nanoparticles*

It should be noted that the signals corresponding to carbon and oxygen detected in the EDS analysis originate primarily from the supporting substrate used during the measurements rather than from the intrinsic composition of the gold nanoparticles.

Overall, the combined SEM–EDS and TEM analyses confirm the successful synthesis of gold nanoparticles, providing insight into their morphology, size distribution and elemental composition.

3.2. Structural characterization of functionalized gold nanoparticles

To evaluate the structural characteristics of the samples studied, X-ray diffraction investigations were performed (Figure 5). The typical diffractogram of gold nanoparticles shows four peaks corresponding to the standard Bragg reflections characteristic of the (111), (200), (220) and (311) planes of the face-centered cubic crystal structure. The peak with the highest intensity at the angle 2θ = 38.1 represents a preferential growth in the (111) direction.

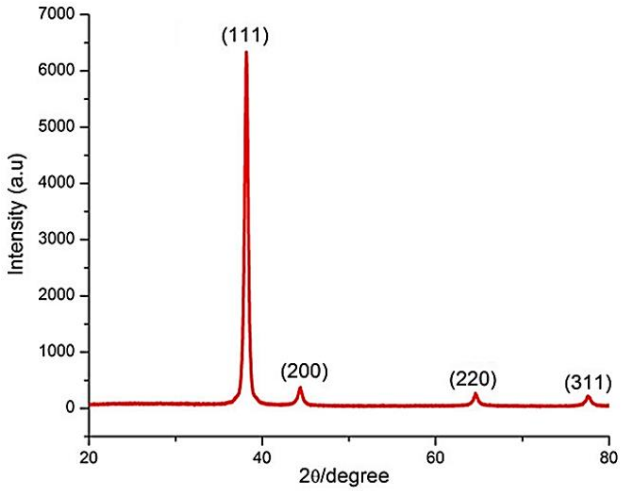

Fig. 5. *XRD analysis of gold nanoparticles*

Other diffraction peaks corresponding to impurities or sodium citrate were not found, suggesting the high purity of the synthesized nanomaterials.

Figure 6 presents the FTIR spectrum of the synthesized gold nanoparticles. The presence of distinct absorption bands at approximately 3400 cm^{-1} and 2916 cm^{-1} can be attributed to N–H stretching vibrations of primary and secondary amines and C–H stretching vibrations, respectively. These features may also indicate the presence of hydroxyl (-OH) functional groups on the nanoparticle surface.

Additionally, absorption bands observed in the range of 1600–1400 cm^{-1} are associated with O–H bending and stretching vibrations, which can be attributed to surface hydroxyl groups and adsorbed moisture. These findings suggest the presence of surface-bound species and functional groups that may play a role in nanoparticle stabilization and subsequent surface functionalization processes.

THE ANNALS OF "DUNAREA DE JOS" UNIVERSITY OF GALATI
FASCICLE IX. METALLURGY AND MATERIALS SCIENCE
N°. 2 - 2026, ISSN 2668-4748; e-ISSN 2668-4756
Article DOI: https://doi.org/10.35219/mms.2026.2.08

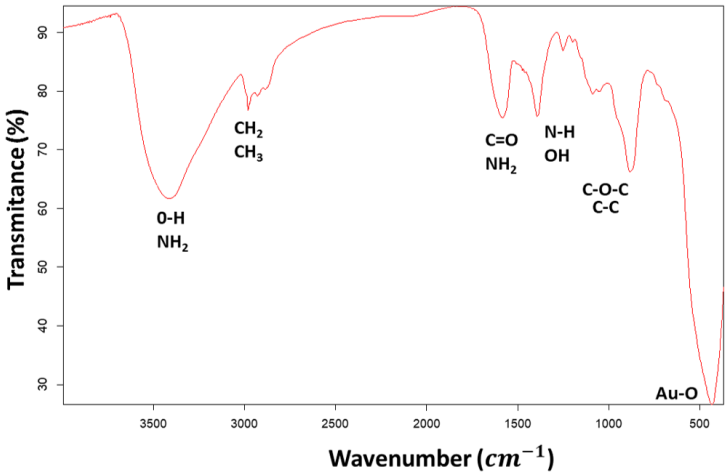

Fig. 6. *FTIR spectrum - Fourier transform infrared spectroscopy of functionalized gold nanoparticles*

A distinct absorption band observed around 1100 cm^{-1} corresponds to Si–O stretching vibrations, indicating the presence of siloxane bonds and suggesting that the silane fragment is successfully anchored onto the surface of the gold nanoparticles [11]. This feature provides strong evidence for the formation of a silane layer following GPTMS functionalization.

Furthermore, the absorption peak located at approximately 820 cm^{-1} can be attributed to Si–O–CH_3 vibrations, characteristic of GPTMS-derived structures [12]. The presence of this band further confirms the successful incorporation of the silane coupling agent onto the nanoparticle surface.

Overall, the FTIR results demonstrate the formation of a hybrid organic–inorganic interface, confirming that GPTMS functionalization was successfully achieved and that reactive functional groups are present on the nanoparticle surface for potential subsequent modifications.

3.3. Analysis of additional SPR bands in GPTMS-functionalized AuNPs

Gold nanoparticles (AuNPs) are well known for their plasmonic properties, which are manifested through localized surface plasmon resonance (LSPR) bands in the UV–Vis spectrum. These optical features arise from the collective oscillation of conduction band electrons induced by an external electromagnetic field, leading to strong and selective light absorption and scattering.

For spherical gold nanoparticles with sizes in the range of 20–30 nm, a characteristic LSPR band is typically observed around 520 nm. However, following surface functionalization with (3-glycidyloxypropyl) trimethoxysilane (GPTMS), additional absorption features were observed in the ultraviolet region, specifically at approximately 230, 270, and 312 nm (Figure 7).

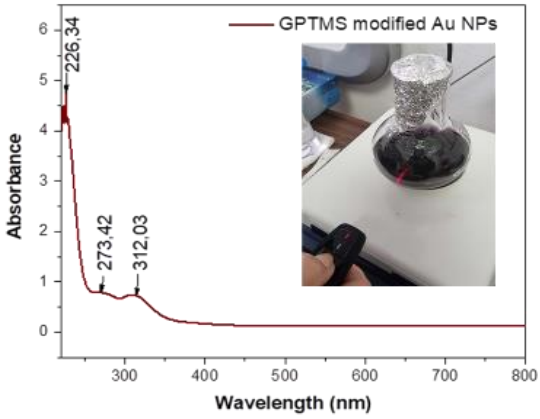

Fig. 7. *UV-Vis absorption spectrum of functionalized gold nanoparticles*

These supplementary bands are not directly associated with the classical plasmonic resonance of gold nanoparticles but rather can be attributed to electronic transitions related to the organic moieties introduced by GPTMS, as well as to interfacial effects arising from nanoparticle–ligand interactions [13]. The attachment of GPTMS onto the nanoparticle surface modifies the local dielectric environment, which can influence the optical response of the system.

Moreover, surface functionalization may promote partial aggregation or clustering of nanoparticles, leading to plasmonic coupling effects. Such interactions between closely spaced nanoparticles can give rise to additional optical features due to dipole–dipole interactions and the emergence of new plasmonic modes. However, these effects should be interpreted with caution as the

presence of UV bands alone does not conclusively indicate plasmonic coupling.

The presence of multiple absorption features may also suggest a certain degree of structural and morphological heterogeneity, consistent with the polydisperse nature of the synthesized nanoparticles [14]. Variations in size, shape, and surface chemistry can contribute to the broadening or modification of the optical response.

Importantly, no significant changes in colour or absorption intensity were observed over a period of 45 days, indicating good colloidal stability of the functionalized nanoparticles at room temperature (Figure 7). This stability can be attributed to the presence of surface-bound GPTMS, which provides steric and chemical stabilization.

Overall, the UV–Vis analysis confirms that surface functionalization with GPTMS influences the optical properties of gold nanoparticles, primarily through modification of the interfacial environment and potential nanoparticle interactions, while preserving the overall colloidal stability of the system.

4. Conclusions

Gold nanoparticles (AuNPs) were successfully synthesized using the Turkevich citrate reduction method resulting in particles with sizes below 30 nm and exhibiting a polydisperse distribution. The structural analysis performed by X-ray diffraction confirmed the formation of a face-centered cubic (fcc) crystalline structure, with characteristic Bragg reflections corresponding to the (111), (200), (220), and (311) planes. The most intense diffraction peak observed at $2\theta \approx 38.1°$ indicates a preferential growth orientation along the (111) crystallographic plane.

The formation of gold nanoparticles was initially indicated by the characteristic ruby-red colour of the colloidal solution which arises from the excitation of localized surface plasmon resonance (LSPR). This observation was further confirmed by UV–Vis spectroscopic measurements which revealed the presence of the typical plasmonic absorption band associated with gold nanoparticles in the visible region. Additional absorption features observed in the ultraviolet region (250–350 nm) are attributed to surface functionalization effects and interfacial interactions, rather than intrinsic plasmonic modes.

Surface functionalization with GPTMS was successfully achieved as confirmed by FTIR analysis, indicating the formation of a hybrid organic–inorganic interface on the nanoparticle surface. This modification enhances the chemical versatility and stability of the nanoparticles, enabling further functionalization and integration into complex systems.

Considering their tuneable optical properties, surface adaptability, and demonstrated stability, the synthesized AuNPs represent promising platforms for a wide range of biomedical applications. These include targeted drug and gene delivery, biosensing, detection, and optical bioimaging. The results highlight the importance of controlled synthesis and surface engineering in tailoring nanoparticle properties for advanced applications in nanomedicine.

Acknowledgements

This work was supported by the Scientific Research contract no. RF 828 dated 11.12.2024, in partnership with SC ARTZ Dent SRL, Galati, Romania, within the project entitled "Development of Functional Surfaces for Dental Implants: Hydroxyapatite Enriched with Bioactive Agents for Osseointegration and Antimicrobial Protection", Acronym BIOHAF (Biocompatible Implants Optimized with Hydroxyapatite and Functional Additives).

References

[1]. Dreaden E. C., *et al.*, *The golden age: Gold nanoparticles for biomedicine*, Chem. Soc. Rev., vol. 41, p. 2740-2779, 2021.
[2]. Jain P. K., *et al.*, *Plasmonics in nanomedicine*, Chem. Rev., vol. 120, p. 103-139, 2020.
[3]. Langer J., *et al.*, *Present and future of surface-enhanced Raman scattering*, ACS Nano, vol. 14, p. 28-117, 2020.
[4]. Anker J. N., *et al.*, *Biosensing with plasmonic nanosensors*, Nat. Mater., vol. 7, p. 442-453, 2021.
[5]. Huang X., *et al.*, *Gold nanoparticles in photothermal therapy: Mechanisms and applications*, L. Med. Sci., 37, p. 2345-56, 2022.
[6]. Li N., *et al.*, *Plasmonic nanoparticles for biomedical applications*, Nano Today, vol. 58, p. 102345, 2024.
[7]. Albanese A., *et al.*, *The effect of nanoparticle surface chemistry on biological systems*, Annu. Rev. Biomed. Eng., vol. 14, p. 1-16, 2021.
[8]. Sperling R. A., *et al.*, *Biological applications of gold nanoparticles*, Chem. Soc. Rev., vol. 37, p. 1896-1908, 2022.
[9]. Dong J., *et al.*, *Synthesis of Precision Gold Nanoparticles Using Turkevich Method*, Kona., 37, p. 224-232, DOI: 10.14356/kona.2020011, 2020.
[10]. Buşilă M., *et al.*, *Synthesis and characterization of antimicrobial textile finishing based on Ag:ZnO nanoparticles /chitosan biocomposites*, RSC Adv., 5, p. 21562-71, 2015.
[11]. Ma J., *et al.*, *Fabrication of modified hydrogenated castor oil/GPTMS:ZnO composites and effect on UV resistance of leather*, Sci. Rep., 7, 3742, 2017.
[12]. Schramm C., *High temperature ATR-FTIR characterization of the interaction of polycarboxylic acids and organotrialkoxysilanes with cellulosic material*, Spectroch. Acta A Mol. Biomol. Spectrosc., 243, 118815, 2020.
[13]. Bhainsa K. C., D'Souza S. F., *Extracellular biosynthesis of silver nanoparticles using the fungus Aspergillus fumigatus*, Colloids Surf. B Biointerf., 47, p. 160-164, 2006.
[14]. Narayanan K. B., Sakthivel N., *Facile green synthesis of gold nanostructures by NADPH-dependent enzyme from the extract of Sclerotium rolfsii*, Colloids Surf. B Physicochem. Eng. Aspects, 380, p. 156-161, 2011.

MANUSCRISELE, CĂRŢILE ŞI REVISTELE PENTRU SCHIMB, PRECUM ŞI ORICE CORESPONDENŢE SE VOR TRIMITE PE ADRESA:

MANUSCRIPTS, REVIEWS AND BOOKS FOR EXCHANGE COOPERATION, AS WELL AS ANY CORRESPONDANCE WILL BE MAILED TO:

LES MANUSCRIPTS, LES REVUES ET LES LIVRES POUR L'ECHANGE, TOUT AUSSI QUE LA CORRESPONDANCE SERONT ENVOYES A L'ADRESSE:

MANUSCKRIPTEN, ZIETSCHRITFTEN UND BUCHER FUR AUSTAUCH SOWIE DIE KORRESPONDENZ SID AN FOLGENDE ANSCHRIFT ZU SEDEN:

After the latest evaluation of the journals by the National Center for Science Policy and Scientometrics (**CENAPOSS**), in recognition of its quality and impact at national level, the journal will be included in the B^+ category, 215 code (http://cncsis.gov.ro/userfiles/file/CENAPOSS/Bplus_2011.pdf).

The journal is already indexed in:
DOAJ: https://doaj.org/
SCIPIO-RO: http://www.scipio.ro/web/182206
EBSCO: http://www.ebscohost.com/titleLists/a9h-journals.pdf
Google Academic: https://scholar.google.ro
Index Copernicus: https://journals.indexcopernicus.com
Crossref: https://search.crossref.org/

The papers published in this journal can be viewed on the website: http://www.gup.ugal.ro/ugaljournals/index.php/mms

Name and Address of Publisher:
Contact person: Prof. Dr. Eng. Elena MEREUŢĂ
Galati University Press - GUP
47 Domneasca St., 800008 - Galati, Romania
Phone: +40 336 130139
Fax: +40 236 461353
Email: gup@ugal.ro

Name and Address of Editor:
Ş. L. Dr. Eng. Marius BODOR
"Dunarea de Jos" University of Galati, Faculty of Engineering
111 Domneasca St., 800201 - Galati, Romania
Phone: +40 336 130208
Phone/Fax: +40 336 130283
Email: marius.bodor@ugal.ro

AFFILIATED WITH:

- THE ROMANIAN SOCIETY FOR METALLURGY
- THE ROMANIAN SOCIETY FOR CHEMISTRY
- THE ROMANIAN SOCIETY FOR BIOMATERIALS
- THE ROMANIAN TECHNICAL FOUNDRY SOCIETY
- THE MATERIALS INFORMATION SOCIETY (ASM INTERNATIONAL)

Edited under the care of the FACULTY OF ENGINEERING

Annual subscription (4 issues per year)

Fascicle DOI: https://doi.org/10.35219/mms

Volume DOI: https://doi.org/10.35219/mms.2026.2

Editing date: 15.06.2026
Number of issues: 200
Printed by Galati University Press (accredited by CNCSIS)
47 Domneasca Street, 800008, Galati, Romania